CRANFIELD UNIVERSITY

JOAO CORREIA

THE INFLUENCE OF EXTERNAL DISTURBANCES ON THE AERODYNAMIC PERFORMANCE OF A WING IN GROUND EFFECT

CRANFIELD DEFENCE AND SECURITY
Centre for Defence Engineering
Aeromechanical Systems Group

PhD Thesis

Supervisors:
Prof. Kevin Knowles
Dr. Mark Finnis

November 2015

CRANFIELD UNIVERSITY

CRANFIELD DEFENCE AND SECURITY
Centre for Defence Engineering
Aeromechanical Systems Group

PhD Thesis

Academic Year 2015-2016

Joao Correia

THE INFLUENCE OF EXTERNAL DISTURBANCES ON THE AERODYNAMIC PERFORMANCE OF A WING IN GROUND EFFECT

Supervisors: Prof. Kevin Knowles and Dr. Mark Finnis

November 2015

Abstract

Aerodynamic development of race cars is mostly performed in wind tunnels, where consistent and repeatable conditions can be found. This leads to race cars being designed to be very efficient in a uniform, low-turbulence flow. However, while running on the track the airflow passing over a car is frequently altered by the presence of other cars, ambient wind, or track conditions, which may lead to a change in aerodynamic performance.

An experimental and computational study was set up in an attempt to understand the effects of real on-track performance-limiting factors such as roll, yaw and immersion in the wake of a leading car. The study was broken down into independent phases that allowed the collection of reference data, from a wing operating with and without roll and yaw in an undisturbed flow, wake data from a leading wake-generator representative of a monoposto car, and data from the wing operating in the wake of the leading vehicle.

Results from the wake survey led to the identification of three main flow characteristics: low dynamic pressure in the wake, counter-rotating vortices that lead to local velocity components and high turbulence intensities in the wake. The negative influence of these flow characteristics was confirmed once the wing was immersed in the wake, as the wing suffered from a significant reduction in downforce throughout the tested ride height range.

The results from the roll and yaw experiments showed that when operating in either condition an inverted wing in ground effect will experience the same downforce enhancement mechanisms as those present on a wing operating in an unrolled and unyawed condition. Although either roll or yaw showed reductions in the downforce generated by the wing, the roll results showed a small ride height range where it is possible to increase the generated downforce under certain flap and roll settings.

Keywords:

Inverted, Wing, Ground Effect, Wake, Vortices, Roll, Yaw.

To my Wife and Parents

Acknowledgements

A big thank you to my supervisors, Professor Kevin Knowles and Dr. Mark Finnis, for the opportunity given, guidance and most of all for their patience in these last couple of years when my non-academic career led to the write-up taking far too long.

I would like to thank Dave, Brian, Karl and all the technical staff that helped with building or simply setting up the models and experiments.

Thanks also to all the former members of staff and other PhD students, Nathan, Graham, Tanmay, Pira, Varun and Steven for the daily gatherings that kept me sane throughout the time at the Defence Academy.

And finally a big thank you to Dr. Robin Knowles for helping me keep my eyes on the ultimate goal, to Luke Roberts for pushing me to keep writing and to my wife, Raquel, who was there front start to finish.

TABLE OF CONTENTS

List of Figures

List of Tables

Notation

A	Planform area / m^2
AR	Aspect Ratio
c	Wing chord / m
C_D	Drag Coefficient $C_D = \frac{D}{q \times A}$
C_L	Lift Coefficient $C_L = \frac{L}{q \times A}$
C_p	Pressure Coefficient $C_P = 1 - \left(\frac{V}{U}\right)^2$
D	Drag / N
h	Height above the reference plane / m
I	Turbulence intensity $I = \frac{u'}{U}$
L	Lift / N
q	Dynamic pressure / Nm^{-2}
Re_c	Reynolds number based on wing chord
u, v, w	Velocity components aligned with x, y and z axis respectively / ms^{-1}
U	Freestream velocity / ms^{-1}
u’	Root-mean-square of turbulence velocity fluctuations / ms^{-1}
V	Local air velocity / ms^{-1}
x, y, z	Cartesian coordinates. x for streamwise direction, y for lateral direction and z for vertical direction.
x_{LS}	Laminar separation bubble length / m
x_R	Flow reattachment position / m
x_S	Flow separation position / m
α	Flow incidence angle / °

ρ	Air density / kgm^{-3}
τ	Wall shear stress / Pa
CFD	Computational Fluid Dynamics
F1	Formula 1
LDA	Laser Doppler Anemometer / Anemometry
PIV	Particle Image Velocimetry

1 Introduction

1.1 Background

The importance of aerodynamics on a race car's performance has been recognized and understood for some time. The initial focus of aerodynamic development was to reduce drag in order to improve speed and fuel economy. However, the benefits of aerodynamic downforce on the overall performance of a car only started being exploited in Formula 1 in the late 1960s (Wright (1982)). With the increase of downforce, and consequent increase in friction between tyres and road, it was possible to improve the turning rates and acceleration without adding extra weight to the vehicle (Dominy & Dominy (1984)).

Aerodynamic development of a race car is mostly performed in a wind tunnel where consistent and repeatable conditions can be found. This leads to a race car being designed to be very efficient in a uniform, low-turbulence flow. However, while running on the track the airflow passing over a car is frequently altered by the presence of other cars or wind which may lead to a change in performance.

When following another car, the trailing car's performance will be affected by the presence of the leading car. A decrease in drag may be viewed as a positive benefit as it gives an increase in speed for a given power. However, if accompanied by a reduction in downforce, the following car's performance will be affected negatively during braking and cornering.

A Formula 1 car has three main downforce generating devices: the front wing, the rear wing and the underbody. Toet (2013) reported that the front wing, the rear wing and underbody are responsible for approximately 28.5%, 23.8% and 47.6% of the car's total downforce respectively, with other components creating lift. The front wing of the car operates in ground effect at a ride height of 70 to 100mm (Agathangelo & Gascoyne (1998)) above the ground. Ground effect refers to the changes in the aerodynamic forces a wing or body experiences as it approaches the ground. In the case of an inverted wing in ground effect, an

increase in downforce and increase in drag is experienced (Knowles et al. (1994)).

As the front wing is the furthest upstream element of the car all downstream components work in its wake. Katz (2006) reported that changes to the front wing geometry or incidence changed the flow to the rear wing, leading to a reduction of its downforce. Hence the design of the front wing is a compromise between generating downforce and upsetting the downstream flow (Page (2000)). This has led to the front wing being designed mostly as a trimming device to adjust the centre of pressure of the car (Jeffrey et al. (2001)) and also used as a flow management device that helps control the shape and position of the front wheel wake, and also of the downstream flow to the rest of the car (Pegrum (2007)).

1.2 Literature Review

1.2.1 Vehicle Aerodynamic Interaction

The first published work on the interaction of two race cars in tandem was carried out by Romberg et al. (1971). In this work, two 3/8th scale saloon car models were placed above a stationary ground plane and tested in various drafting and overtaking positions. Due to wind-tunnel size restrictions, vehicle separation was limited to a maximum of approximately two car lengths. It was noticed that the trailing car experienced a drag reduction which reached a maximum of 37% at 1.1 car lengths separation and zero lateral offset. This reduction in drag was caused by the trailing car's forward stagnation pressure being reduced due to it being immersed in the leading car's wake. A reduction in drag was also noticed on the leading car when separation between both cars was reduced to close to zero, which was attributed to the increase of the leading car's base pressure due to the proximity of the trailing car's forward stagnation area. Significant changes to the load distribution on the front and rear axles of both vehicles were also noticed at different longitudinal offsets.

Howell (1981) also carried out experimental investigations into the aerodynamic forces that a trailing car is subjected to when following another car. In this study,

two generic and identical Can-Am Prototype race car models without wheels were tested at longitudinal separations between one and two car lengths, at a freestream Re≈$0.7x10^6$ based on the model's length, above a stationary ground plane. The main objective of this work was to determine if the forces experienced by a trailing car, when following another car, were capable of overturning it. Results showed that a trailing car experiences a reduction in lift and drag, with an increase of the pitching moment that in conjunction with its attitude could lead to it overturning when in the wake of the leading car.

Dominy (1990) published the first investigation of Formula 1 cars in tandem. Two quarter-scale models were tested at a constant longitudinal separation of one car's wheelbase and at different lateral offsets, ranging from 0 to 1.25 car widths, at a constant freestream velocity of 20m/s. Due to wind-tunnel size restrictions, the model used to measure both downforce and drag was located above the rolling road, with the leading model located ahead of it. The presented data showed that when the trailing car was fully immersed in the wake of the leading car (no lateral offset), a reduction of up to 36% in downforce and 23% in drag was experienced. A shift in relative axle loading from the front to rear was also reported, an indication that the front wing suffered a greater loss than the rear wing. As the lateral offset between both models was increased, and the trailing car moved out of the leading car's wake, the trailing car's forces gradually recovered to the freestream values, with drag recovering more gradually. The results from this investigation were then used in a vehicle dynamics simulation code to estimate the lap time of the trailing car. According to the results, if the trailing car were fully immersed in the wake of the leading car for a whole lap, it would be slower for the studied track configuration than in the freestream conditions on the same track as the reduction in downforce would lead to lower cornering speeds.

Duncan (1994) carried out a study on the changes in body pressure distribution due to interference between two saloon cars. The author failed to give detailed information about the experimental setup and the limited information available only mentioned the use of two generic car models placed at various drafting and

overtaking positions in a wind tunnel, without quantifying their dimensions. Force measurements showed a decrease in drag of 15% on the leading and 50% on trailing car when the separation between both cars was 150mm.

Dominy et al. (2000a, 2000b) placed a 20%-scale model Le Mans Prototype in the wake of a similar leading car, with a half-car-length separation at a Reynolds number of 1.33×10^6 based on car length. A 30% reduction in downforce and a 16% reduction in drag were noted on the trailing car. Contrary to previous work, a shift of relative load from the rear to the front axle was found. This phenomenon was explained to be caused by different downforce-generating mechanisms on the Le Mans Prototype, compared to a monoposto car. This difference is due to a monoposto car generating downforce through the front wing, rear wing and underbody while in the case of a Le Mans Prototype the majority of the downforce is generated by the underbody, using special tunnels designed to enhance ground effect.

Albers (2003) studied the influence of a leading car on the aerodynamic drag of a trailing car. Two identical generic saloon car models with fixed wheels were placed on a stationary road and their drag was measured at 3 different Reynolds numbers 3.6×10^5, 5.14×10^5 and 6.12×10^6, with separations between 1 and 3 cars' lengths at half-car length increments. The results indicated a reduction in drag of up to 67% on the trailing car and of 14% on the leading car at a separation of one car length and that the drag reduction on the trailing car was independent of the Reynolds number. At 3 cars' lengths the drag on both models returned to the undisturbed values, an indication that there was no longer an interaction between them.

More recently Fiumara (2007) studied numerically the aerodynamic interaction between two generic monoposto cars during an overtaking manoeuvre. Steady-state simulations were carried out at a constant freestream velocity of 50m/s with the cars at different longitudinal and lateral offsets, replicating the longitudinal and lateral offsets seen during different stages of an overtaking manoeuvre. The results showed that at a vehicle separation of 1.5 cars' lengths and zero lateral offset a 5.4% reduction in drag and 12.1% reduction in

downforce was experienced by the trailing car. Similarly to other authors the front wing suffered a greater loss of downforce (20.7%) than the rear wing (16.2%) resulting in a 6.2% shift of axle loading from the front to the rear.

The most recent study was published by Newbon et al. (2014). The authors carried out experimental and computational studies on a quarter-scale Formula 1 car immersed in the wake of a leading car. Using a short bluff body in the experiments and a computational wake generated either by a leading car geometry or by representative inlet conditions, the authors studied the influence of the leading car on the trailing car at inter-vehicle separations ranging from 0.4 to 2 cars' lengths, at a Reynolds number based on car length of 3.1×10^6. The computational results showed poor correlation with the experimental results, with the simulations indicating a reduction of 42% and 15% of downforce and drag respectively at one car-length separation with the experimental results indicating a downforce loss in the region of 60% and no mention of the drag change. As seen by other authors when the separation between cars was increased the reduction in downforce and drag was lower than at smaller separations, with losses of 29% and 6.3% respectively for a separation of 2 cars' lengths.

Table 1-1 lists the works available on vehicle aerodynamic interaction and presents a summary of the methods used.

1.2.2 Vehicle Wakes

Morel (1978) published one of the first works on automotive wakes. The objective of his study was to understand the influence of the base slant angle on the drag of a 3-dimensional bluff body. Using a generic vehicle-shaped body with an adjustable slant angle the author carried out lift, drag and surface pressure measurements for the models at different slant angles. The model was located above a fixed ground plane at a Reynolds number of 1.4×10^6, based on the model's length. The force measurements showed that as the slant angle was increased from 0° to 8° there was a small reduction in C_D, which was caused by an increase in the downwash over the slant and consequent reduction in the wake size. As the slant angle was increased above an angle of

8° C_D increased monotonically until reaching its maximum value at a slant angle of 30°. Above this angle C_D dropped to half the value, it had for the 30° slant angle, and stayed almost unchanged with further slant angle increments. Using smoke visualization and pressure measurements on the slant the author was able to identify two flow regions, one for slant angles below 30°, which was characterized by an attached flow on the last two-thirds of the slant, and a second region characterised by a fully separated flow from the slant. The author also noted the presence of two strong longitudinal vortex structures originating from top side edges for slant angles below 30° while for slant angles above this the structures were no longer present. Pressure data from a horizontal line of pressure taps, placed at the base of the model, showed lower base pressures for slant angles between 8° and 30° than those seen for slant angles above 30°. This lower base pressure is a consequence of the presence of the longitudinal vortex structures and leads to the increase seen in drag for the 8° to 30° slant angle range. Once the slant angle is above 30° drag decreases due to the vortex structures bursting leading to a reduction in vortex drag and also in pressure drag, due to the higher pressure along the base of the model.

Ahmed (1981) studied three generic automotive shapes (estate, notchback and fastback) in an attempt to correlate the wake structure with drag. Experiments were carried out using 25% scale models place above a fixed ground plate at a Reynolds number based on the model length of 4.29×10^6. Oil-flow visualization of the off-body flow along the symmetry plane of the model was done by attaching a vertical plate to the model. Behind the three configurations a region of separation was found in the central plane of the model. These separation regions were split into lower and upper sub-regions of recirculation. In all three cases the lower recirculation region rotated upwards downstream of the rear of the model and the upper region rotated downwards, as seen in regions D and E in Figure 1-2. The height of the sub-regions was found to depend on the shape of the rear of the model with the notchback having both upper and lower recirculation regions of equal sizes, while the fastback and estate had a bigger lower structure compared to the upper structure. Using a 6-hole probe the author identified the presence of a pair of counter-rotating longitudinal vortices,

as shown by region F in Figure 1-2. The author suggested that these structures were generated by the closure of the recirculation vortices seen at the centre plane of the models. These vortices generated upwash at the centre plane of the estate geometry and downwash in the fastback and notchback geometries. Although not mentioned the difference in vertical wash direction will have also been caused by the shape at the rear of the models and the flow behaviour over them. The author also found that the vortical structures generated for the estate slant angle (0°) were weaker and dissipated much quicker than for the fastback slant angle (22.5°) and only equated to 8% of the total drag in the estate compared to 28% for the fastback..

Using the same model as Morel (1978) an analysis into the time-averaged wake structures downstream of a bluff body was carried out by Ahmed et al. (1984). In their study the authors carried out force and pressure measurements, and a wake survey using a ten-hole probe, on a bluff body with different slant angles. The experiments were carried out with the model above a fixed ground plane and at a model-length Reynolds number of 4.29×10^6. As reported by Morel (1978) two longitudinal vortex structures originating from the top edge of the body were identified and a correlation was found between the vortex structure strength and the slant angle, with vortex core strength increasing as the slant angle was incremented. The authors reported that at a slant angle of 30° the flow was unstable and switched between a low and a high drag condition, which was characterized by the flow over the slant being attached for the high drag and separated for the low drag condition.

Combining the findings from the three aforementioned studies provides a direct link between slant angle, vortex strength, drag and flow over the slant.

1. Slant angles below 8° - As the slant angle is increased the flow remains attached to the slant (Figure 1-1 region A) generating downwash that reduces the size of the wake (Figure 1-1 region B) and consequently leads to a reduction in drag. At the same time longitudinal vortices originate from the top side edges (Figure 1-1 region C).

2. Slant angles between 8° and 30° - As the slant angle is increased the vortex strength increases (Figure 1-2 region F), leading to a decrease in base pressure and consequent increase in drag. The presence of the vortex structures also leads to an increase in turbulent mixing along the slant delaying boundary layer separation on the slant.
3. Slant angles above 30° - The vortex structures burst (Figure 1-3 region G) leading to a decrease in drag due to increase in base pressure and a reduction in vortex drag. As the turbulent mixing from the vortex structures and the favourable pressure gradient are no longer present the boundary layer separates from the slant, as shown in Figure 1-3 region H.

The near-wake region behind a bluff body was studied by Bearman (1997). In his study the wake behind a one-eighth-scale generic passenger car was measured using Particle Image Velocimetry (PIV). The results showed a distinct difference between the time-averaged and instantaneous flow structures in the wake. Whilst the instantaneous results indicated that the wake consisted of a great number of unsteady longitudinal vortices and weaker transverse ones, the time-averaged results only showed the existence of two counter-rotating longitudinal vortical structures, similar to those identified by previous authors.

Krajnovic and Davidson (2001) carried out a Large Eddy Simulation (LES) study, in ground effect, using the same generic model as that used by Ahmed (1984) with the simulations being carried out at a model-length Reynolds number of 7.25×10^5. The authors used published experimental data from other researchers as a basis for the comparison with their own results. Despite this, they opted to carry out the majority of their simulations at a different Reynolds number compared to the other authors. Comparisons between LDA data from other sources and the simulations showed good agreement with the normalized velocity profile data downstream of the model. Despite this, the surface pressure predictions were less accurate due to the coarseness of the mesh in certain areas.

Basara et al. (2001) completed a CFD study of various industrial vehicle shapes, obtained from different automotive sources, at undisclosed simulation conditions. The objective of this study was to confirm the effectiveness of the standard κ-ε model and the Reynolds-stress model (RSM). The authors reported that the RSM model was able to predict more accurately the region of separation present at the rear window slant. The RSM was also able to predict that the region of counter-rotating vortices was present on the notchback geometry at the centre plane, similar to the results presented by Morel (1978). The three-dimensional vortex structures reported by both Morel (1978) and Ahmed (1981), as well as the pressure distribution along the top of the models were also predicted more accurately by the RSM than by the κ-ε model.

Zhang et al. (2003a) carried out a study on a bluff body equipped with an underbody diffuser and endplates. In their study the bluff body was placed above a rolling road at different ride heights and force measurements were taken at a Reynolds number, based on body length, of 6.4×10^6. Surface flow visualization and a wake survey using a Laser Doppler Anemometer (LDA) were also carried out. The force measurements showed the body had similar force enhancement and reduction behaviour as an inverted wing in ground effect. From the LDA wake survey the authors identified three different types of vortices created at the bottom of the endplates: (1) concentrated, symmetric with high-axial-speed core, (2) diffused, symmetric with low-axial-speed core, and (3) diffused and asymmetric. The authors suggested that changes to the vortex strength and breakup as ride height was reduced were the cause of the changes noted on the force curve.

Dominy & LeGood (2008) studied the wake of a Nascar and proposed the possibility of using a short bluff body in the wind tunnel as a wake generator in order to recreate the wake without requiring a complete car model. In their study the authors conducted a computational analysis of a complete car and carried out a wake survey using a 5-hole probe on a one-fifth-scale short bluff body resembling the rear section of the computational model. The complete car model simulations were carried out at a Reynolds number of 7.6×10^6 whilst the

wind tunnel model consisted of a 20% scale short bluff body that was tested at a Reynolds number of 1.36×10^6, based on the length of a complete car model. Both computational and experimental results indicated the presence of a pair of counter-rotating vortices, high turbulence intensities, reaching 40% in places, and a low-energy separated flow region at the back of the car with an axial velocity deficit of up to 65% compared to freestream. The authors concluded that there were three wake mechanisms that would affect a trailing car: a velocity deficit, high turbulence levels and local incidence variations. In order to validate their results, obtained using a scale model, the authors compared their data with results from an analysis of the wake of a full-size Nascar, published by Duncan and Golsch (2004), and found good correlation between results, which led to a validation of their method.

Wilson et al. (2008) also studied the possibility of using a short bluff body as a wake generator in the wind tunnel. A wake survey was conducted using a 5-hole probe on a one-sixth-scale Formula 1 car model and on a one-sixth-scale short bluff body representative of the rear section of a Formula 1 car, with a rear wing, diffuser and two rear wheels. The tests were carried out at a Reynolds number based on body length of 6×10^5 with the one-sixth-scale model placed on the rolling road with its wheels rotating, whilst the short bluff body was placed upstream of the rolling road on a stationary surface with its wheels static. Although the ground and wheel dynamics were different between cases the results indicated that the flow from a Formula 1 car was characterized by a pair of counter-rotating vortices originating from the rear wing and a weaker pair of counter-rotating vortices originating from the diffuser. At half a car's length downstream of the model the wake exhibited high turbulence intensities of up to 45% and a velocity deficit of up to 60%, which are similar conclusions to those presented by Dominy and LeGood (2008). The authors stated that due to the similarities in wake structures generated by both configurations, the changes to the flow caused by the stationary ground and wheels were negligible.

1.2.3 Aerodynamics of Inverted Wing in Ground Effect

1.2.3.1 Experimental Studies

The first published comment on inverted wings in ground effect was made by Zahm & Bear (1921) in an investigation of aircraft wings in ground effect. In their study the authors tested a British RAF 6 wing, with a span of 457.2mm and a chord of 76.2mm, at a freestream velocity of 17.7m/s above a stationary ground plane. Among their measurements a data set was obtained with the suction surface of the wing close to the static ground plane. The authors reported for this case a significant increase of force towards the ground plane, which was due to the increase in flow velocity between the wing and the ground and was accompanied by an increase of drag. This data set, as stated by the authors, was taken for completeness rather than practical importance.

For years, studies of inverted wings in ground effect were very limited. In a review of Grand Prix car aerodynamics Dominy (1992) suggested that the performance enhancement in ground proximity was caused by the flow being constrained between the road and the inverted wing, causing it to accelerate and consequently increasing downforce. Although the author's aforementioned explanation for how an inverted wing in ground effect creates downforce was plausible a study was not conducted to prove or disprove the notion.

The first experimental study of the operating conditions of an inverted wing in ground effect was published by Knowles et al. (1994). In this study the forces and pressure distribution were obtained on a single-element GA(W)-1 wing, with a chord of 250mm and an aspect ratio of 3, at a freestream velocity of 25m/s for a range of ride heights and incidences above a rolling road. The authors also carried out 2D inviscid computations, using the panel method, which had good agreement for low incidence angles, where viscous effects were negligible. From this work, it was reported that downforce and drag increased as ride height was reduced, at all incidences. Pressure measurements indicated that as the wing's ride height was reduced the pressure on the wing's suction surface decreased leading to the increase in downforce, corroborating the explanation given by Dominy (1992) for downforce generation on an inverted wing in ground

effect. Also seen in the pressure measurements was a gradual separation of the boundary layer at the trailing edge as ride height was reduced.

A number of experimental and computational studies were conducted by Ranzenbach and Barlow, who investigated both single- and double-element wings in ground effect, over stationary and moving grounds. Two-dimensional studies were conducted at a chord-based Reynolds number of 1.5×10^6 on a NACA 0015 section (Ranzenbach & Barlow (1994)), NACA 4412 section (Ranzenbach & Barlow (1995), Ranzenbach & Barlow (1996)) for the single-element case and a NACA 63_2-215 Mod B section with a 30% slotted flap (Ranzenbach et al. (1997)) for the double-element case. In these studies the incidence was kept constant and the ride height was changed. It was noted that downforce increased as ride height was reduced in all cases. A critical height was identified, where further reduction of ride height caused a decrease in downforce. This was attributed to merging boundary layers from the wing and ground, which reduced the flow velocity on the suction surface of the wing. This effect has subsequently become known as the force-reduction phenomenon (Zerihan and Zhang (2000b), Moryossef & Levy (2004)). The critical height was found to be geometry dependent, and increased with increasing wing camber. On the NACA 0015, NACA 4412 and NACA 63_2-215 airfoils the critical heights were 0.028c, 0.056c and 0.04c respectively, for the moving ground cases. Comparisons between a stationary and a moving ground showed the downforce to be greater for a given height above the moving ground, in all cases. In addition the onset of the force-reduction phenomenon was seen to start at greater heights above the moving ground.

Jasinski & Selig (1998) studied the influence of different endplate and flap configurations on the performance of a UIUC700 double-element inverted wing in ground effect. The investigation was performed at five different Reynolds numbers, between 0.7×10^6 and 1.3×10^6, over a fixed ground. Their study showed that with an increase of Reynolds number there was an increase of downforce coefficient and decrease in drag coefficient for a given incidence, evidence that their wing was susceptible to scaling effects, a phenomenon that

will be described below (Section 1.2.7). It was also shown that the increase of planform area of the flaps increased the total downforce and also increased the main element loading. Even though an increase in downforce and reduction in drag was noted with an increase in endplate size, the conclusions taken are questionable as the change in endplate size was accompanied by a change in endplate geometry, as the position of the endplates with respect to the suction surface of the wing was changed.

Force and pressure measurements were taken at different incidences and heights above a rolling road on a Tyrrell 026 single-element wing by Zerihan & Zhang (2000a), at a chord-based Reynolds number of 2.0×10^6. As shown by previous authors, an increase in downforce with decreasing height was noted. As the wing was lowered towards the ground the rate of downforce increase started to drop, at which point the pressure distribution indicated that the wing's boundary layer had started to separate at the trailing edge, a phenomenon also linked to the increase in drag. With further reductions in height the separation point gradually moved forward until the height of maximum downforce was reached and the flow separated over most of the wing. Based on the surface pressure it was proposed that at close proximity to the ground the pressure recovery behind the throat, created by wing and ground, was too steep for the flow to continue attached, leading to the downforce reduction.

Continuing with their earlier work, Zerihan and Zhang (2002) studied a double-element wing at two different flap incidence settings and at different ride heights above a rolling road. In this study the authors used a modified GAW two-element wing with endplates, a span of 1100mm and a combined aspect ratio of 2.89. Force and pressure measurements were taken and a LDA flow survey made at a chord-based Reynold number of 0.765×10^6. The force measurements showed that, despite a significant increase in downforce with the highest flap incidence, both flap configurations displayed similar behaviour to the single-element wing as ride height was decreased. The authors also reported an increase in wake thickness and velocity deficit behind the main element, which was caused by the boundary layer separating at the trailing

edge of the wing as the ride height was reduced. The main element was also found to create most of the downforce and was dominant in the development of the turbulent wake. It was noted that the wake from the flap was not significantly affected by ground proximity and that increasing the flap angle proved to increase the velocity deficit and wake thickness.

The wing-tip vortices from a Tyrrell 026 wing with endplates, in ground effect above a rolling road, were studied by Zhang et al. (2002). In this study, LDA and PIV surveys were made to measure the wing-tip vortices generated by the wing. The tests were carried out on a wing, with a span of 1100mm and a chord of 223.4mm, at a chord-based Reynolds number of 0.462×10^6. It was reported that at greater ground clearance vortex shedding was present on the wing's trailing edge, but once time-averaged (via LDA measurements) it showed a small wake growing and moving upwards as it moves downstream. As the ground clearance was reduced the boundary layer started separating on the trailing edge of the suction surface, and gradually moving towards the leading edge with further ride height reductions. It was also shown that close to the height of maximum downforce the rate of change of downforce was a function of vortex strength. Vortex-induced suction was attributed as the cause of the change in the rate of downforce increase as ride height was reduced, due to the onset of vortex breakdown being reached before the height of maximum downforce. The vortices' upwash was also observed to effectively reduce the flow incidence close to the wing tip, delaying separation on the suction surface. Below the maximum downforce height the vortex broke down and the upwash disappeared leading to flow separation on the wing, resulting in a reduction in downforce.

Soso and Selig (2002) studied the influence of endplate design on wing performance for a low-aspect-ratio wing with endplates. In their study they used a UIUC700 two-element aerofoil with a span of 925mm and a geometric aspect ratio of 2.88, which was computationally tested at a chord-based Reynolds number of 1.45×10^6. Different endplate configurations were studied by increasing the height and chord ahead of the wing's leading edge. The results

indicated that the endplate height had a significant influence on the effective aspect ratio of the wing. It was reported that an increase in endplate height by 40% led to an increase of the wing's effective aspect ratio by 7.29%, whilst increasing the endplate chord by 61.7% in the upstream direction only increased the effective aspect ratio by 1.27%.

A further study on wing tip vortices was performed by Galoul & Barber (2007). The authors tested a Tyrrell 026 wing with endplates, with a span of 130mm and a chord of 75mm, placed 35mm above a rolling road, at a chord-based Reynolds number of $5.0x10^4$. In their work, two distinct trailing vortices were identified downstream of the endplate. The first one was a stronger vortex forming on the suction surface of the wing and a second smaller one formed on the pressure surface along the top outer tip of the endplate. In their study a flow survey was made downstream of the wing using LDA in order to analyse the vortices' behaviour. It was noted that the smaller vortex did not have an influence on the stronger vortex. While the stronger vortex pulled the weaker one towards it until they eventually merged between one and two chords downstream. The authors concluded that the moving ground had no influence on the behaviour of the vortices. However as the measurements were taken at a single height this conclusion may be questionable.

A study of separation suppression using dimples was performed by Beves (2009) using a Tyrrell 026 wing in ground effect at different incidences and ride heights, above a rolling road. The wing had a span of 230mm and a chord of 75mm and was tested at a chord-based Reynolds number of $0.5x10^5$. For this study different dimple array configurations were machined into the wing's suction surface at different chordwise locations. The results showed a reduction of wake velocity deficit and thickness with three rows of dimples located at the peak suction region of the wing and with the smallest inter-dimple separation, of the studied configurations. From these results it was suggested that with the three rows of dimples the dimple vortex shedding produced enough streamwise vortices that reattached the flow on the majority of the wing's suction surface. Further tests with five rows of dimples showed a greater wake velocity deficit

than verified on the three row configuration. This was thought to be caused by the greater vortex interaction caused by the extra vortices being generated.

Another study on flow separation control was carried out by Kuya et al. (2009) on an inverted Tyrrell 026 wing using vortex generators above a rolling road. A wing with a span of 1100mm and a chord of 223.4mm was tested at a chord-based Reynolds number of $4.5x10^5$ at different ride heights. In their study counter-rotating sub-boundary layer, large-scale counter-rotating, and sub-boundary layer co-rotating vortex generators were used. Wing incidence was changed from 1 to 17 degrees and surface pressure distributions were recorded. It was reported that the vortex generators had an effect on controlling flow separation in the adverse pressure gradient region leading to increases in downforce, particularly for low angles of attack ($\alpha<5$ degrees) and ride heights ($h/c<0.12$) and for angles of attack between 5 and 10 degrees at ride heights between $h/c=0.150$ and $h/c=0.200$. The counter-rotating vortex generators were shown to give the biggest improvement, with downforce increasing by up to 26% and the lift-to-drag ratio (L/D) increasing by 10%. They were also shown to eliminate the region of separated flow on the suction surface of the wing. The results indicated that the co-rotating vortex generators caused the wing's performance to deteriorate and were unable to change the separated boundary layer region.

Van den Berg and Zhang (2009) observed changes to the performance of a wing operating in close proximity to the front wheels of a monoposto car. In his study the gap between wing and wheel remained constant whilst the wing's ride height was changed. The wing used in their study was an LS(1)-0413 MOD with a flap and endplates, having a total chord of 284mm and a span of 580mm; the tests were carried out at a chord-based Reynolds number of $1.4x10^5$. The results showed that at lower ground clearances ($h/c<0.15$) the proximity of the wheels enhanced the wing's performance whilst at greater ride heights the wing's performance was reduced. Using PIV the authors identified a phenomenon they named the "channeling effect" that is caused by the increase in blockage from the wheel, combined with the direction of the wheel rotation

helping extract air from under the wing, which leads to the flow being accelerated and consequently improving the wing's performance. This effect led to a flow velocity increase of 3.8% at mid-span. When the wing was placed above the wheel centreline a reduction in wing performance was found. This was reported to be caused by the fact that above the wheel centre line the wheel surface is moving upstream and altering the flow, leading to a decrease in mid-span velocity of 27%. From this study 3 main wing/wheel interaction phenomena were identified:

- Separation Effects – the presence of the wheel leads to a delay in the separation caused by low ground clearances, meaning that the onset of separation starts at lower ride heights. Also the adverse pressure gradient caused by the wheel blockage leads to the separation of the tip vortex from the flap.
- Vortex Effects – the presence of the wheel reduces the undesired sudden performance change due to tip vortex breakdown and consequent reduction of vortex-induced suction.
- Wheel Circulation Effect – below the wheel centreline the wheel rotation increased the flap loading in the spanwise region in front of the wheel, whilst decreasing it when the wing was above the centreline.

The influence of a ground boundary layer on the performance of an inverted wing in ground effect was reported by Marshall et al. (2010). In this work the authors used a GA(W)-1 wing that had a chord of 147mm and a span of 515mm, and was tested at a chord-based Reynolds number of 2.5×10^5. The wing was placed above a splitter which was the full width of the test section, but with different upstream lengths, from the leading edge of the wing, in order to generate different ground boundary layers. Pressure measurements and an LDA survey were carried out on the wing at a range of ride heights above a fixed ground and with different boundary layer thicknesses. Although there were significant changes to the pressure distribution on the suction surface of the wing no changes were reported on the pressure surface. As the ground boundary layer thickness was increased the pressure on the suction surface also increased, due to a reduction of the flow speed between the road and the

wing. An LDA survey showed that in close proximity to the ground (h/c<0.2) both the wing wake and ground boundary layer merged, further reducing the flow speed on the suction surface of the wing.

1.2.3.2 Computational Studies

The first published computational study of inverted wings in ground effect was by Katz (1985). In this study a single-element wing in ground effect was modelled using the panel method, with the ground represented by the mirror-image technique. Downforce was shown to increase asymptotically with the reduction of ride heights. However, since viscous effects were not modelled the downforce reduction was not evident. Using the same method, Knowles et al. (1994) modelled a GA(W)-1 wing in ground effect. The computational results were compared with experiments and reasonable agreement was only obtained at low incidence angles and at ride heights above h/c=1, when viscous effects are negligible.

As well as reporting experimental results Ranzenback and Barlow (1994, 1995, 1996, 1997) also made computational studies on an aerofoil in ground effect using a RANS solver with turbulence modelled by the κ-ε model. The single-element aerofoil results were similar to the experimental results above h/c=0.1. Below h/c=0.1 the results showed the computed downforce being greater and drag matching the experimental results. On the double-element configuration the computational results showed less downforce and more drag than experimentally, throughout the ride height range. From the analysis of the computational results and due to their similarity with the experimental results, the authors considered the hypothesis of the downforce reduction being caused by ground and wing boundary layer merging as valid in both the stationary and moving ground cases. The development of the floor boundary layer was explained to be caused by the local acceleration of the flow between the wing and the ground.

In an attempt to select a valid turbulence model a series of computational simulations was made by Zerihan & Zhang (2001) using a Tyrrell 026 aerofoil at a chord-based Reynolds number of 4.6×10^5. The computational pressure

distribution results were compared with the mid-span pressure measurements obtained experimentally by Zerihan & Zhang (2000a), on a wing of the same geometry. The results showed that both turbulence models that were tried (κ-ω SST and Spalart-Allmaras) gave slightly lower pressure on the aerofoil's suction surface at h/c=0.671 and h/c=0.448, than those recorded experimentally. At h/c=0.224 and h/c=0.134 the κ-ω SST model results matched the ones obtained experimentally and the Spalart-Allmaras model results gave a lower pressure on the aerofoil's suction surface than recorded experimentally. Further comparisons between the computational wake downstream of the wing with the experimental results by Zerihan & Zhang (2000a) showed that the computational wake was thicker and had a greater velocity deficit. Although both turbulence models gave similar wake results the κ-ω SST model was unable to model the ground boundary layer correctly.

A computational study on a GA(W)-1 aerofoil in ground effect was conducted by Lawson et al. (2002) using a RANS solver with turbulence modelled by the Spalart-Allmaras model. The aerofoil had a chord of 247mm and the simulations were carried out at a chord-based Reynolds number of 6.9×10^5. The results were compared with PIV and surface pressure measurements obtained experimentally in the wind tunnel, with the wing above a rolling road at different incidences and ride heights. The results showed good agreement between experiment and computation for α=0° at h/c=0.1 and h/c=0.47. For α=15° the computational results predicted a thinner boundary layer and a later boundary layer separation, which was not present in the wind tunnel. The authors attributed this discrepancy to poor modelling of wind tunnel conditions, i.e., turbulence level, boundary layer suction and road surface roughness.

A series of two-dimensional computational simulations comparing results from six different turbulence models was performed by Mahon & Zhang (2006). The aerofoil sections of the main and flap elements were the same as used by Zerihan & Zhang (2002) and were modelled in ground effect above a moving ground at a chord-based Reynold number of 7.86×10^5. The results showed that all turbulence models predicted accurately the pressure distribution on the

wing's surfaces in the range of ride heights. The κ-ω SST model gave the most accurate results as they were nearly identical to the experimental results obtained by Zerihan (2001). The authors reported that the majority of the downforce was produced by the main element while the majority of the drag was produced by the flap.

A Tyrrell 026 aerofoil in ground effect above a moving ground was studied at different ride heights using a RANS solver with turbulence modelled by a one-equation model by Moryossef & Levy (2004). The wing was set at a constant Reynolds number of $4.5x10^5$ and incidence, and the results were compared with experimental data obtained by Zerihan and Zhang (2001). The results showed very good agreement between computational and experimental surface pressure distributions above h/c=0.448. Below this height the computational results showed a decrease in pressure on the suction surface of the wing, with the error increasing with further ride height reductions.

Soso and Phillips (2004) investigated the changes to the downforce curve of a double-element aerofoil in ground effect above a moving ground. A UIUC700 two-element wing, with a chord of 200mm and an undisclosed span or aspect ratio, was studied at different ride heights, with both elements at different angles of attack and at a chord-based Reynold number of $1.4x10^5$. A decrease in the maximum downforce and an increase of the ride height at which it occurs were reported as the main element angle of attack was increased. An increase in wake thickness and a softer stall with the increasing main-element angle of attack were also noted. Increasing the flap angle offset the downforce curve upwards but did not alter the shape of the curve significantly. Downforce reduction was attributed to flow separation from the wing's main-element, as none of the results indicated both ground and wing boundary layer were merging.

A study into the optimum chord length for each element of a two-element wing was carried out by Goto and Sakurai (2006). Using the same FX63-137 aerofoil section for both elements the authors carried out a series of simulations, at a chord-based Reynolds number of $7.3x10^5$, where the chord of each aerofoil was

changed while the total chord was kept constant at 304.8mm. The results showed that maximum downforce was achieved with flap chord values between 0.4c and 0.7c of the wing assembly's chord, whilst in order to achieve minimum drag a shorter flap chord, between 0.25c and 0.3c, was required.

An inverted aerofoil in ground effect was modelled by Molina & Zhang (2010) to investigate the aerodynamic behaviour of a heaving wing above a moving ground, using a URANS solver with turbulence modelled by the Spalart-Allmaras model. The aerofoil that was investigated had the profile from the main element of a double-element wing configuration previously used by Mahon (2006). The aerofoil had a chord of 139mm and simulations were carried out at a chord-based Reynolds number of 3.9×10^5 with a constant incidence and at different heaving frequencies. The results showed three different mechanisms that increased the aerofoil's lift coefficient. At low frequencies the increase was due to ground effect, as the flow accelerates between the wing and ground. At medium frequencies the increase was caused by the heaving motion altering the angle of incidence of the aerofoil, due to the vertical velocity component of the aerofoil. And at high frequencies the increase was caused by the vertical acceleration of the aerofoil, which led to an increase in downforce proportional to the acceleration.

With the objective of investigating and capturing the complex flow around an inverted double-element wing in ground effect, Bruckner & Zhang (2010) conducted a computational study using the detached eddy simulation (DES) method. Simulations on the same wing geometry as used by Mahon & Zhang (2006) were carried out at a chord-based Reynolds number of 5.8×10^5 at different ride heights; downforce, pressure distribution and flow vorticity were validated against experimental work and Steady Reynolds-Averaged Navier Stokes (SRANS) simulations. DES captured throughout the ride height range the tip vortices' breakdown, the influence on force behaviour and their increasing unsteadiness as ride height was reduced. Both DES and SRANS gave similar results but at h/c=0.211 DES was more accurate in predicting the trend of downforce while SRANS predicted vortex breakdown accurately. DES

also predicted more accurately the tip vortices formed on the suction surface and pressure surface.

1.2.4 Wings in Turbulent Wakes

Soso and Wilson (2006, 2008) published the first studies of inverted wings in ground effect and simultaneously in the wake of an upstream body. Surface pressure at three spanwise locations and forces were recorded at a chord-based Reynolds number of 3.01×10^5 on a single element GA(W)-1 wing, with a chord and span of 250 and 550mm respectively, which was placed above a rolling road. Located upstream of the wing, at a nominal separation of 1.5 car lengths ($x/c \approx 9.82$), was a bluff body with a diffuser and wing to replicate the main flow features of a race car wake. The results showed a reduction in downforce similar to the findings reported by Dominy (1990, 2000), but the reported increase in drag contradicted Dominy's results. The surface pressure results indicated that the reduction in downforce was greater at mid-span. This was reported as being due to the upwash and lower dynamic pressure in the bluff body's wake. The increase in drag was considered to be caused by the downwash created by the counter-rotating vortices, produced by the upstream body's diffuser. These increased the effective incidence angle towards the tips of the wing leading to an increase in induced drag. Changes to the flow on the wing surface were also noted. These were characterized by an earlier laminar-to-turbulent transition and the elimination of the separation bubble.

More recently Wilson et al. (2008) studied the possibility of reproducing a Formula 1-type wake, by using a generic Formula 1-type bluff body in a wind tunnel. Force measurements were taken on a GA(W)-1 wing, with a chord of 250mm and a span of 600mm, at different incidences in the wake of a generic Formula 1 bluff body at a separation equivalent to a half-car length and at a chord-based Reynolds number of 1.2×10^5. The results showed a reduction of up to 50% in downforce and up to 25% in drag. Further tests were conducted to establish the influence of oncoming flow turbulence on the wing's performance. In these tests turbulence was generated by a turbulence grid which did not generate the trailing vortices or upwash evident in the bluff body's wake. From

the results it was concluded that the turbulence delayed separation on the wing's surface, leading to an increase in downforce. It was suggested that this increase in downforce due to oncoming flow turbulence was counteracted by an increase in velocity deficit caused by the lower axial velocity, as shown in Figure 1-4, and upwash generated by the upstream body, as seen in Figure 1-5, which reduced the effective angle of attack leading to the reduction in total downforce. The drag reduction, which contradicts Soso and Wilson's (2006, 2008) findings, was suggested to be caused by the lower dynamic pressure in the wake.

1.2.5 Freestream Turbulence

Experiments were carried out by Hoffman (1990) in an attempt to understand the influence of freestream turbulence on the aerodynamic performance of a wing out of ground effect. In his study a rectangular NACA 0015-section wing with a chord of 154mm and an aspect ratio of 2.9, was tested at a chord-based Reynolds number of 2.5×10^5 at different freestream turbulence levels from 0.25% to 12% and at a range of angles of attack from -5 to 35 degrees. Different freestream turbulence intensities were obtained by using different unidirectional rod configurations spanning the wind tunnel test section. Results showed that turbulence intensities up to 9% did not alter the slope of the lift curve, but an increase in maximum lift of up to 30% was noted. The increase in turbulence intensity was also shown to change the angle of attack at which the maximum downforce is obtained from 23° to 33°. Although oil flow visualisation results highlighted the existence of a separation bubble and separated boundary layer at the trailing edge at low turbulence intensities, no significant changes were reported on drag.

The influence of freestream turbulence on the aerodynamic performance of wind turbine blades was studied by Deviant et al. (2002). In their study a NACA 65_4-421 aerofoil, with a chord of 300mm and a span of 1100mm, was subjected to different freestream turbulence intensities ranging from 0.5% to 16% at chord-based Reynolds numbers from 1.0×10^5 to 7.0×10^5 and at angles of attack ranging from 0° to 90°. By using a grid of tubes upstream of the test section the authors were able to change the turbulence intensity. Similar to previous

authors, a delay in separation and an increase in the maximum lift were reported. A slight change in the lift curve slope at low angles of attack was also noted but the overall shape of the curve remained unchanged.

Watkins et al. (2010) carried out a study of the influence of freestream turbulence on wings at low Reynolds numbers. In their study a symmetric flat plate aerofoil was used with a chord of 150mm. Tests were conducted at a Reynolds number of $7.5x10^4$ with a freestream turbulence intensity ranging from 1.2% to 12.6%, for angles of attack from -25° to +25°. Force data obtained from integrating surface pressure measurements indicated that for angles between 0° and 12° lift was greater at turbulence intensities below 7.5%. For angles above 12° and turbulence intensities above 7.5% lift was greater. Although drag results were not presented the increase in lift at high turbulence intensities and angles of attack indicates that the boundary layer remained attached.

Whilst studying the use of a short bluff body in the wind tunnel as a way of simulating the wake generated by a Formula 1 car, Wilson et al. (2008) proposed that one of the flow mechanisms affecting a wing in the wake of a leading body was the increase of freestream turbulence, which would lead to a delay in separation of the flow from the surface of a trailing wing. In order to prove this theory a grid of tubes creating a turbulence intensity of 8%, at the leading edge of the trailing wing, was placed upstream of the test section. From the experiment an increase in downforce was noted for angles of attack above 12°. This was explained as being caused by a delay in separation of the boundary layer from the suction surface of the wing at high angles of attack, as a consequence of the mixing between the turbulent flow and the boundary layer.

1.2.6 Wings in Yaw or Roll

As a race car negotiates a track it will experience a variety of flow conditions. Although during their development cars are tested in a wind tunnel, the flow on the race track may not match the flow in the wind tunnel. When driving around a track a car will be influenced by other cars, cross-winds and changes in attitude such as pitch, roll and yaw, due to acceleration and irregularities on the track.

Limited research has been carried out on different wing attitudes other than pitch, i.e., changes in angle of attack. The first study mentioning a vehicle in yaw was published by Duncan (1994). In his study a generic stock car model was placed in the wind tunnel at various yaw angles and pressure was measured at various points around the body. The author reported that changes in yaw angle led to an increase of rear downforce and total drag. In the study, limited information was presented on both the experimental setup and the model geometry, but it is believed that the changes to the forces were geometry specific, as the model had a rear deck spoiler, and cannot be carried over to other models.

A study by Gogel (2007) looked at the influence of yaw on the performance of a monoposto-type rear wing. In his study a Swift Engineering Toyota Atlantic Series single-element wing with sharp-edged, rectangular endplates was studied computationally at different yaw angles, from 0 to 20° in 5° increments, at a chord-based Reynolds number of 4.3×10^5. He found that the windward endplate inner edge showed a flow separation which affected the flow over the wing in the streamwise direction. A decrease in downforce of 0.51% was reported at 5° yaw and 11.7% at 20° yaw. No drag data were presented but it was mentioned that drag presented no discernible difference at the different yaw angles. An increase in static pressure was noted on the entire suction surface, and a reduction in the pressure in the wake of the windward endplate. The reduction in downforce and changes in pressure were attributed to a blocking effect on the flow caused by the endplate. Further to this study, different endplate configurations were tested to analyse their sensitivity to yaw. The results indicated an improvement in performance caused by adding slits on the endplate on the pressure surface. The size of the endplate and its extension in the upstream direction with respect to the wing leading edge showed that, although the flow still separated on the windward inner edge, the endplate extension allows for the flow to reattach before reaching the wing leading edge.

An inverted wing in ground effect will experience roll whilst cornering, due to vehicle roll, as well as in a straight line condition, due to track surface

irregularities. Although no study has been carried out on this operating condition, it is important to understand it as whilst cornering the wing will suffer from asymmetric loading and flow structures that will influence the flow around components downstream of the wing.

1.2.7 Scaling Effects

Although the standard approach to vehicle wind tunnel testing is to use scale models, the use of these may lead to results which differ from those experienced by the actual component. These are caused by differences in the boundary-layer transition location between the model and the actual component (Mabey (1991)).

Braslow and Knox (1958) presented a simple method for boundary-layer transition fixing by using grit. The method calculates the correct grit size for boundary layer transition fixing at specific locations on sub-scale aerodynamic components in wind tunnels. In their report the authors did not mention the pattern, density or length of the transition strip, hence the approach is open to different interpretations.

The existence of separation bubbles with reattachment has been reported when testing sub-scale models both on general aviation wings (Tani (1964)) and on inverted wings in ground effect (Zerihan (2001), Soso (2005)). These separation bubbles appear when a laminar flow encounters a strong adverse pressure gradient, separates and then reattaches. The reattachment can be of laminar nature if the flow does not transition to turbulent and will only occur if in the presence of a favourable pressure gradient. In the case of a turbulent reattachment the flow will have transitioned to turbulent whilst separated and will reattach whether in a favourable or unfavourable pressure gradient.

A study of the influence of Reynolds number on the flow separation on a two-dimensional aerofoil was conducted by Mueller & Battil (1982). In their study a NACA 66_3-018 aerofoil was tested at different angles of attack and at chord-based Reynolds numbers from 4.0×10^4 to 4.0×10^5. In their study a decrease in the bubble length was shown to occur as the Reynolds number was increased.

Further research into the dynamics of laminar separation bubbles at different Reynolds numbers was carried out by Diwan & Ramesh (2007). In their study a laminar separation bubble was created on the surface of a flat plate by inducing an adverse pressure gradient through the use of a contoured wall above the flat plate. Data were obtained using a hot-wire anemometer and surface flow visualization. The results indicated that both the length and height of the bubble decreased with the increasing Reynolds number, due to the flow transitioning to turbulent further upstream and increasing the mixing with the separated boundary layer as the Reynolds number is increased. Further analysis of the results indicated that the height of the bubble reduces at a greater rate than the length as the Reynolds number was increased, thus altering the aspect ratio of the bubble.

A study on the aerodynamic performance of a NACA 2415 aerofoil at low Reynolds numbers was carried out by Genc et al. (2012). The experiments were undertaken using a wing with a chord of 180mm and a span of 290mm at a chord-based Reynolds numbers between $0.5x10^5$ and $3x10^5$, with the wing's incidence set to angles of attack ranging from -12° to 20°. Force measurements were taken and surface flow visualization carried out. A more gradual stall was noted as the Reynolds number was increased and from the surface flow visualization it was apparent that the onset of separation moved towards the leading edge of the wing as the Reynolds number was increased.

Hu & Yang (2008) studied the transient behaviour of a laminar separation bubble on a GA(W)-1 wing with a chord of 101mm at different angles of attack and at a constant chord Reynolds number of $7.0x10^5$. Surface pressure was acquired and a flow survey was carried out using PIV. Both PIV and pressure data showed a laminar boundary layer separating from the wing surface at angles of attack above 8°. It was found that laminar-to-turbulent transition was quick and the flow reattached to the surface of the wing, resulting in the formation of the separation bubble with turbulent reattachment. The reattached turbulent boundary layer was more energetic, thus more capable of advancing without further separation. As the angle of attack was further increased it was

noted that the bubble moved towards the leading edge and the bubble length (0.2c) remained unchanged. The results also indicated that the existence of the separation bubble reduced the rate of lift increase. Separation of the boundary layer from the entire wing surface occurred at angles of attack above 12° when the separation bubble burst suddenly causing the aerofoil to stall.

1.3 Research Aim & Objectives

Studies carried out on inverted wings in ground effect have focused mainly on the influence of ride height and angle of attack on the forces, pressure distribution and flow features when the wing is operating in undisturbed flow. Hence, only a limited number of studies have been carried out on inverted wings operating both in ground effect and in a turbulent wake simultaneously. The wings used in these studies were single-element types that did not represent a Formula 1-type wing. As shown in Figure 1-6, a Formula-1-type wing assembly consists of a full-span main wing with two identical flaps, or a multi-element flap cascade of smaller spans, located on each side of the main element leaving a void between both flap inner ends. This leads to more complex flow structures than those seen on single-element or simple double-element wings used in previous academic work. Although a more complex wing is of interest in order to study these complex flow structures the reality is that a jump to a Formula-1-type wing might be too big a leap in the knowledge base and leave blanks between the simple and complex wing geometries. This way a compromise is required in the wing geometry that allows us to add to the knowledge of inverted wings in ground effect, without the complex flow structures associated with the Formula-1-type wing.

The literature survey also highlighted the absence of fundamental studies of the influence of roll and yaw on the performance of an inverted wing in ground effect. Due to the geometry and surface of a race track a car is rarely in levelled conditions hence the wing is constantly at different attitudes that have an influence on its performance.

Through the analysis of the available literature the overall aim was drawn as an attempt to understand the effects of real on-track performance-limiting factors of

a race-car front wing including roll, yaw and immersion in the wake of a leading car.

In order to achieve the aim of this study the following objectives were set:

- To investigate the aerodynamic performance of a simplified Formula-1-type-wing in ground effect, using the data set as a reference for subsequent cases.
- To investigate the dominant flow structures present in the wake of a simplified Formula-1-type car and seek an understanding of the potential influence they play on a body travelling in the wake.
- To investigate the change in aerodynamic performance of a wing in ground effect when traveling immersed in the wake of a Formula-1-type car.
- To investigate the individual influences of roll and yaw on the aerodynamic performance of an inverted wing in ground effect.

Table 1-1: Previous studies on vehicle aerodynamic interactions

Author(s)	Year of publication	Type of study	Type of ground	Scale	Type of car	Type of wheels	Inter-car position changes
Romberg et al.	1971	Experimental	Fixed	3/8th	Saloon	Fixed wheels	Longitudinal separation and lateral offset
Howell	1981	Experimental	Fixed	1/12th	Prototype	No wheels	Longitudinal separation
Dominy	1990	Experimental	Moving	1/4th	Monoposto	Rotating wheels	Offset and fixed longitudinal separation
Duncan	1994	Experimental	Fixed	N/A	Saloon	N/A	Longitudinal separation and lateral offset
Dominy et al.	2000a,b	Experimental	Moving	1/5th	Prototype	Rotating wheels	Fixed separation
Albers	2003	Experimental	Fixed	1/25th	Saloon	Fixed wheels	Longitudinal separation
Fiumara	2007	Computational	Moving	1/1	Monoposto	Rotating wheels	Longitudinal separation and lateral offset
Newbon et al.	2014	Computational	Moving	1/6th	Monoposto	Rotating wheels	Separation

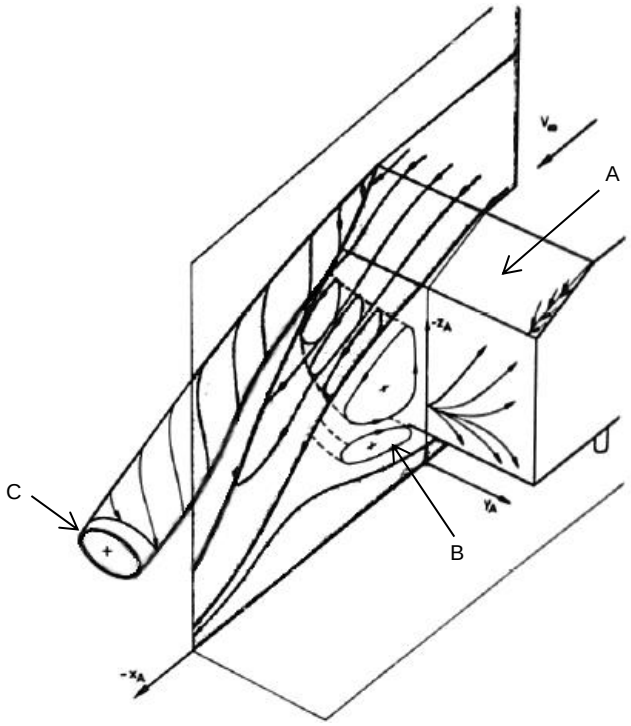

Figure 1-1: Flow features behind generic vehicle-shaped body for slant angles below 8°. Image adapted from Ahmed et al. (1984)

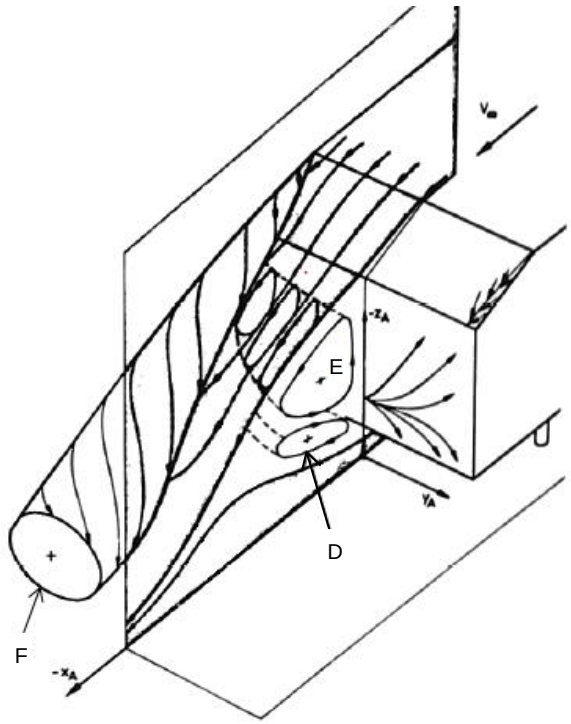

Figure 1-2: Flow features behind generic vehicle-shaped body for a slant angle between 8° and 32°. Image extracted from Ahmed et al. (1984)

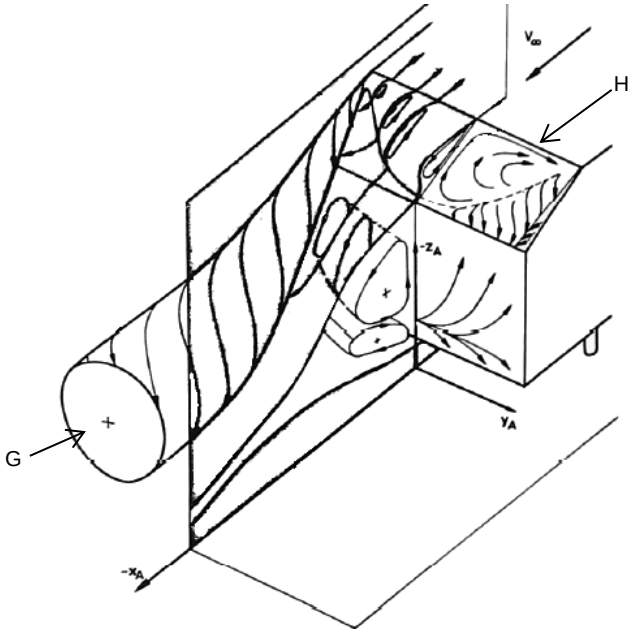

Figure 1-3: Flow features behind generic vehicle-shaped body for slant angles above 32°. Image extracted from Ahmed et al. (1984)

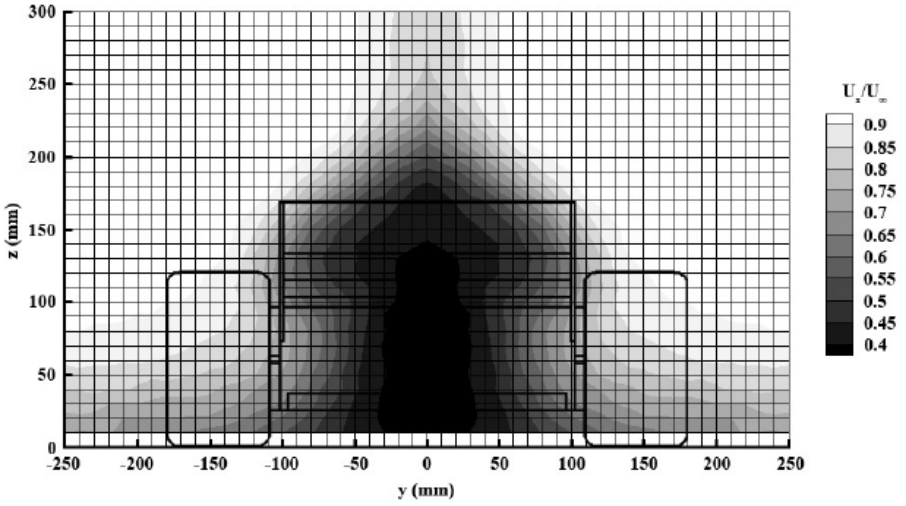

Figure 1-4: Contour of normalized axial velocity at half-car length downstream of wake-generating model. Plot extracted from Wilson et al. (2008)

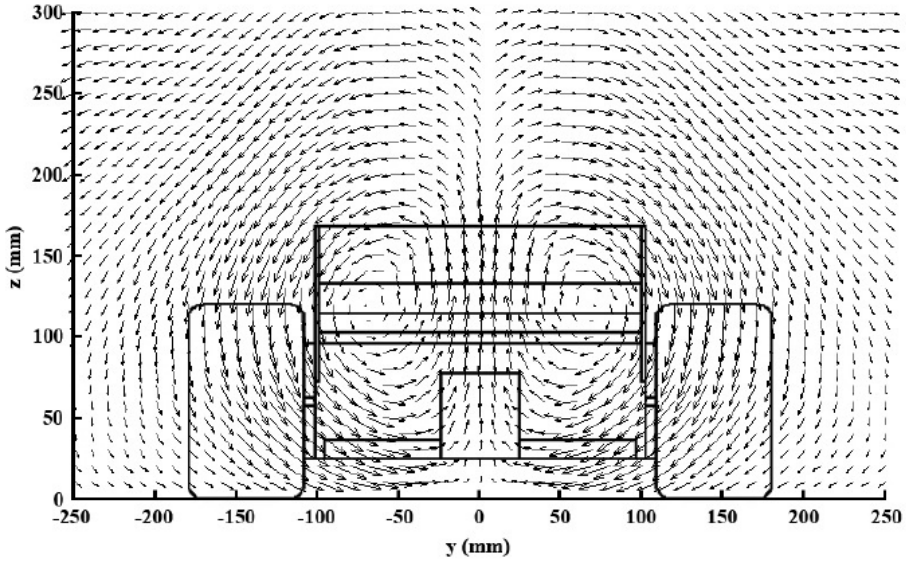

Figure 1-5: X and Y velocity vectors at half-car length downstream of wake-generating model. Plot extracted from Wilson et al. (2008)

Figure 1-6: Formula 1 multi-element wing

2 Research Procedure

In line with the aims and objectives outlined in Chapter 1, an experimental programme was set up in a wind tunnel. The front wing on a Formula 1-type car is the first element to come into contact with the oncoming flow, making it possibly the most important aerodynamic component as the rest of the car operates downstream of it and its wake. Despite this, the front wing, is also influenced by other components around it. These components such as the wheels, brakes ducts, suspension elements, nose cone, etc. influence the wing's performance as they create pressure gradients that may be beneficial or detrimental to the wing's performance. These interactions introduce a level of complexity that was not in the interest of this study, as there were still gaps in the knowledge base that required understanding before progressing into a study an analysis of them. This way, to minimize these complex aerodynamic interactions it was decided to focus on the performance of an isolated front wing, rather than a complete car. This enabled individual effects of the leading car's wake on the front wing of the trailing car to be isolated, without having to investigate the interactions between the wing and other components. Because of this simplification the results from this work can be used as a reference for future studies aimed at further understanding the realistic behaviour of a front wing mounted on a car, when travelling in the wake of a leading car.

To compensate for an equipment failure, a numerical study was also conducted using the experimental data to validate this approach. In this chapter the wind tunnel facilities and models will be described, as well as the experimental and numerical approaches. Detailed information on the wind tunnel, model geometries, uncertainty analysis, and experimental and numerical test conditions can be found in Appendices A, B, C and D respectively.

2.1 Wind Tunnel Facilities

2.1.1 Tunnel

The experiments were carried out in Cranfield University's DS Houghton wind tunnel at the Defence Academy of the United Kingdom in Shrivenham. This is a

closed-return, three-quarter open-jet wind tunnel, as shown in Figure 2-1 and Appendix A, and was equipped with a continuous-belt rolling road ground simulation synchronized with the freestream velocity. Suction was applied under the belt to prevent it from raising due to the aerodynamic forces created by the wing, and any belt expansion. Boundary-layer suction was applied through the floor ahead of the rolling road to remove the wind tunnel boundary layer. Optimization of the level and distribution of the suction, coupled with a knife-edge transition to the belt, ensured minimal belt boundary layer (Knowles and Finnis (1998)). The wind tunnel was equipped with a computer-controlled support sting incorporating an automated motion control system to adjust the ride height of the model above the rolling road during the experiments, to within ±0.05mm of the requested ride height.

The wind tunnel was controlled by a Pi Mistral system. This system controlled the wind tunnel operating parameters and data logging. It also allowed for test templates to be created that controlled the test parameters, such as model ride height, wind and road speed, boundary layer and belt suction, and exported the logged data to the post-processing software.

2.1.2 Test Conditions

All experiments were conducted at a nominal freestream velocity of 25m/s, giving a Reynolds number of 4.45×10^5, based on the wing's chord. A turbulence intensity, for the undisturbed flow cases, of 0.7% was measured in the test section using a hot-wire anemometer at the leading edge location of the wing used in this study. The air and road temperatures were maintained at a constant 25°C during the runs, through the use of the wind tunnel and rolling road heat exchangers. The rolling road boundary layer thickness was calculated to be approximately 1.58mm at the leading edge of the wing, using the turbulent boundary layer thickness equation and the measured data in the DS Houghton wind tunnel available in Knowles (2005) as a starting point.

Due to the dimensional limitations imposed by the wind tunnel test section the wake-generating model was placed ahead of the rolling road on the boundary layer suction box, for the disturbed flow cases. Because of the influence the

boundary layer suction would have on the flow under the model and consequently on the wake-generating model's wake it was decided to run the disturbed case experiments with the boundary layer suction turned off. A similar solution was used by Wilson et al. (2008) in their studies, where the leading wake-generating body was placed on a stationary ground plane ahead of the rolling road. The authors compared the wake generated by the model placed on the rolling road with the wake generated with the model ahead of the rolling road, placed over a stationary ground plane, and concluded that the changes caused by the stationary ground plane had a negligible effect on the wake shape.

2.2 Models

2.2.1 Wing

The front wings used in motorsports are normally highly complex three-dimensional geometries that can contain twist, taper, varying aerofoil sections, sweep and complex features that generate secondary flows. For this study such a wing was considered to be inappropriate, since gaps in the literature were found that needed to be addressed with simpler geometries. A compromise between a simple double-element wing and a realistic double-element wing geometry was sought.

A simplified wing assembly was designed and built based on a 2009 Formula 1 wing, at a 50% scale. It was designed as a double-element wing, with a main element and two identical flaps, as seen in Figure 2-2 and Appendix B.1. The main element was an untwisted, unswept, untapered, GA(W)-1 section wing with a 750mm span and 119.7mm chord. The flaps consisted of two identical untwisted, unswept, untapered, Reynard Motorsport Kylie aerofoil sections with a 250mm span and 160.2mm chord. These aerofoil sections were developed by Reynard Motorsports for use as flap elements on inverted wings in ground effect for their Indycar projects in the late 1990s. A flap was placed towards each tip of the main element, and held in position by the endplate and a bracket (see Appendix B.1, Figure B-2). The correct overlap and gap for the flap was obtained from previous work by Young (2003). The endplates consisted of

10mm thick plates, 274mm long, 99.8mm high, with a 25mm radius between the top edge and the vertical leading edge, and the lowest edge 6 mm below the lowest point on the suction surface of the wing. The inner vertical leading edge of the endplate had a 10:5mm ellipse profile, the outer top and vertical leading edges had a 5mm radius, while the remaining edges were square (see Appendix B.1, Figure B-2).. The endplates were fastened to the tip of the main element giving the assembly a total span of 770mm.

The main element was designed to operate at a fixed angle of attack of -0.5° (leading edge up), while the flaps had two different angle settings: 13.8° and 23.9°. Due to changes in the total chord with varying flap angles, a fixed value of 252mm was used as the chord of the assembly. This value was calculated by averaging the chords of the two different flap settings, giving the assembly an aspect ratio (AR) of 3.82 and a planform area (A) of 0.161 m^2

The main element of the wing was machined from aluminium, whilst the flaps, due to their geometry, were made from two separate parts. The first part consisted of the leading edge profile, which was made from aluminium and the second part consisted of a steel plate which was bonded and screwed to the aerofoil section. Due to manufacturing reasons, each element had a finite thickness trailing edge. The wing had a 1.9 mm-thick trailing edge, representing 1.6 %c of the main element and the flaps had a 2.1 mm-thick trailing edge, representing 0.8 %c of the flap.

2.2.2 Wing Setup

The wing assembly was suspended on two pylons from a force balance, located at the bottom of the wind tunnel support sting (see Appendix B.2). The correct positioning of the wing was ensured by two reference pins on each side of the wing. Their location on the wing was known and measuring their height relative to the road and to a reference slot on the side of the road allowed for accurate setting of the wing's main element to within $\pm 1.667 \times 10^{-4}$ degrees, $\pm 4.0 \times 10^{-3}$ degrees and $\pm 2.1 \times 10^{-2}$ degrees in pitch, roll and yaw respectively.

In order to study the wing's aerodynamic performance when operating in roll and yaw, the model was designed to yaw to ±2.5° and ±5.0° and roll to ±1.5° and ±3.0°. For both experiments in roll and in yaw the force balance was positioned so that lift and drag were measured directly without needing to use a transformation matrix to extract the values, i.e., lift was measured in the vertical axis (z) and drag measured in the longitudinal axis (x).

The wing's ride height was defined by the distance from the ground to the lowest point on the suction surface of the wing's main element. When setting the wing in the wind tunnel the ride height was set by using a set of slip gauges between the wing endplates and the rolling road, as well as a height gauge to confirm the height from the top of the end plate to the rolling road. During the experiments the sting motion control system adjusted the ride height to the required positions.

The wing assembly was representative of a Formula 1 front wing assembly mounted on a car at 0° nominal pitch.

2.2.3 Wake-Generating Model

A short bluff body (Figure 2-3 and Appendix B.3) was built to represent a generic leading car at 50% scale. It was equipped with a rear wing, diffuser and non-rotating rear wheels in order to replicate the major flow features generated by a Formula 1 race car, as described by Wilson (2008). This gave the possibility of simulating a leading car without the requirement of having a complete car model in the wind tunnel, which would have further limited the test scale.

This body was placed upstream of the wing at a distance of 1165 mm from the leading edge of the wing, representing approximately half a car's length separation at 50% scale (see Appendix B.4). Due to space constraints in the wind tunnel test section, the body was placed ahead of the rolling road, on a fixed ground. The body was held in place by two angle brackets that were attached to a support beam inside the boundary layer suction box.

2.3 Research Techniques

2.3.1 Force Measurement

Forces were measured using an Aerotech 6-component force balance with the wind tunnel set to constant dynamic pressure mode. Force and other wind tunnel parameters were recorded at a logging frequency of 10Hz for 20 seconds at each ride height during the experiments. Nil-force data were also obtained prior to and after each run in order to eliminate force balance drift during the run.

The force balance was located inside a non-metric streamlined body. This streamlined body isolated the force balance from the airflow and also simulated the nose cone of a Formula 1 car. Special attention was taken in designing the body so that forces on the body would not be transmitted to the force balance, which would therefore only measure the wing and pylon forces.

2.3.2 Surface Flow Visualization

A mixture of fluorescent pigments, paraffin and a few drops of oleic acid (as an anti-coagulant) was used for the surface flow visualization tests. This mixture was sprayed evenly onto the surface of the wing using an aerosol spray. The wing was then set at the required ride height and the freestream velocity was set to the required value for 45 to 60 minutes to allow the mixture to dry, after which the pigments left on the wing surface highlighted the flow features. An ultraviolet light was used to make the particles glow, allowing for pictures to be taken with higher contrast than if a non-fluorescent pigment had been used.

2.3.3 Laser Doppler Anemometry

A Laser Doppler Anemometer (LDA) is a non-intrusive device that measures the instantaneous flow velocity at a point by using laser beams. Two laser beams intercept at a point forming a measurement volume and flow seeding particles scatter light when crossing the measurement volume. The scattered light is collected by a receiving optic and analysed by a spectral analyser that

calculates the speed and direction of the flow based on the Doppler shift of the scattered light and the orientation of the beams.

A two-component LDA system from Dantec was used in order to measure off-surface flow velocity. The system consists of a multi-line argon-ion laser, a transmitter box incorporating a Bragg cell, a two-component probe and two burst spectrum analyser (BSA) boxes. Although the system allowed for a third component to be measured a second lens of a matching focal length was not available. This meant that in order to obtain the third velocity component a second measurement of the same point at a different beam orientation would be required, but due to the equipment malfunctioning it was not possible to carry out this measurement.

The Bragg cell consists of an acoustic-optical modulator that splits the laser light into two new beams of the same intensity, but with a 40MHz frequency shift between them. The shifted beams are then separated into different wavelengths that correspond to green, blue and violet laser light. These are aligned and focused into optical fibres and transmitted through a lens. The lens emits 2 beam pairs which are then focused and overlapped at a point in the flow creating an ellipsoid-shaped measurement volume.

The interception of each pair of beams in the measurement volume creates interference fringes. As a seeding particle crosses the fringe pattern light is scattered. From the scattered light the speed and direction of travel of the particle can be calculated, along the beam pair axis, as the scattered light contains a Doppler shift which is proportional to the velocity. The scattered light is captured by the receiving optics at the back of the probe, transmitted through the optic fibres to the photomultipliers. These send the raw signal to the BSA boxes that analyse the signal and send the data to the Dantec BSA Flow software.

Using a 2.5m focal length lens measurements were taken at a selection of planes downstream of the models. A grid of points was defined in each plane and a total of 1.6×10^5 data samples were acquired for each grid point before the traverse moved to the next measurement point. Due to the size of the

measurement volumes (0.025mm x 15mm x 0.025mm) the resolution of the grid was limited by the measurement volume in the y-direction, hence a grid was defined, with a spacing of 25mm between each point, so that each measurement did not overlap another making each measurement point unique.

A Concept Smoke 135 smoke machine was used to seed the flow. This machine was found to produce high quality seeding at ambient temperature, with the average particle size being 0.7µm. The smoke generator was located outside of the wind tunnel and supplied the smoke through a hose into the working section collector. This meant that the smoke particles would flow around the circuit before reaching the test section, which allowed for a homogenous mixing of the smoke with the air flow.

Because the DS Houghton wind tunnel has an open test section the quantity of the seeding fluctuated during the experiments and consequently the sampling frequency also fluctuated. Due to the large size of the measurement planes and the differences in flow at different spatial locations it was decided to gather a greater number of samples than would normally be required. This was aimed at reducing the standard error and the influence of local flow instabilities on the average results. The selection of the sample size was based on information from previous studies carried out in the DS Hougton wind tunnel and by carrying out measurements of the wind tunnel's mean velocity using the LDA system and comparing with the data obtained from the wind tunnel's pitot-static tube. Analysis of the LDA measurement uncertainty (see Appendix 6.2C.2) indicated that for a 95% confidence interval the measurement error for the u velocity component was below 1%, as explained in Appendix C.2.3. In Appendix D.1.3 further information regarding the dimensions and positions of the measurement planes can be found.

2.3.4 Computational Study

Following the Fluent guidelines for external automotive aerodynamics testing, provided by Lanfrit (2005), a computational domain, as shown in Figure 2-4, measuring 3 times the wake-generating body length (L) upstream, 7L downstream of the rearmost point behind the trailing wing, and with a width of

5.30L and height of 3.53L that gave a blockage of 0.88%, was discretised into approximately $1.7x10^7$, $3.4x10^7$ and $5.0x10^7$ unstructured elements generated in IcemCFD for the wing in isolation, the wake-generating body in isolation and the wake-generating body with the wing immersed in its wake, respectively. These consisted of triangular surface elements, tetrahedral volume elements and prism boundary-layer elements. A $y^+ \leq 1$ and a total of 24 prism layers on the wing surface were used due to the chosen turbulence model requiring a near-wall modelling approach that fully resolved the boundary layer.

To prevent issues during solving special attention was paid to the quality of the mesh. An Octree algorithm was used to generate a surface mesh, a Delaunay algorithm to generate the volume mesh, and finally prism layers were grown one-by-one. Localised refinement and smoothing was used between each stage in problematic areas such as the tyre contact patch and slot gap between the two wing elements. Due to problems with the geometry of the contact patch a minor simplification was adopted by using a contact block instead of a tangent contact with the ground plane. A minimum quality criterion for mesh regularity was set to 0.4 and the target of zero highly skewed elements was achieved, improving the solution accuracy.

An incompressible, steady-state segregated solver was used in Ansys Fluent for all simulations. The 3-equation $k\text{-}k_L\text{-}\omega$ transitional RANS turbulence model was used. This model was chosen due to its good prediction of transition from laminar to turbulent flow. Although this was not important for the wake-generating body it was of significant importance for both the trailing wing in isolation and in the wake, in order to correlate computational surface results with surface flow visualization results.

A computational domain was generated to replicate correctly the wind-tunnel rolling road, with the boundary representing the ground split into two parts, the first part being the fixed ground and the other the moving ground. The fixed ground was set as a stationary boundary wall and the moving ground was set as a translating wall, at the same speed as the freestream velocity. Both walls had a no-slip condition applied in order to replicate the wind tunnel boundary

layer development. To model the three-quarter open test section configuration of the wind tunnel the remaining boundaries (domain walls) were defined with symmetry conditions. This enforced a zero normal gradient to the wall for all parameters. The inlet was defined as a velocity inlet, with the turbulence length scale set to 0.1m and the turbulence intensity to 0.8% at the inlet, giving a turbulence intensity, at the leading edge of the trailing wing, similar to that recorded in the wind tunnel (0.7%) and the outlet was defined as a pressure outlet.

The inlet conditions were used to initialize the flow-field, followed by a total of 7,500 iterations on Cranfield University's HPC cluster, Astral. The wing drag and lift coefficients were monitored throughout the simulations and were used as the convergence criteria. The simulations ran in batch mode and were deemed as converged once both parameters were steady to three significant figures for a minimum of one hundred iterations, a condition that was confirmed during post-processing at the end of the runs. In Figure 2-5 we find a typical illustration of the convergence history for the lift and drag coefficients over the last one thousand iterations of a simulation. The figure shows the values of normalized lift and drag are stable to within ±0.25% of their average value. A typical convergence history for the cell residuals can be found in Figure 2-6. In all cases the convergence criterion was obtained before five thousand iterations and did not require any further solution time once reaching 7,500 iterations.

2.4 Overall Procedure

The aim of this study was to improve the understanding of the influence of real on-track effects, such as roll, yaw and immersion in the wake of a leading car, on the performance of a simplified Formula 1-type wing in ground effect.

A key objective of this work was to understand the influence of a leading Formula 1 car's wake on the aerodynamic performance of a trailing wing. In order to do so the aerodynamic forces of the wing were measured in an undisturbed flow at various ride heights and wing settings to obtain the reference data (see Chapter 3). From the reference data a group of ground clearances and settings was selected to conduct the surface flow visualization

tests. During this phase the data required for the roll and yaw cases were also obtained.

In the following phase the wing's aerodynamic forces were measured with the wing positioned in the wake of the leading bluff body. These were measured at the same ground clearances and wing settings as in the undisturbed cases. These results are discussed in Chapter 5.

In order to prevent repeatability issues due to removing the wing assembly from the wind tunnel it was decided to carry out all force measurements on the wing in both the undisturbed and disturbed flow cases, before removing it for the wake survey. This way the final phase of the research consisted of measuring the wake of the bluff body and of the wing with the objective of understanding the bluff body's wake/wing interaction and the changes produced to the wing's wake. Due to equipment failure this phase was cut short and a numerical study was conducted, with the LDA data being used to validate it. Both the experimental and computational results are presented in Chapter 4.

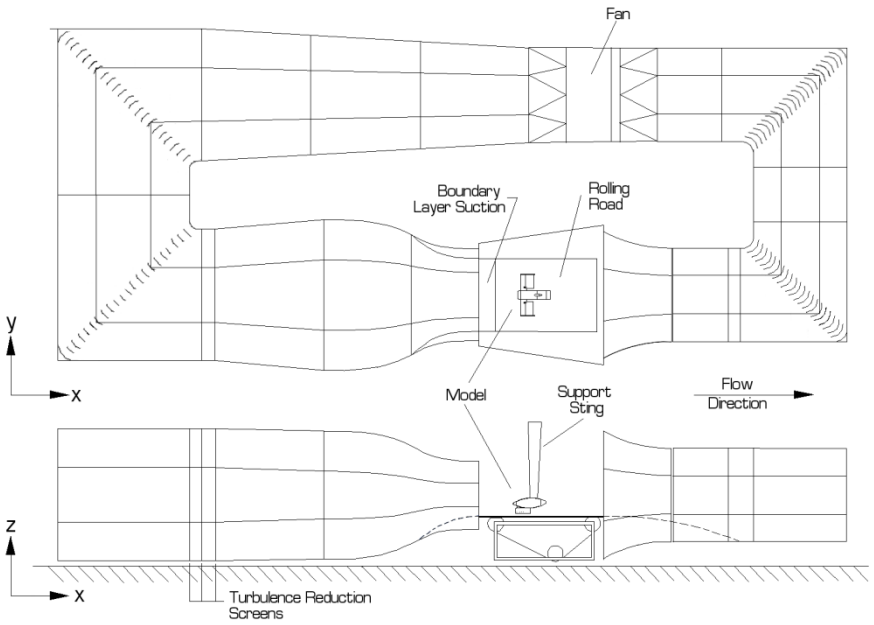

Figure 2-1: DS Houghton Wind Tunnel Schematic

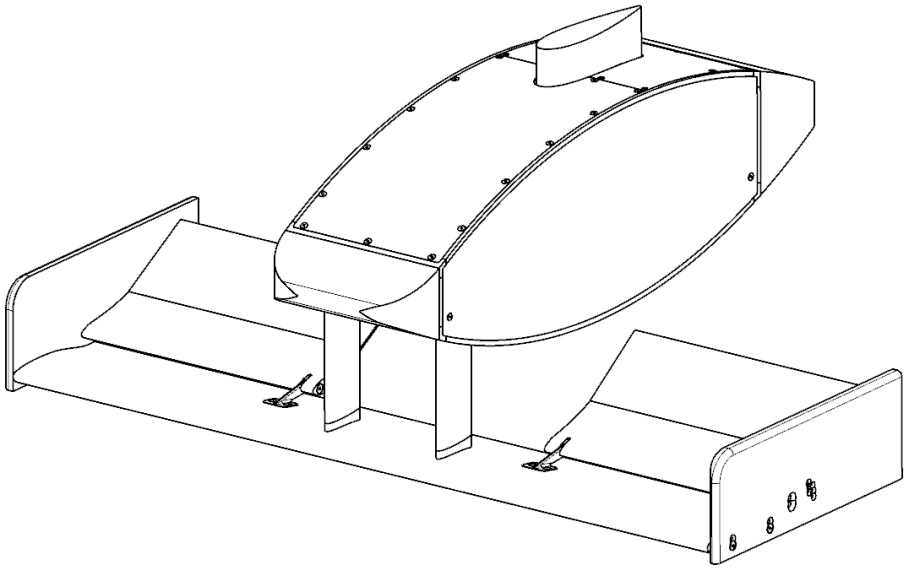

Figure 2-2: Simplified Wing Geometry

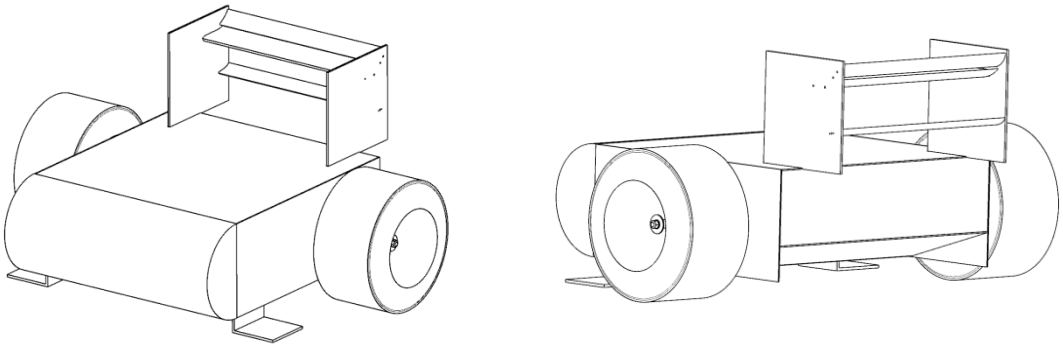

a) b)

Figure 2-3: Schematic of upstream body: a) front-quarter view; b) rear-quarter view

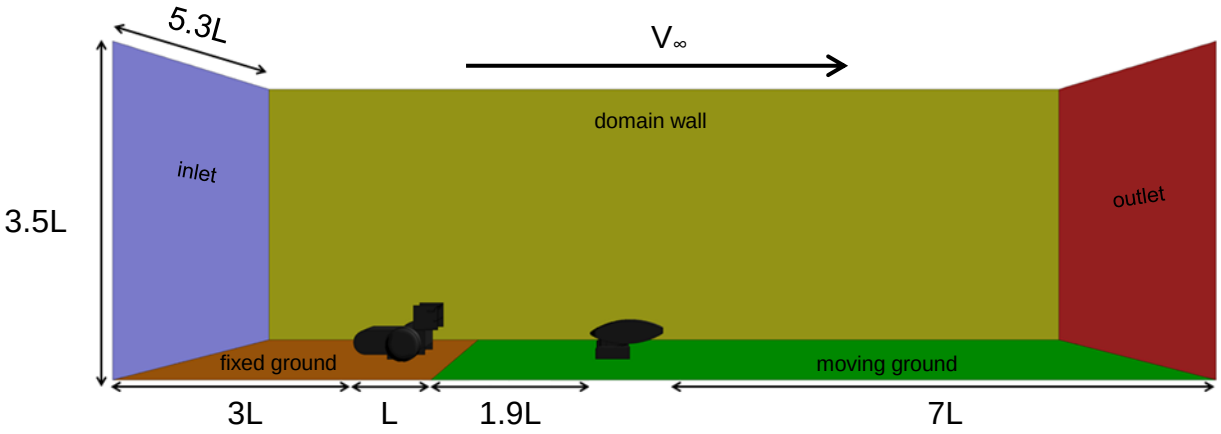

Figure 2-4: Schematic of the computational domain.

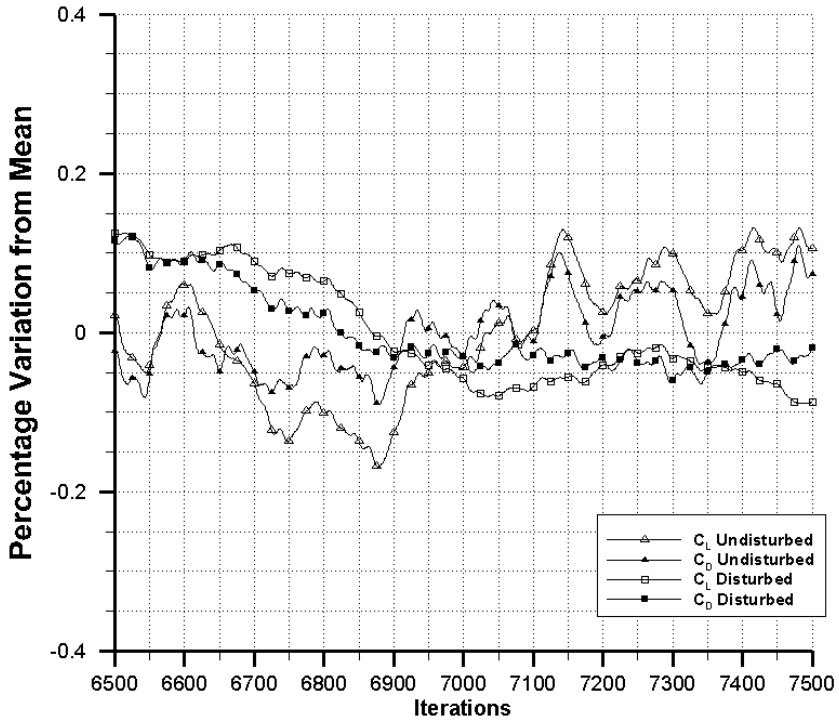

Figure 2-5: Convergence history, normalized lift and drag coefficient monitors, for both the wing in undisturbed and disturbed flow cases.

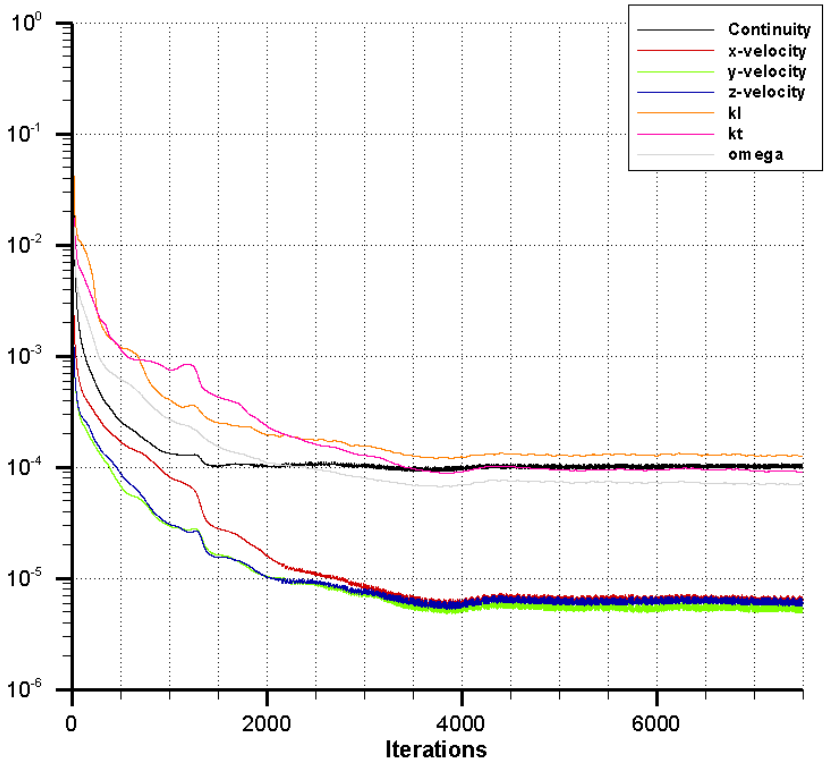

Figure 2-6: Convergence history, scaled monitors

3 Wing Operating in Undisturbed Flow

3.1 Introduction

In this chapter the results for the wing operating in undisturbed flow will be presented and discussed. Force measurements, surface flow visualization and computational simulations will be used to understand the performance characteristics of the wing operating at different yaw and roll angles.

Two flap setting of 13.8º and 23.9º, that will be regarded as low and high setting respectively, were tested at three different yaw angles (0°, 2.5°, and 5.0°) at 0° of roll and subsequently tested at three different roll angles (0°, 1.5° and 3.0°) at 0° of yaw. Further tests were carried out to verify if the results were independent of yaw and roll direction and to confirm that the wing did not suffer from hysteresis due to ride height changes. The results, shown in Appendix C, indicated that neither hysteresis nor dependency of yaw or roll direction were present in the model used in this study.

Computational simulations were carried out in order to obtain data that could not be obtained experimentally, due to equipment malfunctioning. The simulations were done at a selection of ride heights at which surface flow visualization had been done, in order to correlate the experimental and computational flow patterns and force results. Lists of the tested configurations, and comparison between experimental and numerical results can be found in Appendix D.

3.2 Wing Operating at Zero Yaw and Zero Roll

3.2.1 Force Measurements

As shown in Chapter 1, there has been a significant amount of research on inverted wings in ground effect in the last two decades. These studies have allowed a rapid increase in the understanding of how an inverted wing's performance changes in proximity to the ground and have led to the introduction of concepts that describe, in a simplistic way, some of the phenomena associated with inverted wings in ground effect. A concept such as the force-

enhancement region that describes the range of ride heights where the downforce generated by the wing increases as the ride height is decreased was introduced by Zerihan and Zhang (2000b). They also introduced the concept of the force-reduction region that, conversely, consists of the range of ride heights where downforce decreases as ride height is decreased.

Further studies by Zhang and Zerihan (2002) and Mahon (2005) further developed the force-enhancement/reduction concept and divided the two regions into smaller sub-regions that are identified by changes in the downforce coefficient slope as the ride height is reduced. With the changes in the slope, as ride height is reduced, four main regions are identified (see Figs Figure 3-1 to Figure 3-5).

- Region A – characterized by the increase of downforce due to the acceleration of the flow between the wing and the ground and the increase of tip-vortex suction
- Region B – where tip vortices become unstable and begin bursting, at the lowest ride height in the region, leading to a reduction in the rate of downforce increase due to the loss of wing-tip vortex suction.
- Region C – where downforce is increased due to the acceleration of the flow between the wing and the ground as the ride height is decreased. In this region the downforce enhancement occurs without the aid of tip vortex suction.
- Region D – where the boundary layer separates from the wing's suction surface leading to a decrease in downforce.

3.2.1.1 High Flap Angle

The downforce coefficient (C_L), downforce coefficient slope ($dC_L/d(h/c)$), drag coefficient (C_D) and downforce-to-drag ratio (L/D) results at different ride heights are presented in Figure 3-1, Figure 3-2, Figure 3-3 and Figure 3-4 respectively.

The variation of downforce coefficient with ride height (h/c) is shown in Figure 3-1. As the wing is lowered from its maximum ride height of h/c=0.893 the downforce coefficient increases monotonically until reaching the ride height of

h/c=0.159, at which point the downforce coefficient has reached C_L=1.934 from an initial value of C_L=1.185 at h/c=0.893. Below h/c=0.159 the downforce coefficient continues increasing with further reductions of ride height but at a slower rate than before. The maximum downforce is reached at a ride height of h/c=0.079 with C_L=2.098, a value 77% greater than recorded at h/c=0.893. Below this ride height the downforce coefficient decreases with further ride heights reductions, reaching a downforce coefficient of C_L=2.053 at the lowest ride height tested in this study (h/c=0.060). Also shown in Figure 3-1 are the results from Zhang & Zerihan (2002). Despite the differences between the present work and their work, which are caused by different wings being used in both studies, the trends seen in both works are similar. As with the present work, Zhang & Zerihan's results also show downforce increasing as the wing's ride height is reduced, reaching a downforce peak and then downforce decreasing with further reductions in ride height. Changes in the downforce slope are also seen at similar (but not identical) ride heights.

In Figure 3-2 the results for the downforce coefficient slope at different ride heights are presented. The analysis of the downforce coefficient slope results is of interest as local maximum and minimum values indicate the boundaries of different regions with different flow mechanisms that cause changes in the downforce coefficient plot. Analysis of the plot shows that between the starting ride height of h/c=0.893 and h/c=0.159 as the wing's ride height is reduced the slope increases from 0.218 until reaching a maximum of 4.147, Region A. Below h/c=0.159 the wing enters Region B with the slope decreasing with further reductions of ride height reaching a value of 1.392 at h/c=0.129. As the ride height continues to reduce the wing enters Region C, where the slope increases as the ride height is reduced and a local maximum of 2.237 is reached at h/c=0.109. Below h/c=0.109 the wing enters the final region (Region D) where the downforce slope decreases with further reductions in ride height, reaching a minimum value of -3.556 at h/c=0.060, the lowest ride height analysed in this study.

The variation of drag coefficient with ride height is presented in Figure 3-3. For the high flap angle, as the wing's ride height is reduced from the maximum ride height of 0.893c the drag coefficient increases monotonically until reaching h/c= 0.159 at which point the drag coefficient has increased from C_D =0.144 to 0.220. Between the ride heights of h/c=0.159 and h/c=0.129 the rate of drag coefficient enhancement decreases reaching zero once it reaches a ride height of h/c=0.119 with a drag coefficient of C_D=0.232. Below this height the drag coefficient remains unchanged until reaching a ride height of h/c=0.079. Below h/c=0.079 the drag coefficient decreases slightly and reaches a value of C_D=0.231 at h/c=0.069, this is followed by an increase to its maximum value to C_D=0.233 at a ride heights of h/c=0.060, the lowest ride height studied in this work. As a comparison, also shown in Figure 3-3 are the results from Zhang and Zerihan (2002), which also show the wing's drag coefficient increasing monotonically as the wing's ride height was decreased.

The downforce-to-drag ratio (L/D) results at different ride heights are presented in Figure 3-4. As the wing's ride height is reduced from the maximum ride height of h/c=0.893 L/D increases monotonically from a value of 8.226 to 8.806 at a ride height of h/c=0.159. Between a ride of h/c=0.159 and h/c=0.129 L/D decreases reaching a minimum value of 8.720. Below h/c=0.129 L/D increases once again with further reductions of ride height reaching the wing's maximum L/D at a ride height of h/c=0.079 with a value of 9.053. Below this ride height L/D decreases with further reductions in ride height, reaching a value of 8.803 at the ride height of h/c=0.060. Analysis of the L/D results shows that the different regions described previously do not have a direct relation with the inflection points seen in the L/D results. Also presented in Figure 3-4 are the L/D results from Zhang & Zerihan (2002). These present a similar trend to that seen on the high-flap-setting wing but with greater variations of L/D over the ride-height range. This gives their wing a steeper L/D slope, whilst the wing used in this present study has a flatter L/D variation with ride height, giving the wing a similar efficiency throughout its operating range.

3.2.1.2 Low Flap Angle

The results for the variation of downforce coefficient with ride height are presented in Figure 3-1. As the wing is lowered from its maximum ride height of h/c=0.893 the downforce coefficient increases monotonically until reaching a ride height of h/c=0.119, at which point the downforce coefficient has increased from C_L=0.726 to C_L=1.352. Below h/c=0.119 the downforce coefficient continues increasing, with some minor oscillations, as ride height is reduced. The maximum downforce coefficient is reached at a ride height of h/c=0.069 with a value of C_L=1.538, which is 112% greater than that recorded at h/c=0.893. Below this ride height the downforce coefficient decreases with further reductions of ride height reaching C_L=1.528 at the lowest ride height measured in this study (h/c=0.060).

In Figure 3-5 the results for the downforce coefficient slope at different ride heights are shown. From the starting ride height of h/c=0.893 and as ride height is reduced the slope increases, with a minor fluctuation between h/c=0.298 and h/c=0.238, until reaching a maximum of 5.562 at h/c=0.119, a range identified as Region A. Between h/c=0.119 and h/c=0.099 (Region B) the slope decreases and reaches a minimum of 2.669. Below h/c=0.099 the wing enters Region C where the downforce slope increases with the reducing ride height until reaching h/c=0.079 where a local maximum of 4.648 is observed. Entering Region D, below h/c=0.079, the downforce slope decreases continuously with further ride height reductions, reaching a minimum value of -1.037 at h/c=0.060, the lowest ride height analysed in this study.

The results for the variation of drag coefficient with ride height are presented in Figure 3-3. As the ride height is decreased the drag coefficient increases without any significant changes to its trend, with the exception of minor fluctuations between the ride heights of h/c=0.129 and 0.089. The drag coefficient increases from C_D=0.057 at ride height of h/c=0.893 to C_D=0.135 at a ride height of h/c=0.060 representing an increase of 137%. The results also show that unlike the high-flap-angle case the low-flap-angle case does not see a plateau in the drag coefficient value.

In Figure 3-4 the results for the variation of downforce-to-drag ratio (L/D) with ride height for the low flap angle setting are presented. Similarly to the high flap setting the low flap setting has an almost flat variation with ride height, but contrary to the high flap setting, there is a very small decrease in L/D as ride height is reduced, with L/D dropping from 12.851 to 12.476 between the ride heights of h/c=0.893 and h/c=0.188. With further reductions of ride height, below h/c=0.188, L/D increases reaching a value of 12.745 at a ride height of h/c=0.109. Below this ride height L/D decreases once again with further reductions of ride height reaching a value of 11.294 at a ride height of h/c=0.060, the lowest ride height analysed in this study.

3.2.2 Surface Flow

Surface flow visualisation was carried out at different ride heights, capturing the force enhancement and reduction regions on both the high and low flap settings. Due to the similarities in results, between both cases, only the high flap setting results are presented.

In Figure 3-6 the streaklines on the wing's suction surface for the high flap setting are presented for ride heights of h/c=0.179, h/c=0.089 and h/c=0.069. The figures show the presence of a spanwise bubble type region on the wing's main element, with the exception of a small region in proximity to the wing tip, at the different ride heights. This bubble structure is caused by the laminar boundary layer separating from the wing surface, due to the adverse pressure gradient, and reattaching downstream once the boundary layer transitions to turbulent.

The wing tip vortices can be identified by the triangular shape on the wing's surface starting at the leading edge of the wing next to the endplate, as indicated in Figure 3-7. As the wing's ride height is reduced the tip vortices appear to widen, an indication of the instabilities in the vortex structures as described by Zhang et al. (2002). In proximity to the wing tips the tip vortex interacts with the bubble structure altering its shape.

Downstream of the bubble the flow becomes random without the separation between the streaklines that are seen upstream of the bubble. This characteristic highlights the presence of a turbulent flow downstream of the bubble. As the ride height is reduced the flow at the trailing edge at the mid-span of the wing (left-hand edge of the figure) appears to become more unstable and signs of flow reversal are present at a ride height of h/c=0.060 indicating the presence of a separated boundary layer. In Figure 3-6(b) some flow reversal is also visible at the trailing edge of the main element, which is caused by a hole on the wing's surface not being properly plugged leading to a local flow separation.

Presented in Table 3-1 are the results for the bubble separation onset and flow reattachment chordwise locations, and bubble length for both the high and low flap angle cases. Analysis of the bubble shape, for the high flap setting, indicates that its geometry is influenced by the ride height. At the ride height of 0.179c the bubble appears to have a curved shape pointing in the upstream direction and its length varies along the span, with its minimum length at mid-span of the main wing element and the maximum length seen in the same spanwise position as the flap mid-span. The onset and length of the bubble are also affected by the reduction in ride height, with the onset at 35.5%c for a ride height of h/c=0.179 and 30.4%c for a ride height of h/c=0.060, while the bubble's length decreases from 10.8%c to 7.6%c, at ride heights of h/c= 0.179 and h/c=0.060 respectively.

On the flap's suction surface the flow appears to remain relatively unchanged throughout the ride height range presented. At all ride heights the mid-span flow appears to be parallel with the freestream direction. Inboard of the flaps the flow turns towards the inner tip due to the presence of a wing-tip vortex on the inner edge of the flap. The flow on the flap's suction surface does not appear to be influenced by the ride height reductions, with the exception of a small triangular region on the outboard tip that appears to increase in size at the lower ride heights.

3.2.3 Computational Results

3.2.3.1 Validation

Due to the limitation in the experimental programme computational simulations were run to understand the significant flow features around the wing in undisturbed freestream flow, in order to compare with the results in the wake of the leading body, which will be discussed in Chapter 5. In order to confirm if the selected computational approach was reliable the computational results for the high-flap-setting wing operating in the undisturbed flow were compared with the force measurements and the surface flow visualization results obtained in the wind tunnel.

The comparison between the experimental and computational downforce coefficient results can be found in Figure 3-8. The computational simulations were carried out at the ride heights for which surface flow visualization was available and show a slight under-prediction of the downforce being generated by the wing at the five ride heights simulated. At the greatest ride height simulated (h/c=0.893) the simulations under-predicted the downforce value by 0.1%, which was considered a very good agreement with the wind tunnel results. Simulations at lower ride heights led to the downforce coefficient's under-prediction increasing and reaching a maximum value of 2.73% for the lowest ride height at which the wing was tested in the wind tunnel (h/c=0.060).

The computational drag coefficient (Figure 3-9) results showed that this parameter was over-predicted in the simulations. At the greatest ride height in this study (h/c=0.893) the drag coefficient was over-predicted by 2.54%, when compared to the experimental results. As the ride height of the wing was reduced the over-prediction in drag coefficient increased and reached its maximum value of 5.98% at the lowest ride height (h/c=0.060). The larger error in predicted drag, compared to that for downforce, was to be expected as computational codes have difficulty in predicting accurately pressure fields in separated and vortical flow. Also due to the small magnitude of the drag coefficient, in the experimental data, the small variations in the computational

results gave a greater percentage variation than in the case of the downforce coefficient.

In Figure 3-10 a comparison between the CFD-predicted surface streamlines and the surface flow visualization, obtained in the wind tunnel, is presented for ride heights of h/c=0.179, h/c=0.089 and h/c=0.069. The results showed that in all cases the simulations predicted accurately the onset of the separation bubble. In the case of h/c=0.179 (Figure 3-10a) the computation results indicated that the boundary layer reattachment (Region A) occurred further downstream at mid-span than was seen in the wind tunnel. Despite this at mid-flap span the computational results accurately predicted the chordwise location of boundary-layer reattachment (Region B). For the case at h/c=0.089 (Figure 3-10b) the simulations were able to capture accurately the separation bubble throughout the wing span and also predict a region of separation at the trailing edge of the main wing element. For h/c=0.060 (Figure 3-10c) the separated boundary layer along the main wing element was captured correctly. In all cases the simulations predicted for the flap the presence of a separation bubble, which was not present in the wind tunnel (Region C), a situation that may be caused by the surface roughness not being modelled accurately in the computational approach. Towards the tip of the wing the region of the tip vortex is captured accurately with the shape of the interference region between the separation bubble and the tip vortex matching (Region D) and the aforementioned triangular shape at the tip of the wing, where the tip vortices live (Region E), widening at lower ride heights as seen in the wind tunnel results. In both the h/c=0.179 and h/c=0.089 cases the simulations predicted a greater region of separation (Region F) at the main element's mid span, a situation that may be caused by an incorrect setting of the turbulence dissipation rate.

Despite the differences between the experimental and computational forces and surface flows the trends seen in the computational results match those seen in the experimental data. This gives confidence that the CFD can be used, with caution, to fill in the gaps in the experiments.

3.2.3.2 Chordwise Pressure

The chordwise pressure distribution variation with ride height at mid-span, at mid-flap span and at wing tip is shown in Figure 3-11, Figure 3-12 and Figure 3-13 respectively.

The results for mid-span (Figure 3-11) show that as the wing's ride height is reduced the pressure distribution at the leading edge of the wing's suction surface changes shape and peak suction moves aft. At the greatest ride height of h/c=0.179 the pressure decreases quickly for x/c<0.03, reaching its peak negative value, followed by a small rise in pressure before a more gradual increase until x/c≈0.35. After this point the pressure increases at a greater rate until reaching the trailing edge of the wing. For both h/c=0.060 and h/c=0.089 the pressure decrease is more progressive and the pressure peak is reached further along the wing section. In both cases the suction peak is reached at x/c≈0.22 followed by a gradual increase in pressure until a point (x/c≈0.30) where the rate of pressure raise increases. The results also show a change in the pressure distribution on the pressure surface with the pressure on this surface decreasing slightly with ride height reductions.

The results for the pressure distribution around the main plane and flap (Figure 3-12) at the mid-flap plane show a similar trend to the previous case. As the wing's ride height is reduced the pressure along both the pressure and suction surfaces of the wing decreases. Similarly, the pressure decrease at the leading edge has the same shape as in the mainplane mid-span case. The shape of the pressure plot on the suction surface of the wing is similar to the previous case for h/c=0.060 and h/c=0.089, whilst for h/c=0.179 the initial peak at x/c≈0.03 and subsequent drop are followed by a gradual increase in pressure until a second suction peak is reached at x/c≈0.27. Behind this point the pressure gradually increases until reaching x/c≈0.37, where the pressure starts increasing at a greater rate. The flap pressure distribution shows that the pressure on the suction surface is not as affected as on the main element's suction surface with ride-height reductions, at this spanwise location. On the suction surface the initial pressure decrease, in the main plane/flap overlap, is

identical for each ride height. Downstream of the main element's trailing edge the pressure distributions indicate that the case at h/c=0.060 has a slightly higher pressure than that of the other two cases, which show similar results.

The chordwise pressure distribution results at the wing tip (Figure 3-13) show similar results to the two previous cases. As before, the initial pressure decrease shows distinct shapes for each case. At the greatest ride height (h/c=0.179), after the initial drop the pressure gradually increases until reaching a local maximum at x/c≈0.17, after which point the pressure decreases until reaching a second peak at x/c≈0.35 before plateauing after this until the trailing-edge of the main plane. For both h/c=0.060 and h/c=0.089, after a gradual decrease in pressure that peaks at x/c≈0.37 the pressure increases at a greater rate than noted at the mid-flap section. Once again, similarly to the mid-span distribution, the pressure distribution for the h/c=0.060 shows a greater pressure than that of the other two cases, that now show differences in their flap pressure distribution.

From the results in Figure 3-11, Figure 3-12 and Figure 3-13 it is possible to obtain a comparison of the load that each wing section has at each ride height. This is presented in Figure 3-14 as a bar graph. In order to aid the visualization of the results they have been normalized using the loading seen at flap mid-span at a ride height of h/c=0.060, as this was the highest load seen in the data set. This way the remaining sectional loadings are presented as a percentage of this maximum loading. The results show that at a ride height of h/c=0.179 the three spanwise sections have a loading of 24.6%, 81.9% and 49.1% of the wing's maximum sectional loading. As the wing is lowered from a h/c=0.179 to h/c=0.089 the loading of the three sections increases by 6.2% at the wing mid-span, 15.7% at the flap mid-span and 4.2% at the wing tip, leaving each section with 30.8%, 97.6% and 53.3% of the wing's maximum sectional loading. With a further reduction of ride height, from h/c=0.089 to h/c=0.060, the section loading increases by 3.3% at the wing mid-span, reaching a loading of 34.1% of the maximum value, while the flap mid-span loading increases 2.4% reaching the maximum sectional loading. Contrary to the other spanwise sections the wing

tip suffered a reduction in loading of 5.7% with the final ride height reduction, giving it a final loading 47.8% of the maximum sectional loading seen by the wing, an indication of the reduction in vortex-induced suction due to the tip vortices bursting.

Comparing the sectional loading results with the surface flow visualisation it is possible to identify some trends.

- The reduction in mid-span loading increase as the wing's ride height is reduced is consistent with the increase of the boundary layer separation seen on the wing's mainplane.
- The reduction in wing-tip loading is consistent with the widening of the triangular region at the tip of the wing, where the tip vortex lives, which is attributed to the tip vortex bursting and consequently leading to a decrease in vortex-induced suction.
- The absence of a separated region at the trailing edge of the flap is consistent with the gradual increase in mid-flap loading, as the ride height is reduced. Despite this the reduction in loading increase between the ride heights of h/c=0.089 and h/c=0.060 is an indication that the flap is getting close to a condition where the boundary layer will start separating.

3.2.3.3 Wake Flow Field

Figure 3-15 and Figure 3-16 present the flow vectors and dynamic pressure at x/c=1 behind the wing for ride heights of h/c=0.060 and 0.089 respectively. The results show the presence of a pair of counter-rotating vortices on each tip of the flap, an outer-tip vortex and an inner-tip vortex. The outer-tip vortex appears to be very weak, which is expected as at these ride heights the outer-tip vortices are expected to have burst from the downforce coefficient slope analysis. Analysis of the normalized vorticity plots in Figure 3-17 and Figure 3-18 confirm the absence of a strong outer-tip vortex at both ride heights. On the other hand the inner-tip vortex is much stronger and its position does not change as the ride height is reduced.

In Figure 3-19 and Figure 3-20 the velocity vectors and turbulence intensity contours at x/c=1 behind the wing are presented. These results show a significant change of the turbulence intensity in the region of the outer vortex, increasing from 20% to 30% with the ride height reduction. This increase of turbulence intensity in the region of the outer-tip vortex can be attributed to the instabilities caused by the bursting of the outer-tip vortex. Although the vorticity contours (Figure 3-17 and Figure 3-18) indicate that the vorticity of the inner-vortex does not change the increase in turbulence intensity to 10% from 5% may be an indication of instabilities in the vortex structure.

3.2.4 Discussion

The force measurement results obtained in the undisturbed flow for the wing at zero degrees of yaw and roll showed the presence of a downforce enhancement and force reduction region, as well as the continuous increase in drag with ride height reductions. These results gave reasonable agreement with the findings described in other studies of inverted wings in ground effect, despite differences in the results caused by different wing geometries.

Analysis of the downforce slope highlighted the presence of different regions that were postulated by Zerihan and Zhang (2000b) and further refined by Mahon (2005). The results showed that on the low-flap configuration the end of region A occurs at a lower ride height (h/c=0.119) than on the high-flap configuration (h/c=0.159), which is caused by differences in the force enhancement mechanisms in each wing configuration. The drag results showed that both wings performed in distinct manners. The high-flap configuration increased its drag until reaching a plateau, whilst on the low-flap configuration the drag increased monotonically, throughout the ride height range, without entering the plateau region. On the high-flap configuration as the ride height is reduced the downforce is increased and as a consequence the tip vortices become stronger, leading to an increase in induced drag proportional to the square of downforce. As the vortices start to break down the induced drag decreases, at the same time there is an increase of drag due to viscous effects in the boundary layer that lead to the separation of the boundary layer. In the

high-flap configuration the balance between both drag enhancement and reduction mechanisms lead to the plateau region. In the case of the low-flap configuration the significantly lower amount of downforce generated, when compared to the high-flap configuration, means that the wing tip vortices are significantly weaker, induced drag is lower and that viscous effects have a greater impact on the total drag than in the high-flap configuration. This consequent reduction in induced drag due to the lower downforce also has the implication of giving the low-flap configuration a higher L/D, as this form of drag increases with the square of downforce.

Surface flow visualization indicated the presence of a separation bubble, caused by a laminar separation with turbulent reattachment. Analysis of the separation onset and bubble length indicated that these parameters changed with ride height. Although it was not possible to measure during the present study a look at the literature available indicated that the height of the bubble would also be expected to change depending on the local flow speed and length of the bubble (Diwan & Ramesh (2007)). The existence of this bubble is important as it will alter the flow around the wing, effectively altering the local camber, leading to a change in the forces recorded.

The pressure plots were used to map the differences in pressure distribution around certain sections of the wing to serve as a reference in order to compare with the results on the wing in the disturbed flow in Chapter 5. As expected, the pressure distribution on the suction surface of the wing is dependent on ride height, which leads to changes in the pressure coefficient plot at different ride heights and at different spanwise locations. The changes noted in the pressure coefficient plots as the wing's ride height is reduced are a consequence of the increase in circulation, as a result of the flow accelerating between the wing and the road, and this leads to a change in the curvature of the oncoming flow. Consequently the stagnation point position, pressure distribution on both suction and pressure surfaces, and position of the pressure peak on the suction surface all change. Using the pressure plots it was possible to compare the

changes in sectional loading along the wing's span as the ride height is reduced and find a link with the surface flow visualisation results.

3.3 Wing Operating in yaw

3.3.1 Force Measurements

The results for downforce coefficient (C_L), downforce coefficient slope ($dC_L/d(h/c)$), drag coefficient (C_D) and lift-to-drag ratio (L/D) at different yaw angles and ride heights are presented in Figure 3-21, Figure 3-22, Figure 3-23 and Figure 3-24 respectively.

The downforce coefficient variation with ride height is presented in Figure 3-21. As the wings are lowered from a ride height of 0.893c the downforce coefficient increases monotonically until reaching the ride height of h/c=0.169, for both the 2.5° and 5.0° yaw cases. Although the plots for both cases have a similar trend each of them has a small difference in the rate of downforce enhancement, with the 5.0° case producing 2.5% less downforce than for 0° yaw at h/c=0.169, while 2.5° yaw produces only 1% less downforce at this ride height. As the ride height is further reduced below h/c=0.169 both 2.5° and 5.0° yaw suffer a reduction in their rate of downforce enhancement. While 5.0° appears to carry on with an almost linear increase of downforce between h/c=0.169 and h/c=0.089, 2.5° continues increasing its downforce coefficient at a variable rate, which is similar to the results obtained at 0° yaw. Both 2.5° and 5.0° yaw reach their maximum downforce coefficient at a ride height of h/c=0.079, the same ride height as at 0° yaw, with 5.0° reaching a downforce coefficient of C_L=2.030, which is 3.2% lower than the result obtained at 0°, and 2.5° reaching C_L=2.064, which is 1.4% lower than at 0°. Below the ride height of h/c=0.079 both 2.5° and 5.0° enter the force reduction region and their downforce coefficients decrease, reaching their minimum values of C_L=2.017 (3.5% lower than 0°) and C_L=1.981 (1.1% lower than 0°), respectively, at a ride height of h/c=0.060.

In Figure 3-22 the results for the downforce coefficient slope at different ride heights are presented for the 0°, 2.5° and 5.0° yaw cases. Both 2.5° and 5.0° present similar results to 0° and display the 4 regions previously identified for

the 0° case. As the wings are lowered from h/c=0.893 both yawed cases monotonically increase until reaching their maximum value of 3.943 for 2.5° at h/c=0.169, and 3.614 for 5.0° at h/c=0.159. These ride heights of maximum downforce slope indicate the lower boundary of Region A. As ride height is further reduced both cases enter Region B, with 2.5° reaching the lower boundary of the region at h/c=0.109 with a value of 1.041, while 5.0° reaches it at a higher ride height of h/c=0.149 with a value of 2.408. With further reductions in ride height both cases enter Region C with 2.5° reaching the lower boundary of the region at h/c=0.089 with a value of 2.056, and 5.0° reaching it at h/c=0.099 with a value of 1.960. Below these ride heights both cases enter Region D, where the slope continuously decreases with further reductions in ride height.

The drag coefficient variation with ride height is presented in Figure 3-23. Similarly to the downforce results yaw does not appear to have a significant influence on the drag coefficient at a ride height of h/c=0.893, with 0°, 2.5° and 5.0° yaw having a drag coefficient of C_D=0.144, C_D=0.145 and C_D=0.143, respectively, at h/c=0.893. As the ride height is reduced the drag coefficient increases monotonically with similar results for all configurations until reaching a ride height of h/c=0.169. As the ride height is further reduced from h/c=0.169 the drag coefficient continues increasing in the 5.0° case, although at a slightly lower rate, until reaching a local maximum value of C_D=0.226 at a ride height of h/c=0.099, a value 2.6% higher than at 0° yaw. With further ride height reductions the drag coefficient decreases until reaching a ride height of h/c=0.069, below which the drag coefficient increases to its maximum value of C_D=0.228 at h/c=0.060. At 2.5° yaw the drag coefficient presents similar results (Δ<1.2%) to 0° for hide heights above h/c=0.109. As the wing's ride height is further reduced, from h/c=0.109, the drag coefficient decreases slightly from C_D=0.231 to C_D=0.230 at a ride height of h/c=0.089, followed by a small increase reaching a drag coefficient of C_D=0.231 at h/c=0.060.

In Figure 3-24 the results for the downforce-to-drag ratio (L/D) variation with ride height are presented. The results show that despite a maximum difference of

L/D =0.100 (ε≤1.2%) between cases, a value below the absolute uncertainty for this plot, the trends seen for 2.5° and 5.0° of yaw are identical to those seen for 0° of yaw. This indicates that the efficiency is not affected for conditions where yaw is below 5.0°.

3.3.2 Surface Flow Visualization

In Figure 3-25 the streaklines on the suction surface of the wing are presented at a yaw angle of 5.0^0 for the high flap angle, for h/c=0.179, h/c=0.089 and h/c=0.060.

Similarly to 0° yaw a spanwise bubble region is noted on the surface of the wing. In proximity to the wing tips the tip vortex interacts with the bubble altering its shape. The wing tip vortices can be identified by the triangular shapes on either side of the wing that start at the leading edge of the wing next to the endplate and have a triangular shape as they grow downstream. As noted in the 0° case as the wing's ride height is reduced the tip vortices appear to widen, an indication that they are becoming unstable (Zhang & Zerihan (2004)).

Downstream of the bubble region the flow appears to be random with the defined streaklines present upstream of the bubble no longer present. This characteristic highlights the presence of a turbulent flow. As the ride height is reduced the flow at the trailing edge at the mid-span of the main element (centre of figure) appears to become unstable with signs of flow reversal present at h/c=0.060 indicating the presence of a separated boundary layer. Some flow reversal is noted at the trailing edge of the main element for h/c=0.089 (Figure 3-25b) but this is caused by a vortical flow generated by a hole on the wing's surface not being properly filled.

As with the 0° case the shape of the bubble appears to be influenced by the ride height. At a ride height of 0.179c the bubble's appears to have a curved shape pointing in the upstream direction and the bubble length varies along the span, with its minimum length at mid-span of the wing assembly and the maximum length seen in the same spanwise position as the flap mid-span. The onset and length of the bubble are also affected by the reduction in ride height, with the

onset at 29.5%c for a ride height of 0.179c and 27.5%c for a ride height of 0.060c, and its length changing from 9.1%c to 7.3%c respectively.

On the flap's suction surface the flow appears to remain relatively unchanged at the different ride heights. At all ride heights the mid-span flow appears to be parallel with the freestream direction. From the mid-flap and towards the inner tip the flow is turned towards the tip, a clear indication of the presence of a tip vortex. On the windward tip of the flap triangular flow pattern appears at a ride height of h/c=0.089 (as indicated in Figure 3-25) and increases in size at a ride height of h/c=0.060. This region of separation is caused by the flow rolling-up along the edge of the endplate, generating a vortex, due to the presence of a greater stagnation pressure on the endplate side caused by the movement of the leading-edge stagnant region to the side of the endplate as yaw was increased. As the wing's ride height is reduced the vortex becomes unstable leading to the appearance of the region of separation which grows in size once the vortex bursts at lower ride heights.

3.3.3 Discussion

Similarly to the results presented by Gogel (2007) the downforce generated by a wing in yaw decreases as the yaw angle is increased. The results showed that although at greater ride heights and at small yaw angles the differences in downforce and drag coefficients may be negligible, once in proximity to the ground (h/c<0.337) the differences in between the 0° yaw case and the other cases are above 1% and gradually increase as ride height is reduced.

Although lower downforce coefficient values were obtained with the wing in yaw, the results indicated that the force enhancement and reduction regions, and the mechanisms behind these regions are unchanged, something that was confirmed with the downforce slope results. These showed that the same downforce slope regions are present in all yaw cases and their boundaries do not change much as yaw is increased. This is further coroborated with the downforce-to-drag ratio where the results for the cases in yaw are virtually identical to the 0° case.

The surface flow results also further highlighted the similarities between the unyawed and yawed cases. Although slight differences are present the majority of the flow on the wing's suction surface is unchanged, with the exception of a separation region on the windward wing tip. This separation region is believed to be caused by the movement of the leading edge stagnation region to the side of the endplate, with the increasing yaw, and the roll-up of a vortex on the lower edge of the endplate that leads to the vortex region identified on the flap surface. Due to the elliptic shape of the endplate's leading edge the boundary layer did not separate, minimizing the performance losses in this study. By contrast, Gogel (2007) measured larger losses in yaw, attributed to separation off the windward endplate, which had a square leading edge.

3.4 Wing Operating in Roll

3.4.1 Force Measurements

The downforce coefficient (C_L), downforce coefficient slope ($dC_L/d(h/c)$) and drag coefficient (C_D) at different roll angles and ride heights, for the high flap setting, are presented in Figure 3-26, Figure 3-27 and Figure 3-28 respectively.

The downforce coefficient variation with ride height is presented in Figure 3-26. The results show that at a ride height of h/c=0.893 the two wing cases in roll have very similar downforce coefficients values, with C_L=1.152 and C_L =1.159 for 1.5° and 3.0° of roll respectively, while the unrolled condition has C_L=1.185. As the wing's ride height is reduced the downforce coefficient increases for all roll angles, but slightly more rapidly for the rolled cases than for the 0° case. Consequently as the ride height is reduced the plot for 3.0° roll gradually moves closer to that of the 0° case and eventually crosses the 0° plot just above h/c=0.238 where C_L=1.681, compared to C_L=1.672 for the 0° case. Between h/c=0.238 and h/c=0.218 the 3.0° case has a higher downforce coefficient than that for 0° case, reaching a maximum difference of 0.5%. Further reductions in ride height lead to a reduction in the rate of downforce increase, leading to the 3.0° case plot crossing the 0° plot once again, giving it a lower downforce coefficient than in the 0° case. At the minimum ride height tested of h/c= 0.159 the 3.0° roll case has a downforce coefficient of C_L=1.800, which is 6.9% lower

than the 0° case. Although 3.0° roll produces more downforce than 0° at certain ride heights the same is not seen in the 1.5° case. In this case as the ride height is reduced the plot remains parallel to the unrolled case with a constant offset of $-0.012C_L$ until reaching a ride height of h/c=0.476. Between this ride height and h/c=0.238 the offset between the 0° and 1.5° cases gradually decreases to $-0.004C_L$. Below h/c=0.238 the rate of downforce enhancement decreases by 16.1%, moving the plot away from the 0° case. As the 1.5° case reaches a ride height of h/c=0.129 the slope of its downforce enhancement is further reduced, indicating the proximity to the downforce reduction onset. With a further reduction in ride height the 1.5° case reaches its maximum downforce of C_L=1.974 at a ride height of h/c=0.109, the minimum ride height tested for this case because of the proximity of one tip to the ground.

In Figure 3-27 the results for the downforce coefficient slope at different ride heights are presented for the 0°, 1.5° and 3.0° roll cases. Although the downforce coefficient plots for 1.5° and 3.0° did not highlight significant changes to the slope of the plot throughout the ride height range, the downforce coefficient slopes indicate the presence of the four regions identified earlier in this chapter for the 0° case. As the ride height for the 1.5° case is reduced from 0.893c to 0.179c (Region A) the slope increases from 0.218 to 3.074. Although the progression is fairly constant some erratic behaviour is present between the ride heights of h/c=0278 and h/c=0.179. Below h/c=0.179 the wing enters Region B but reaches its lower boundary at h/c=0.169 with a slope value of 1.759. As the wing's ride height is further reduced the wing enters Region C and reaches its lower boundary at a ride height of h/c=0.149 with a value of 2.865. Below this ride height the wing enters Region D where its slope continuously decreases with further ride height reductions, reaching the minimum ride height of h/c=0.109 with a slope value of 0.693. In the 3.0° case as its ride height is reduced from h/c=0.893 the slope increases from 0.216 to a value of 2.697 at a ride height of h/c=0.238, the lower boundary of Region A. Between the ride heights of h/c=0.238 and h/c=0.198 the wing is in Region B where the slope decreases to 1.572 from the initial value of 2.697. With further reductions in ride height the wing enters Region C, where the slope increases reaching a value of

1.632 at a ride height of h/c=0.188. Below this ride height the wing enters Region D where the slope value progressively decreases with further reductions of ride height, reaching a value of 0.804 at the minimum ride height measured in this project, for this wing configuration, of h/c=0.159

The drag coefficient variation with ride height is presented in Figure 3-28. Similarly to the downforce results the roll results for the 1.5° and 3.0° roll cases do not appear to have a significant influence on the drag coefficient at a ride height of h/c=0.893, with 0°, 1.5° and 3.0° having a drag coefficient of C_D=0.144, C_D=0.141 and C_D=0.143 respectively. As the ride height is reduced, for both the 1.5° and 3.0° cases the drag coefficient plot shows similarities between themselves and the 0° case, as noted in the downforce coefficient analysis. Whilst the 1.5° roll case was almost parallel to the 0° case until reaching h/c=0.179, the 3.0° case gradually moves closer to the 0° plot and crosses it at h/c=0.397 and at h/c=0.198. As the 3.0° case reaches h/c=0.218 the rate of drag increase is reduced and the plot crosses the 0° case plot and carries on increasing at a lower rate, reaching its maximum of C_D=0.098 (27% lower than the 0° case) at h/c=0.159, the lowest ride height measured. On the 1.5° case the rate of drag increase reduces below the ride height of h/c=0.179, but continues increasing until reaching its maximum of C_D=0.114, 16% less than at the 0° roll, at a ride height of h/c=0.109.

Presented in Figure 3-29 are the results for the variation of downforce-to-drag ratio (L/D) with ride height for the different roll angles. The results show that both roll cases have very similar trends, with L/D increasing slightly as the wing's ride height is reduced and not showing inflection points in the curves, as was seen in the 0° case, for ride heights below h/c=0.159. In both the 1.5° and 3.0° roll cases the L/D results increase monotonically, with the exception of one ride height in each case where an instability appears at h/c=0.169 and h/c=0.218 for the 1.5° and 3.0° cases respectively. The results also indicate that L/D does is not affected by roll for ride heights above h/c>0.218, as both the 1.5° and 3.0° cases follow an identical trend to that seen on the 0° case. As

the lowest tip gets close to the ground and the 3.0° wing's downforce increases above the 0° case its L/D becomes greater than that of the 0° case.

3.4.2 Surface Flow Visualization

In Figure 3-31 the streaklines are shown on the suction surface of the wing at 3.0° roll for the high flap setting at h/c=0.179. Although Figure 3-31 is from the wing in roll the similarities between this case and the 0° case are evident. Similarly to the 0° roll case a spanwise bubble region is noted on the suction surface of the wing. In proximity to the wing tips the tip vortex interacts with the bubble altering its shape. The wing-tip vortices can be identified by the triangular shapes on either side of the wing that start at the leading edge of the wing next to the endplate and grow downstream. The presence of the wing tip vortex can be seen on both tips, although the shape of the vortex is slightly different on each side of the wing, with the lower side (right-hand side in figure) having a tighter triangle-shaped flow pattern than the other side, indicating that the vortex is stronger on this side (Zhang & Zerihan (2004)).

Downstream of the bubble region the flow appears to be random with the defined streaklines present upstream of the bubble no longer present. This characteristic highlights the presence of a turbulent flow.

On the flap's suction surface the mid-span flow appears to be parallel to the freestream direction. The curved flow present on the inner flap tips appears to have a more pronounced curvature on the side of the wing that is closer to the ground, indicating the presence of a stronger vortex than on the other side.

3.4.3 Discussion

The force results from the wing in the roll condition indicated that, although at large ride heights a wing in roll will produce less downforce than a wing at 0° of roll, once the wing is in ground effect a rolled wing may be capable of producing more downforce than the level wing. Although the results were not presented this characteristic was also noted on the low-flap-angle configuration as shown in Figure 3-30. In this case the increase in downforce was seen across a greater range of ride heights than on the high-flap-angle condition.

This increase in downforce seen on a wing operating in roll can be explained by considering an idealised uniform lift distribution along the span of the wing. Using Figure 3-32 as a visual aid, if we then assume that the downforce coefficient plot (Figure 3-1) for the wing at 0° of roll represents the sectional coefficients of the wing, along the span, and finally considering the centre of the wing is at the nominal ride height, with the wing tips at different ride heights due to the roll, we can calculate the wing's downforce coefficient by integrating the section coefficients along the span. These assumed sectional coefficients are indicated in red in Figure 3-32. This leads to an overall downforce coefficient of C_L=1.205, which is only 1% lower than the measured value.

Analysis of L/D (Figure 3-29) shows that at lower ride heights (h/c<0.198) the rolled cases are slightly more efficient than the zero-roll case, for the same nominal ride height (i.e. centre-span). This is attributed to the lower tip operating at ride heights of higher L/D than the nominal ride height and due to the higher tip operating at a ride height where the difference in L/D to the nominal ride height is smaller than the difference between the nominal ride height to the lowest tip, giving a higher net result for the cases in roll.

Analysis of the downforce coefficient slope showed that the four regions that help identify the mechanisms behind the the force-enhancement and -reduction regions were present indicating that even under roll conditions a wing still performs as its levelled counterparts. Despite the four regions being present they were condensed into a smaller range of ride heights and their upper boundary translated to greater ride heights as the roll angle was increased.

3.5 Conclusions

In this chapter the results for a wing operating in an undisturbed flow at different roll and yaw settings were presented. These results were considered as the baseline results that will be used in a Chapter 5 to compare with the results of the wing immersed in a turbulent flow.

The results presented in this chapter showed that the wing operated as expected, with similar force-enhancement and -reduction trends as those described by other authors in the literature review of Chapter 1.

The presence of a separated region on the wing's suction surface was also noted. A comprehensive study of the separation bubble was outside the scope of this project but the data obtained indicated that changes to its shape with ride height lead to changes to the local flow and consequently force results.

The computational results were compared against the force measurements and surface flow visualisation carried out in the wind tunnel. The results showed that CFD under-predicted the downforce results and that this under-prediction increased at lower ride heights. In the case of the downforce coefficient the under-prediction reached a maximum value of 2.73%, whilst drag was over-predicted by up to 5.98%. Comparing the predicted surface streamlines with the results obtained through surface flow visualization showed good agreement. This gave confidence that the computational method would lead to meaningful results with similarities to those from the wind tunnel.

The yaw results showed that a wing operating in yaw generates similar forces to those at zero yaw when out of ground effect, but once in ground effect the wing in yaw will experience a reduction in downforce and drag.

The roll results showed that for the same nominal ride height it is possible to generate more downforce with the wing at low roll angles than with the wing at zero roll. A peculiar situation caused by each wing tip operating at different ride heights along the downforce enhancement slope, which leads to the downforce and efficiency of the wing being greater than the zero roll case.

Table 3-1: Variation with ride height ($\frac{h}{c}$) of separation position ($\frac{x_S}{c}$), reattachment position ($\frac{x_R}{c}$) and bubble length ($\frac{x_{LS}}{c}$) as a percentage of chord for both high (23.9°) and low (13.8°) flap settings. (0º yaw, 0º roll). δ= ±0.1%

Low Flap: 13.8°			
$\frac{h}{c}$	$\frac{x_S}{c}$	$\frac{x_{LS}}{c}$	$\frac{x_R}{c}$
0.060	27.4	8.5	35.8
0.089	28.7	10.1	38.8
0.179	30.5	12.5	43.1
0.397	30.9	12.7	43.6
0.893	31.5	12.9	44.3

High Flap: 23.9°			
$\frac{h}{c}$	$\frac{x_S}{c}$	$\frac{x_{LS}}{c}$	$\frac{x_R}{c}$
0.060	30.4	7.6	38.0
0.089	32.8	10.2	43.0
0.179	35.5	10.8	46.3
0.397	38.4	11.3	49.6
0.893	39.3	12.1	51.4

Table 3-2: Variation with ride height ($\frac{h}{c}$) of separation position ($\frac{x_S}{c}$), reattachment position ($\frac{x_R}{c}$) and bubble length ($\frac{x_{LS}}{c}$) as a percentage of chord for high flap setting (23.9°) at 5º yaw. (0º roll). δ= ±0.1%

High Flap: 23.9°			
$\frac{h}{c}$	$\frac{x_S}{c}$	$\frac{x_{LS}}{c}$	$\frac{x_R}{c}$
0.060	27.5	7.3	34.8
0.089	28.4	8.0	36.4
0.179	29.5	9.1	38.6
0.397	32.5	9.6	42.1
0.893	33.2	10.5	43.7

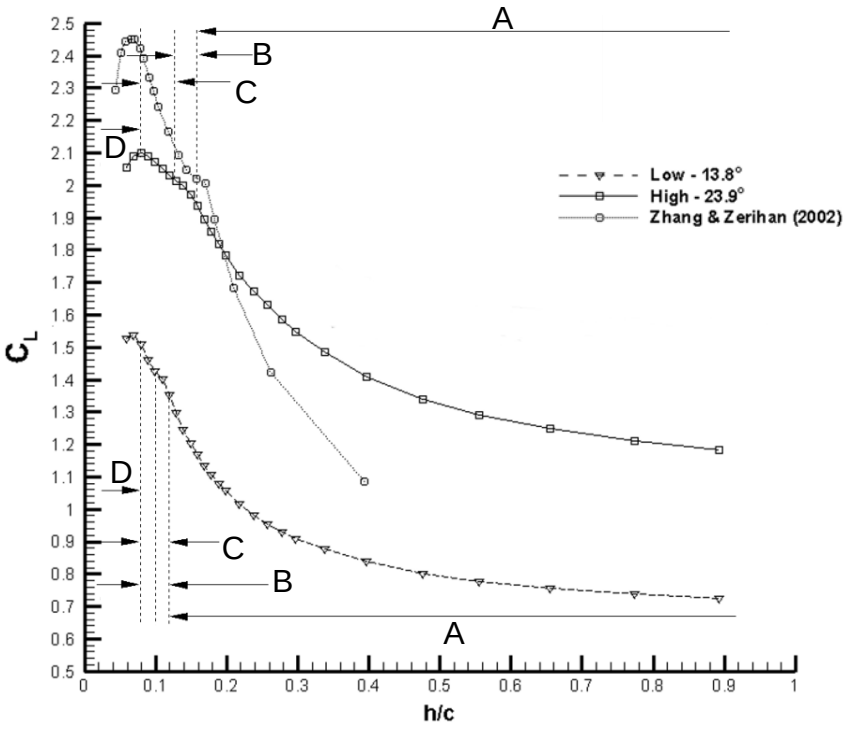

Figure 3-1: Variation of downforce coefficient with ride height for both low and high flap settings and comparison with other authors' results (0º yaw, 0º roll). Δ= ±1.40E-02

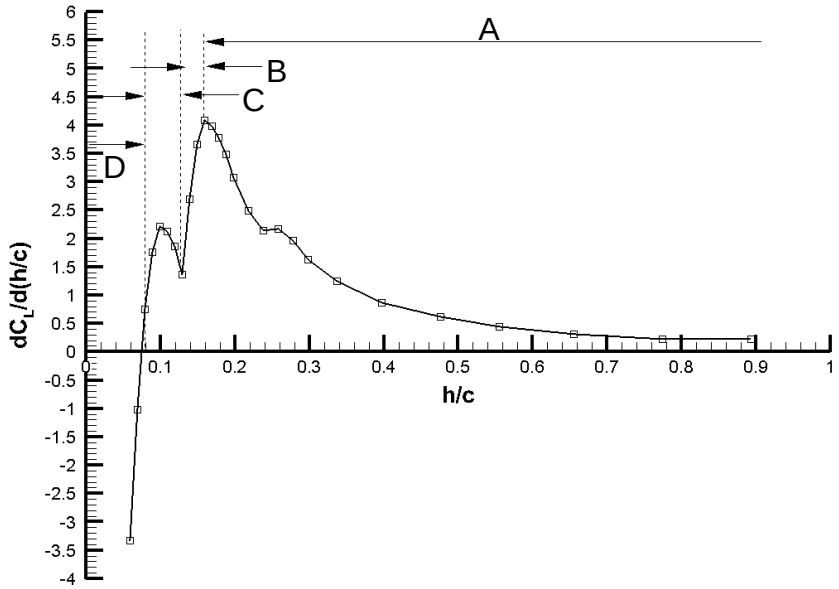

Figure 3-2: Variation of downforce slope with ride height for high flap setting (0º yaw, 0º roll). Δ= ±7.18E-02

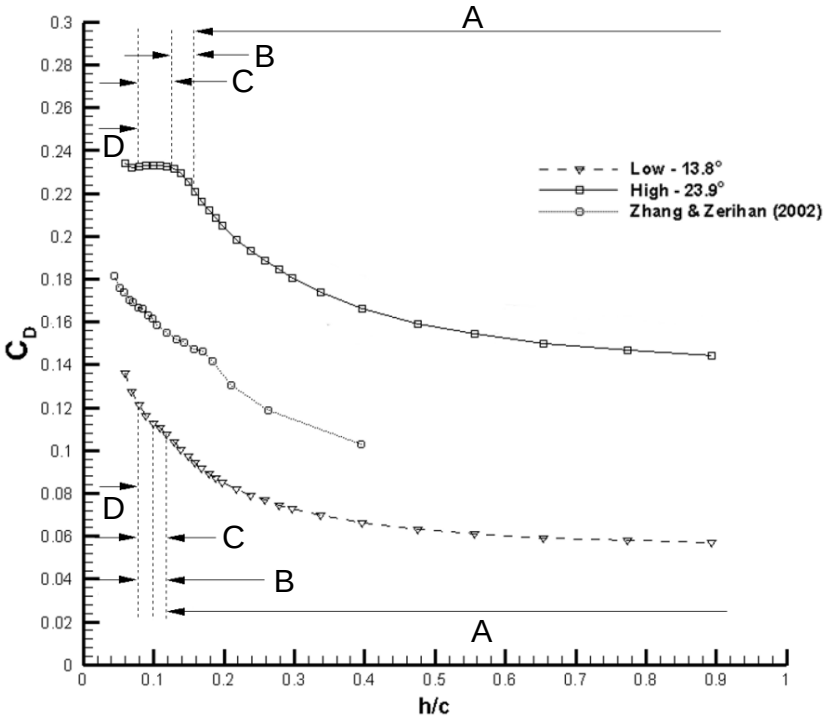

Figure 3-3: Variation of drag coefficient with ride height for both low and high flap settings and comparison with other authors' results (0º yaw, 0º roll). Δ= ±2.33E-03

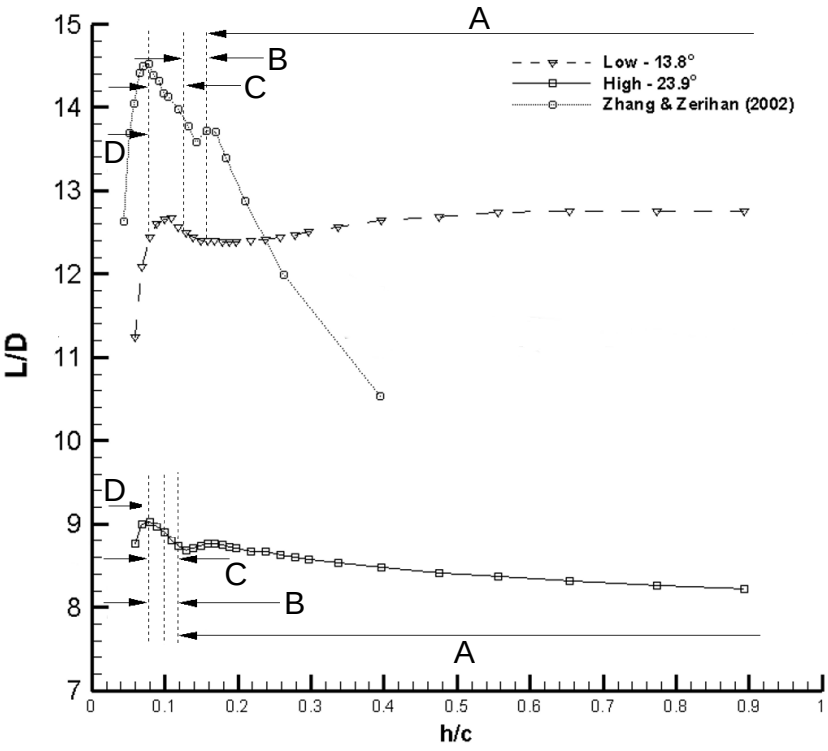

Figure 3-4: Variation of lift-to-drag ratio with ride height for low flap setting and comparison with other authors' results (0º yaw, 0º roll). Δ= ±2.26E-01

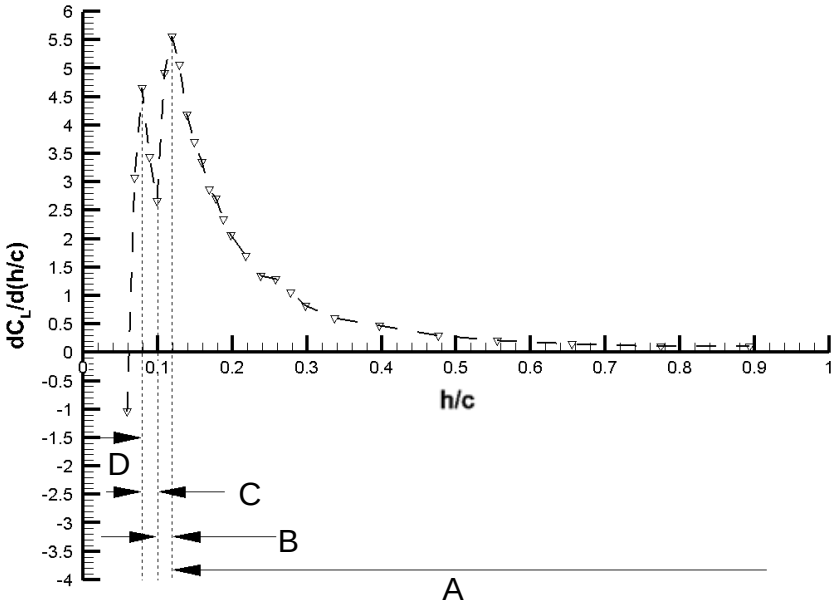

Figure 3-5: Variation of downforce slope with ride height for low flap setting (0º yaw, 0º roll). Δ= ±7.49E-02

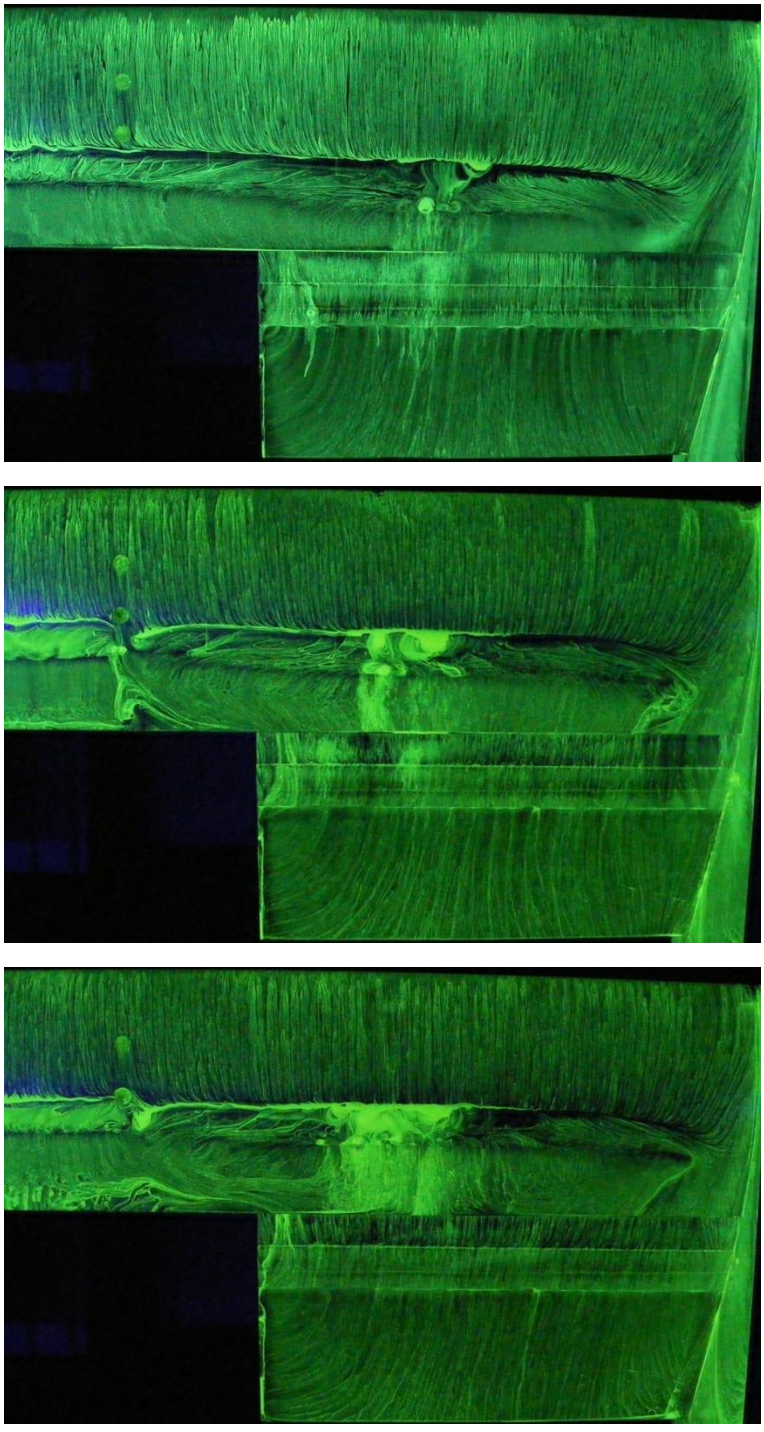

a)
h/c=0.179

b)
h/c=0.089

c)
h/c=0.060

Figure 3-6 Surface flow visualisation on suction surface of wing at high flap setting; leading edge uppermost, CFD on left, experimental on right. (0º yaw, 0º roll)

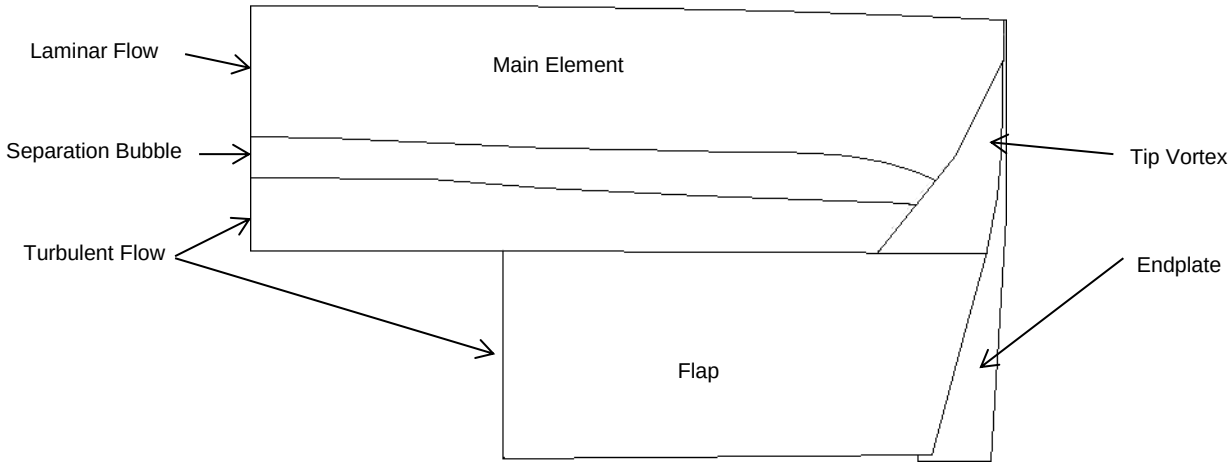

Figure 3-7 Schematic of the flow pattern on the wing's suction surface; leading edge uppermost, wing tip on right

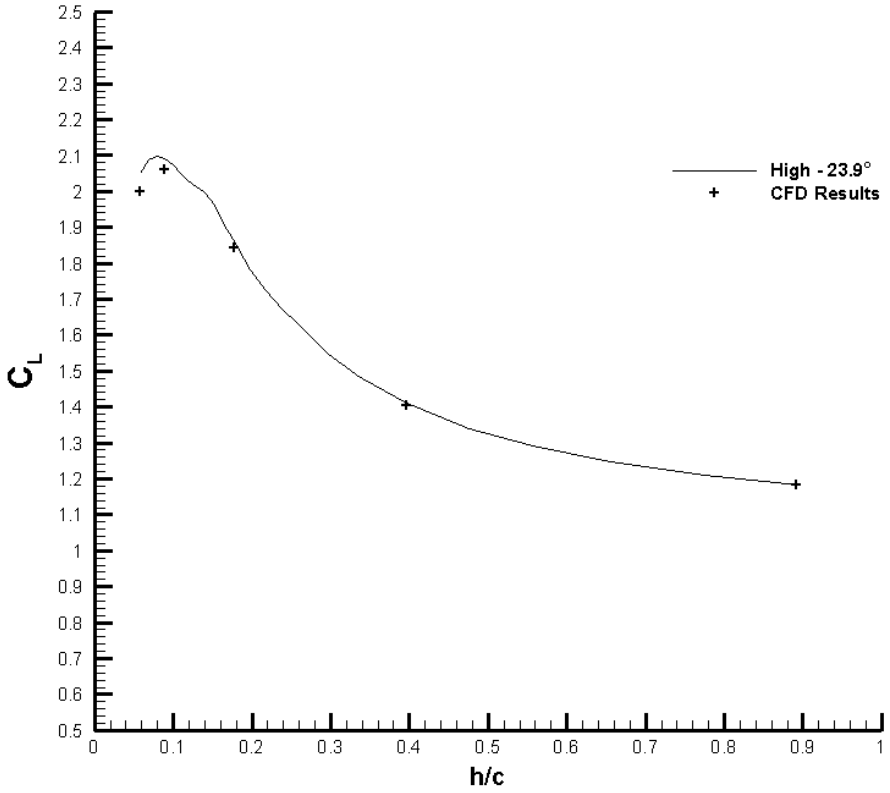

Figure 3-8: Comparison between experimental and computational C_L data at different ride heights for the high flap setting (0º yaw, 0º roll).

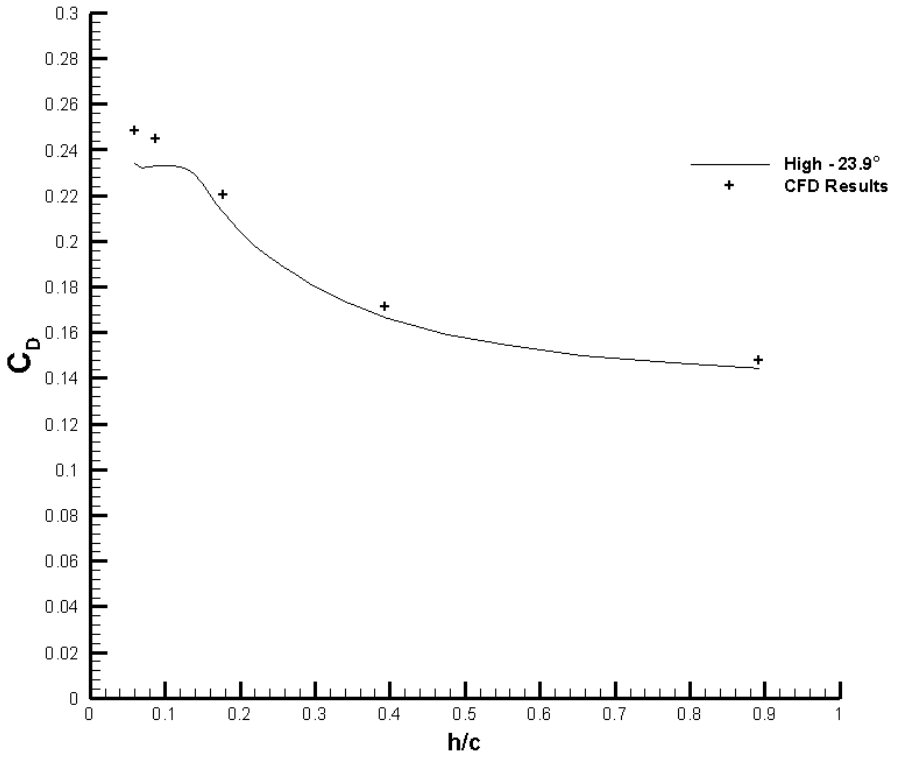

Figure 3-9: Comparison between experimental and computational C_D data at different ride heights for the high flap setting (0º yaw, 0º roll).

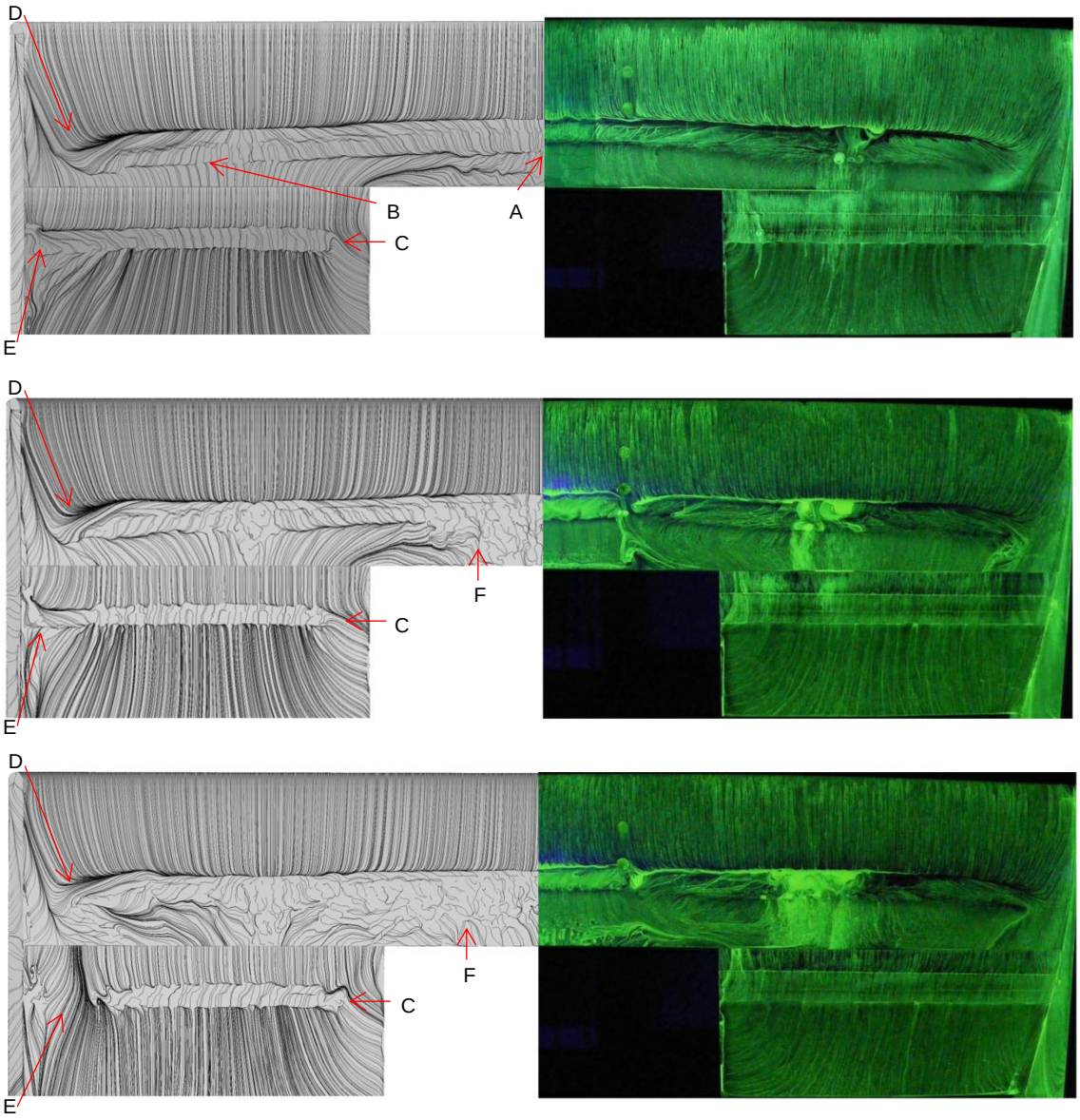

Figure 3-10 Comparison of experimental and CFD-predicted surface flow on suction surface of wing at high flap setting; leading edge uppermost, CFD on left, experimental on right. (0º yaw, 0º roll)

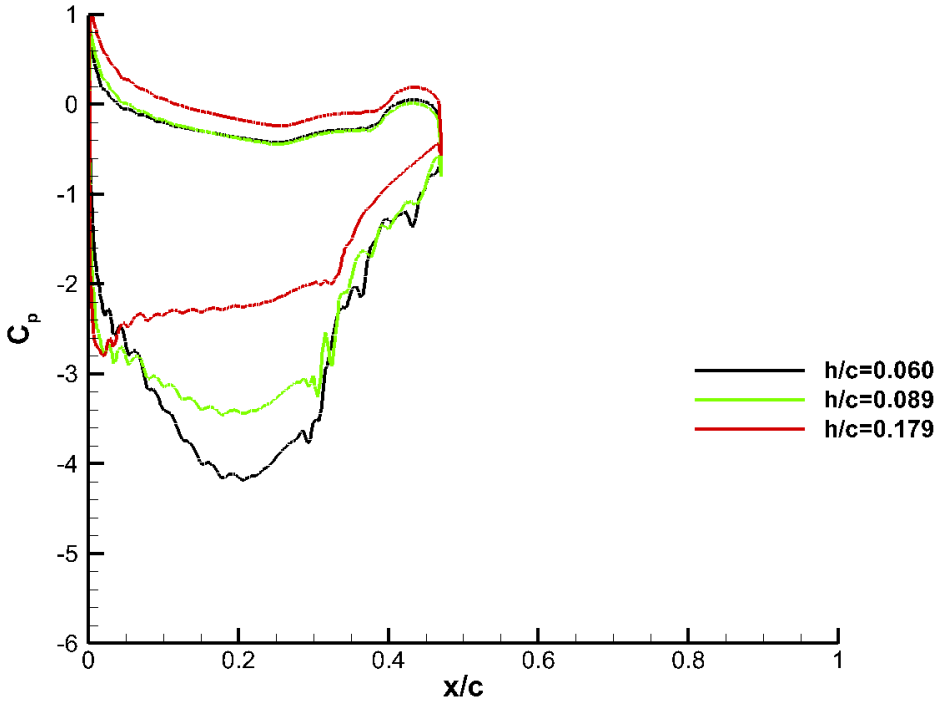

Figure 3-11: Variation with ride height of chordwise pressure distribution around the wing's main plane at mid-span (0º yaw, 0º roll, CFD results)

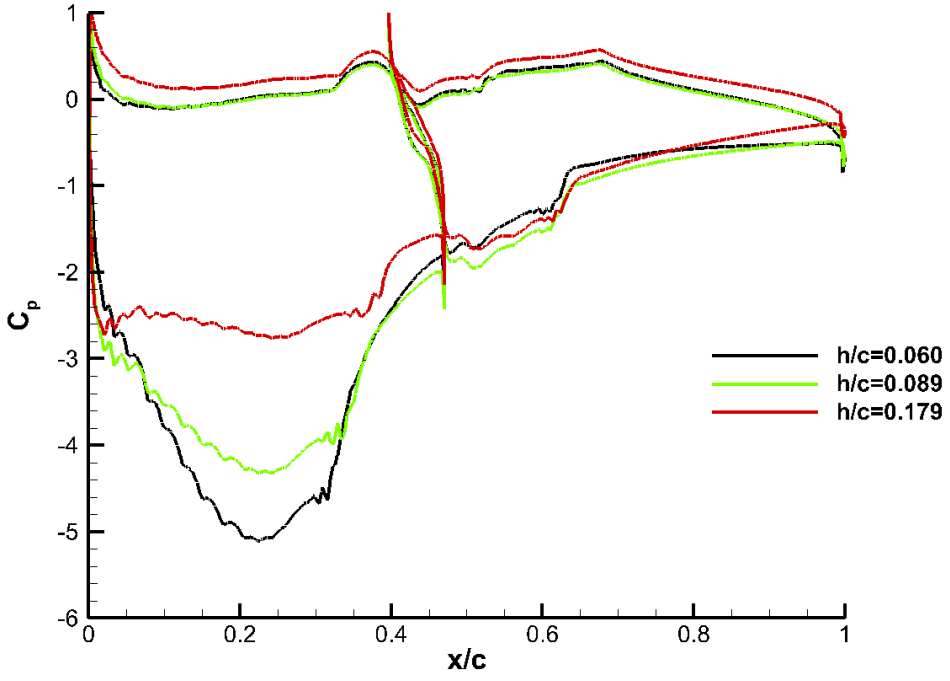

Figure 3-12: Variation with ride height of chordwise pressure distribution around the wing's main plane and flap at flap mid-span (0º yaw, 0º roll, CFD results)

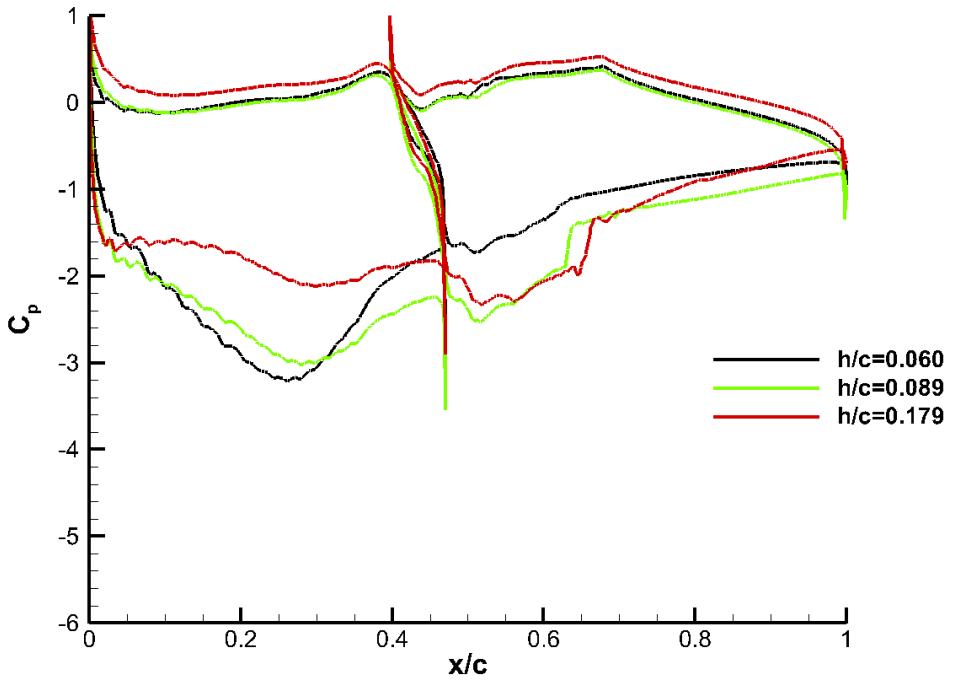

Figure 3-13: Variation with ride height of chordwise pressure distribution around the wing's main plane and flap at the wing tip (0º yaw, 0º roll, CFD results)

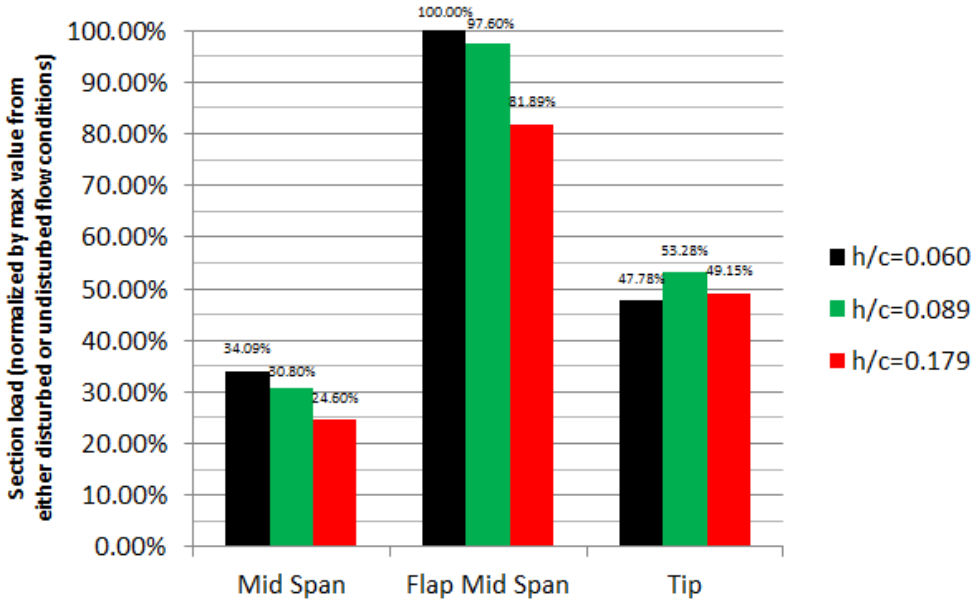

Figure 3-14: Bar graph of CFD-predicted wing section loading, normalized with the maximum loading seen in the data range. (0º yaw, 0º roll, CFD results)

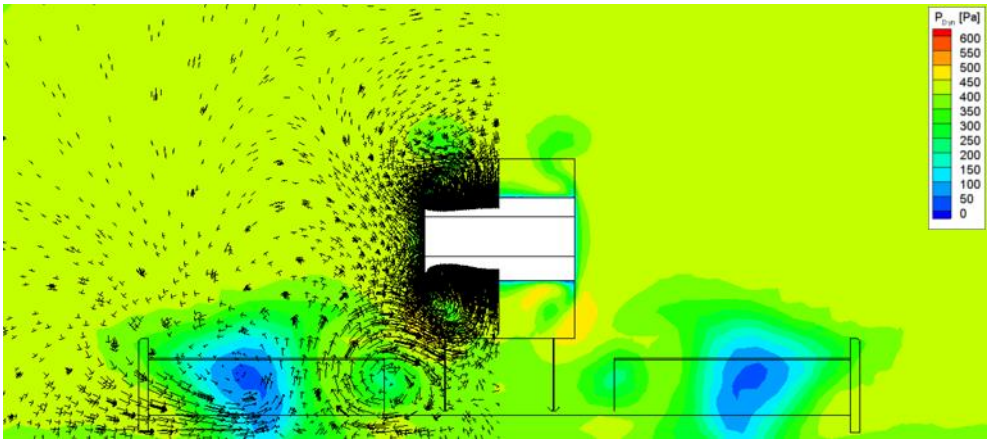

Figure 3-15: CFD-predicted velocity vectors and dynamic pressure contours at x/c=1 behind wing at h/c=0.060. (0º yaw, 0º roll)

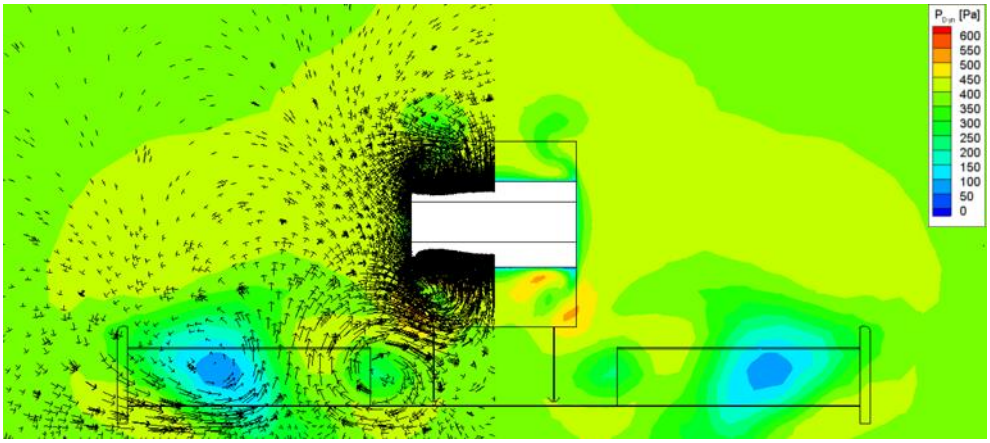

Figure 3-16: CFD-predicted velocity vectors and dynamic pressure contours at x/c=1 behind wing at h/c=0.089. (0º yaw, 0º roll)

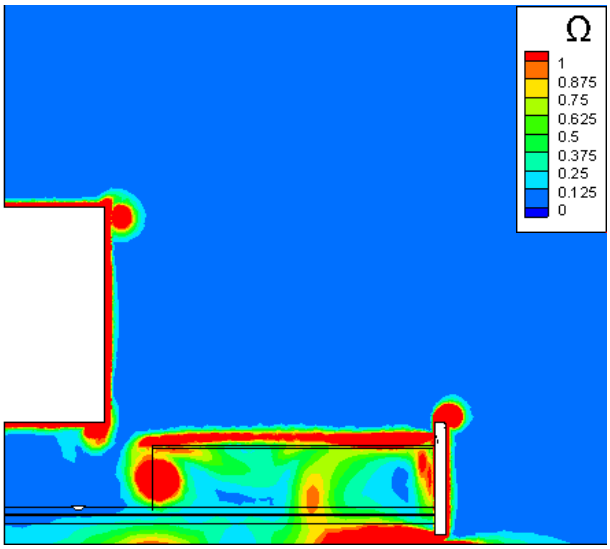

Figure 3-17: Contour of CFD-predicted normalized vorticity magnitude at h/c=0.060 at the trailing edge of the endplate for the high flap (23.9°) setting (0º yaw, 0º roll)

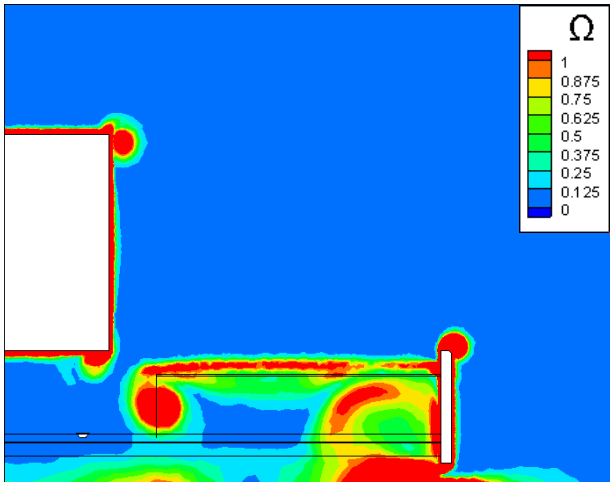

Figure 3-18: Contour of CFD-predicted normalized vorticity magnitude at h/c=0.089 at the trailing edge of the endplate for the high flap (23.9°) setting (0º yaw, 0º roll)

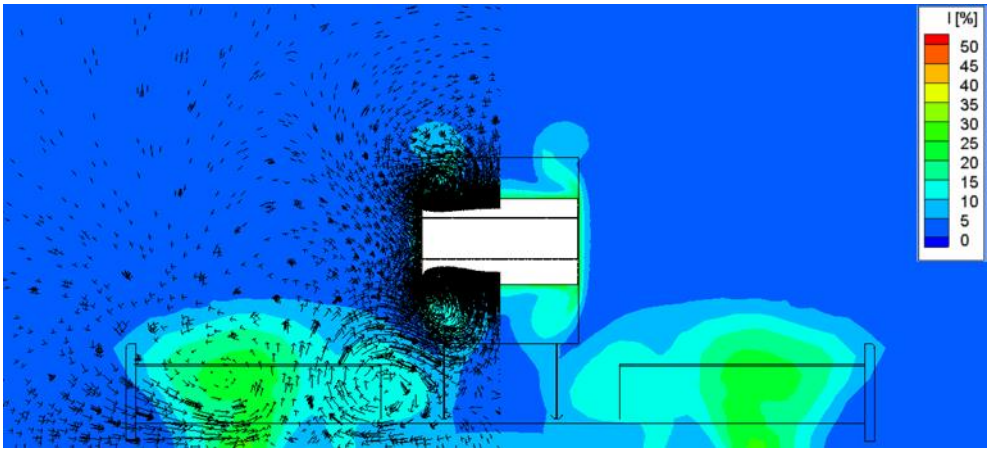

Figure 3-19: CFD-predicted velocity vectors and turbulence intensity contours at x/c=1 behind wing at h/c=0.060 (0º yaw, 0º roll)

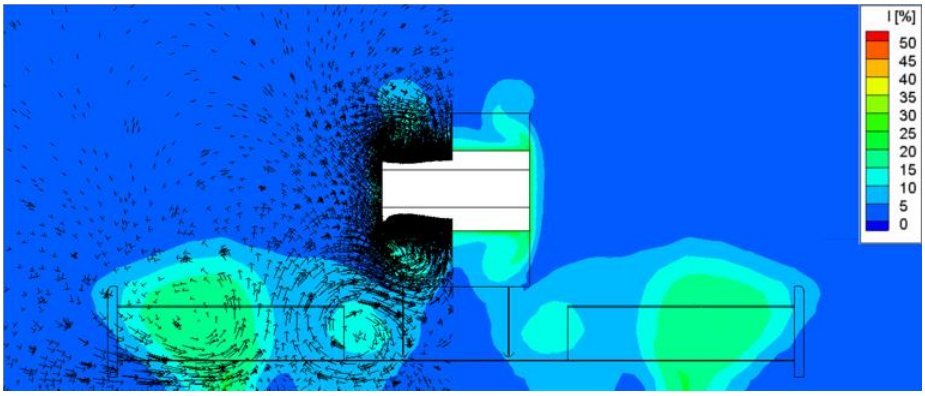

Figure 3-20: CFD-predicted velocity vectors and turbulence intensity contours at x/c=1 behind wing at h/c=0.089 (0º yaw, 0º roll)

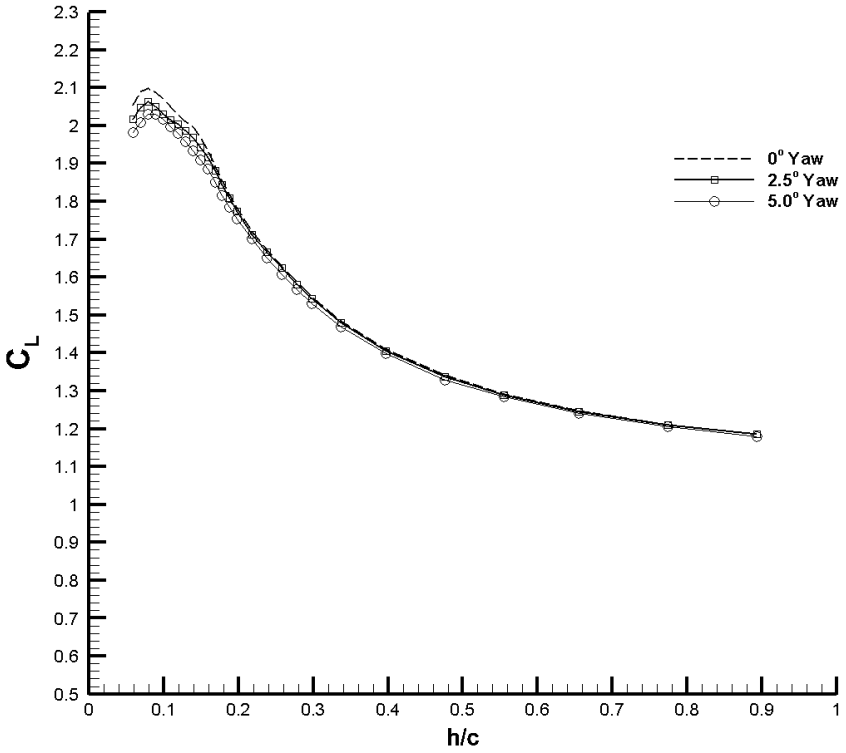

Figure 3-21: Variation of downforce coefficient with ride height at different yaw angles for the high flap (23.9°) setting (0º roll). Δ= ±1.40E-02

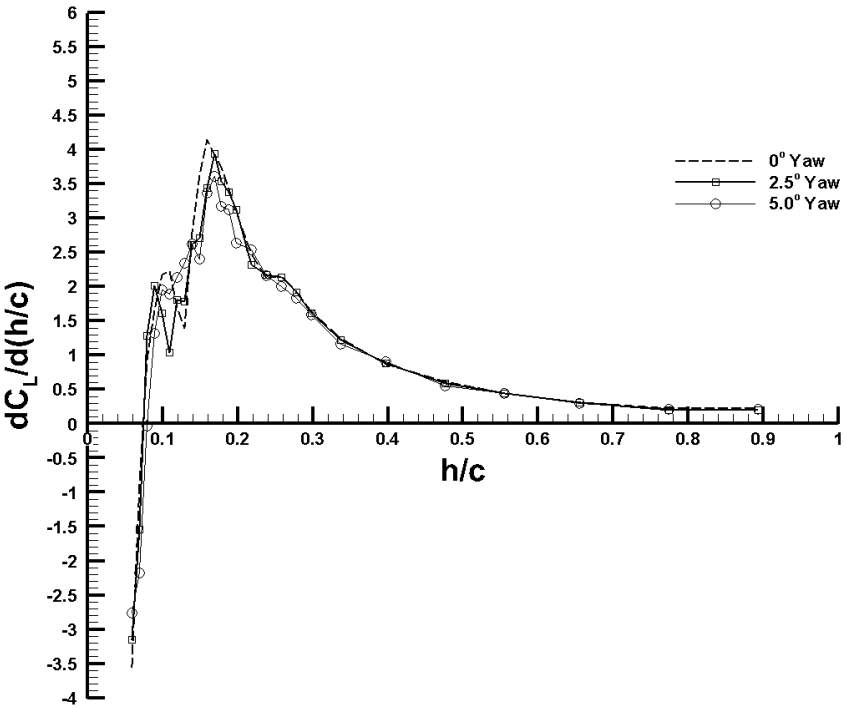

Figure 3-22: Variation of downforce slope with ride height at different yaw angles for the high flap (23.9°) setting (0º roll). Δ= ±7.16E-02

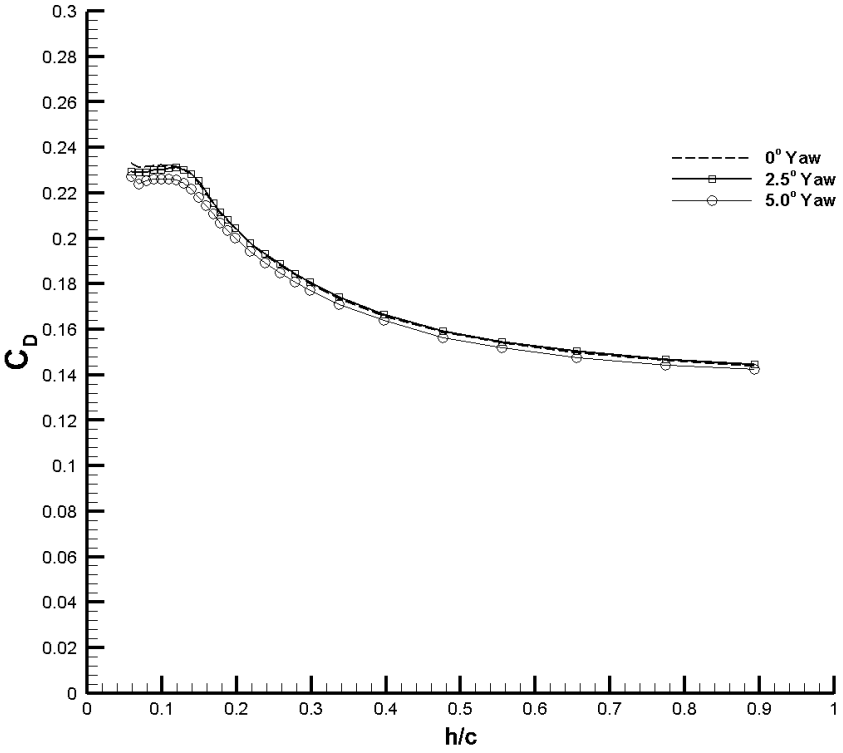

Figure 3-23: Variation of drag coefficient with ride height at different yaw angles for the high flap (23.9°) setting (0º roll). Δ= ±2.33E-03

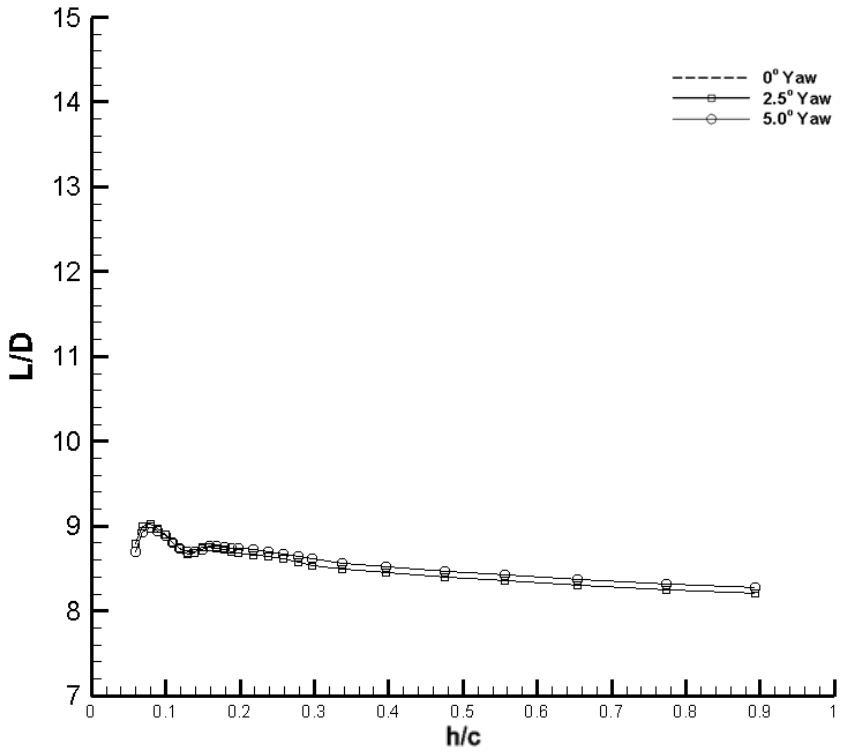

Figure 3-24: Variation of lift-to-drag ratio with ride height at different yaw angles for low flap (13.8º) setting (0º roll). Δ= ±2.31E-01

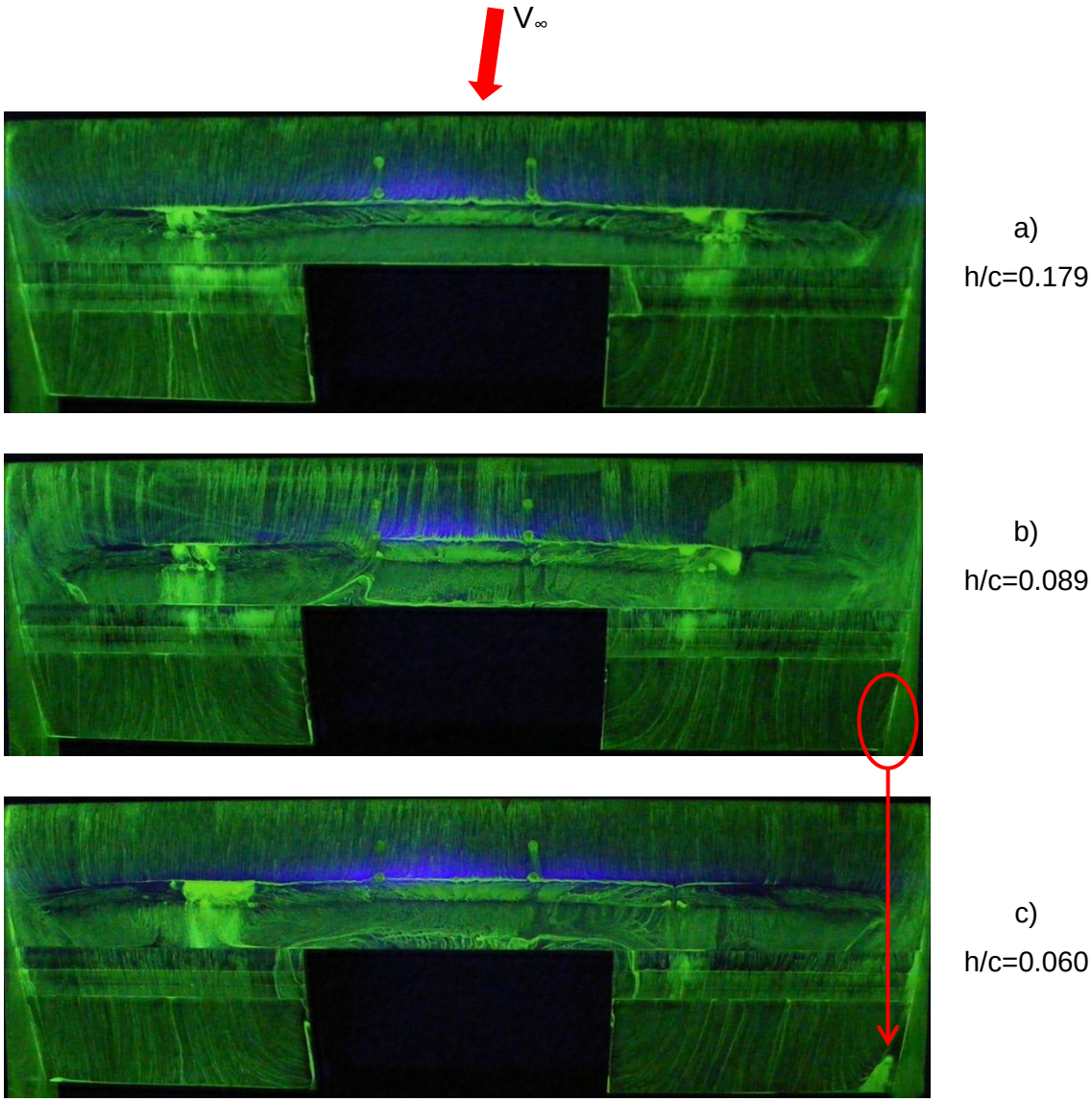

Figure 3-25: Surface flow visualization on suction surface of high flap (23.9°) setting at 5.0º of yaw; leading edge uppermost, crossflow component from right to left. (0º roll)

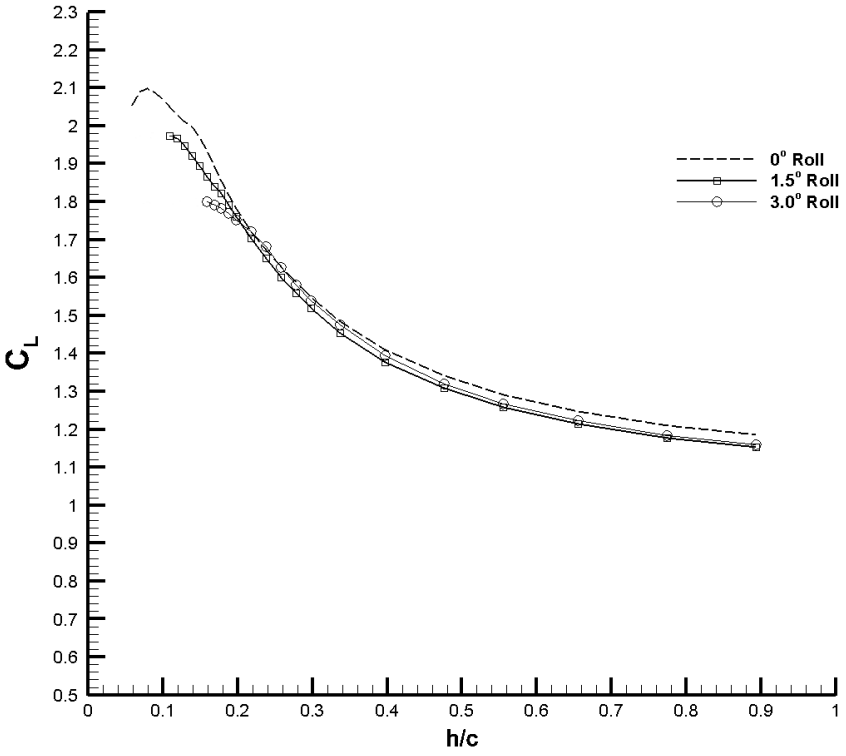

Figure 3-26: Variation of downforce coefficient with ride height at different roll angles for the high flap (23.9°) setting (0º yaw). Δ= ±1.40E-02

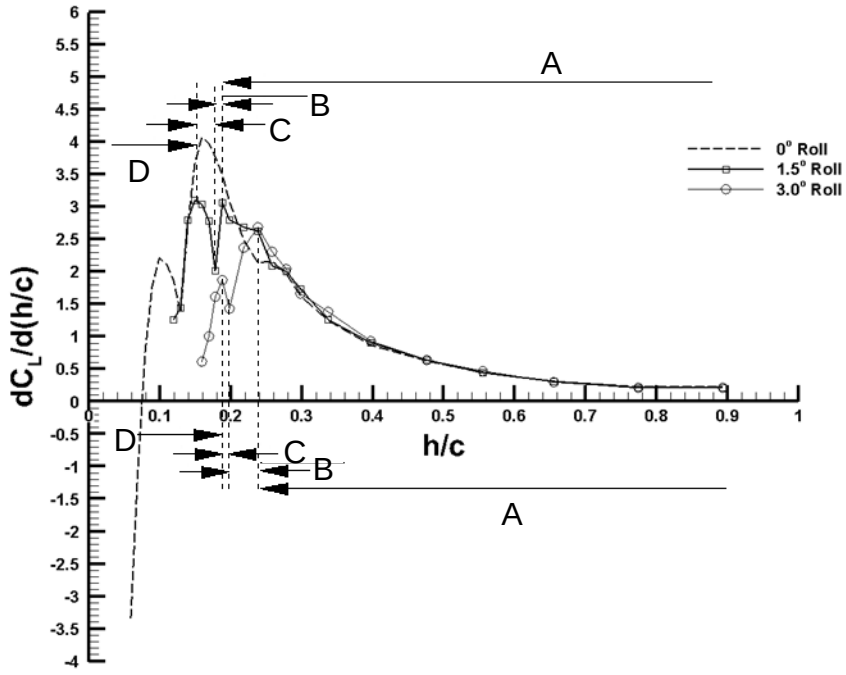

Figure 3-27: Variation of downforce slope with ride height at different roll angles for the high flap (23.9°) setting (0º yaw). Δ= ±7.77E-02

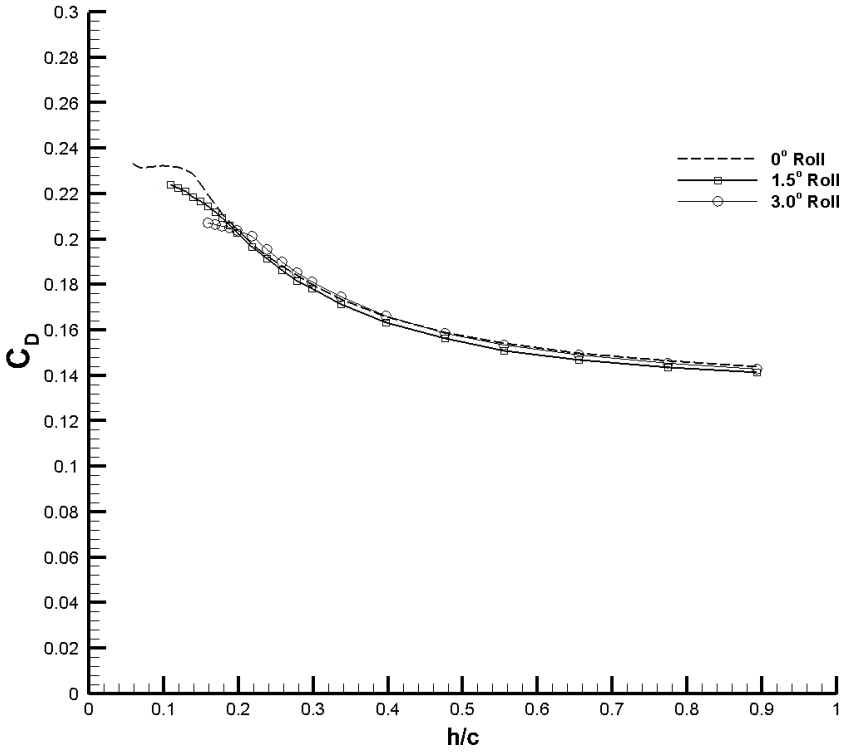

Figure 3-28: Variation of drag coefficient with ride height at different roll angles for the high flap (23.9°) setting (0º yaw). Δ= ±2.33E-03

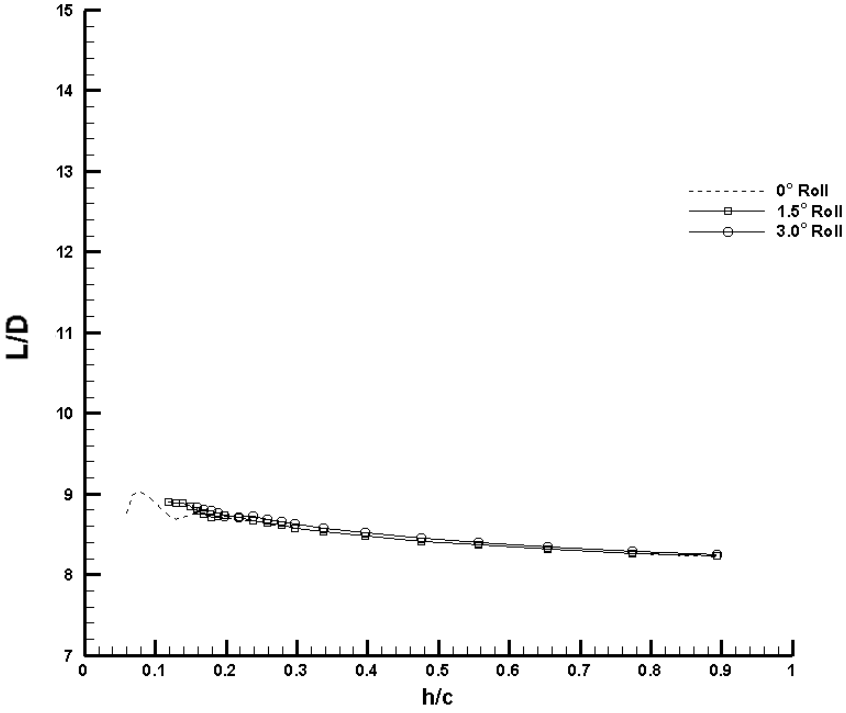

Figure 3-29: Variation of lift-to-drag ratio with ride height at different roll angles for high flap (23.9°) setting (0º yaw). Δ= ±2.35E-01

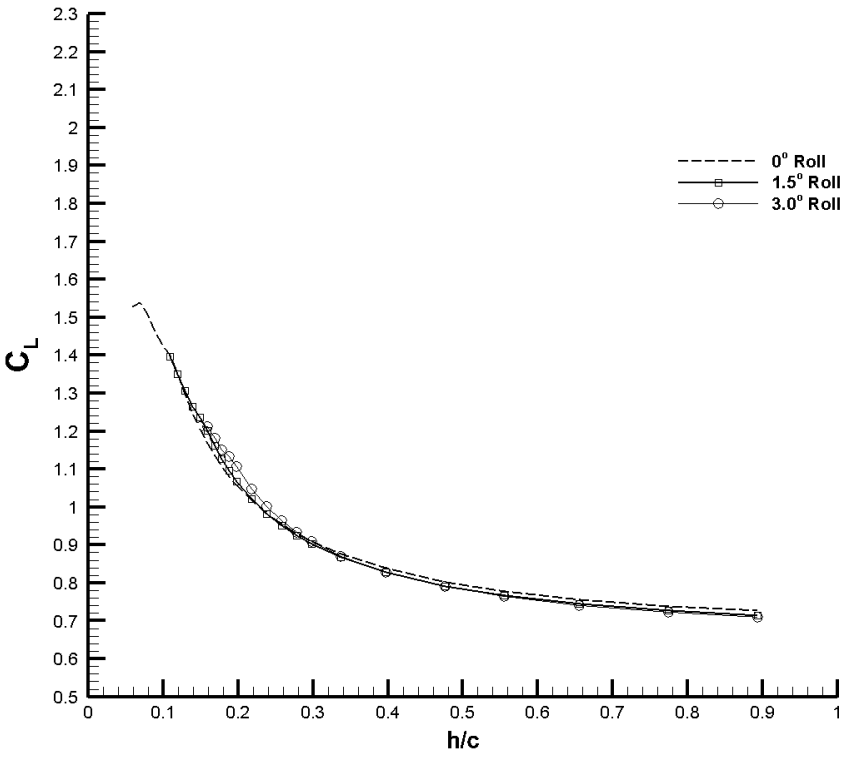

Figure 3-30: Variation of downforce coefficient with ride height at different roll angles for the low flap (13.8°) setting (0º yaw). Δ= ±1.40E-02

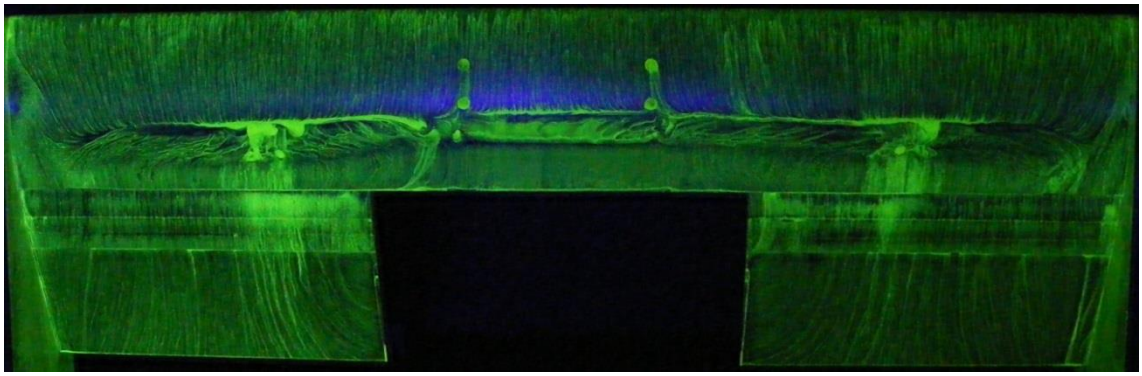

Figure 3-31: Surface flow visualization on suction surface of high-flap setting wing at 3.0º of roll at h/c=0.179; leading edge uppermost, wing tip on right is the closer to the ground

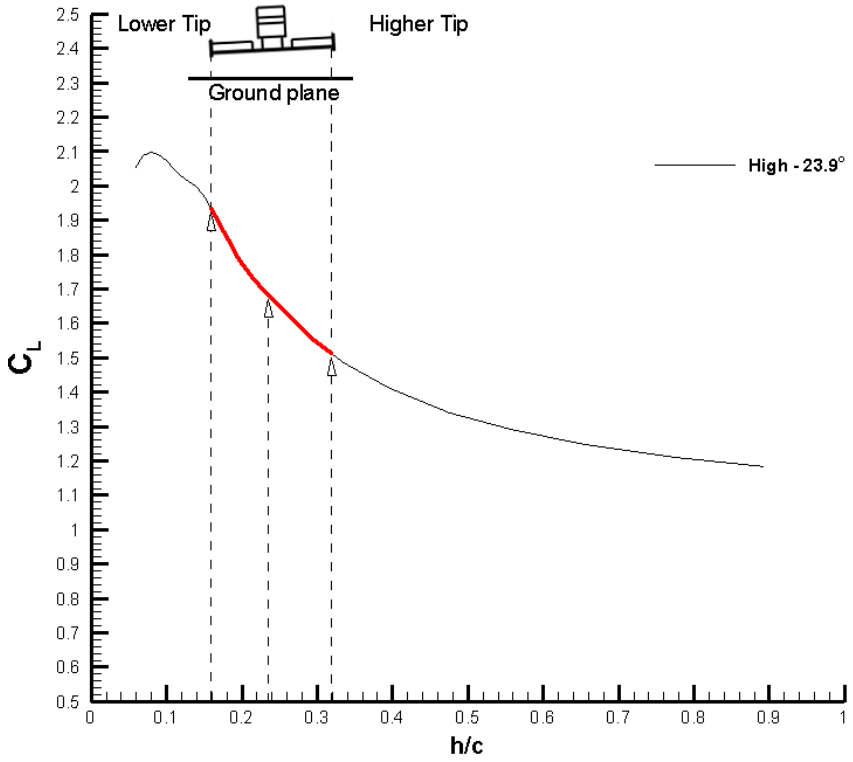

Figure 3-32: Variation of downforce coefficient with ride height for high flap setting and 0° roll, reproduced from Figure 3-1, with assumed variation along the span of the wing superimposed in red for 3.0° roll

4 Upstream Body Wake

In this chapter the results from the wake-generating model's wake survey will be presented and discussed, in order to understand the significant flow features of the wake, its development and influence on vehicles travelling immersed in it.

A wake survey using a laser doppler anemometer (LDA) was carried out, but was not completed due to equipment malfunctioning. With the incomplete data obtained with the LDA a computational approach was validated allowing for a more detailed understanding of the wake, by filling in the blanks left by the LDA wake survey.

Limitations in test-section length led to the wake-generating model being placed upstream of the rolling road, mounted on a fixed ground on top of the boundary-layer suction box. Due to the unfavourable interaction between the boundary layer suction and the flow under the model, and consequently on the wake-generating model's wake, it was decided to run the disturbed case experiments with the boundary layer suction turned off. A similar solution was used by Wilson et al. (2008) in their studies, where the leading wake-generating body was placed on a stationary ground plane ahead of the rolling road. In their study the authors compared the wake generated by the model placed on the rolling road with the wake generated with the model ahead of the rolling road, placed over a stationary ground plane, and concluded that the changes caused by the stationary ground plane had a negligible effect on the wake shape.

Experiments were conducted at a freestream velocity and turbulence intensity, ahead of the wake-generating model, of 25 ms^{-1} and 0.7% respectively. Figure 4-1 shows a schematic of the wake generator.

4.1 Measurement Planes

Figure 4-2 shows the longitudinal and transversal planes behind the body that were measured during this research. The transversal planes (A & B) represent a half-car separation (A - the plane where the leading edge of the trailing wing was located in subsequent tests, x/c=4.365), and a quarter-car separation (B,

x/c=2.183). These planes were taken in order to understand the wake development and the flow a trailing vehicle would encounter.

Three longitudinal planes, which were aligned with the trailing-wing centreline (C, y/c=0), the flap mid-span (D, y/c=0.744), and trailing-wing tip (E, y/c=1.488), were also measured. These planes allow the local flow angle, i.e. upwash or downwash, at different spanwise locations to be evaluated. They also allowed the understanding of how the flow velocity varied between the rear of the upstream body and front of the wing, and show the development of the wake downstream of the body.

4.2 Experimental Results

4.2.1 Velocity Profiles

The normalized velocity profiles obtained with the LDA are shown in Figure 4-3. In this figure u/U shows the normalized horizontal velocity (normalized by freestream) and w/U the normalized vertical velocity (upwash or downwash), measured at three spanwise locations across the wake. These locations are defined as the intersection between the transverse plane A with longitudinal planes C, D and E. This is equivalent to the flow at 3 spanwise locations (centreline, mid-semi-span, and wing tip) at the leading edge of the trailing wing. In the plots the computational results that will be discussed later are also presented.

The results for the centreline (Figure 4-3a) show a significant reduction in u/U, by as much as 57% (u/U=0.43) of the freestream value at a height of z/c=1.259. Below this height u/U increases slightly to 0.57 at z/c=0.146, the lowest point that could be measured with the LDA. Above y/c=1.259 the normalized velocity increases monotonically, reaching the freestream value at approximately z/c=2.336. As we measure further away from the rolling road a vertical flow in the upward direction increases in velocity, reaching the maximum of w/U=0.233 at z/c=0.693, indicating the presence of upwash. Above this height the vertical velocity gradually decreases although it does not reach zero in the measured height range.

The flap mid-span (Figure 4-3b) normalized velocity plots present a slightly complicated profile and can be separated into two distinct regions of velocity deficit. These separate regions consist of a region where downwash (w/U<0) is present for heights below z/c=1.150 and a region of upwash (w/U>0) for all points above this height. A significant reduction in the normalized horizontal velocity is noted in close proximity to the ground with a local minimum of u/U=0.82 at z/c=0.146, the lowest point measured with the LDA. Above this height the normalized velocity increases almost linearly until it reaches z/c=0.511, the upper value for the operating range of a monoposto car front wing, with a value of u/U≈0.95. This value remains almost unchanged until z/c=0.967, where it starts to decrease until reaching an absolute minimum of u/U=0.74 at z/c=1.697. Above this value it increases monotonically reaching the freestream value at z/c=2.427.

In Plane E, which is aligned with the wheel of the wake-generator, (Figure 4-3c) the normalized velocity remains at a freestream value for heights above z/c=1.058. Below this height the normalized velocity decreases to a minimum u/U=0.77 at z/c=0.146. Also evident is the presence of downwash (w/U<0) throughout the height range, with it trending to zero for heights above z/c=2.5. The downwash present in Plane E is caused by the flow being turned around the wheel of the wake generator and reaches a maximum value of w/U=0.11 at a height of z/c=1.5. Below and above this height downwash decreases approximately linearly and tends towards zero far above the ground.

4.2.2 Validation of CFD Results

The validation of computational results with experimental data is an important part of any computational study as it gives an indication of how representative of real flows the results are. With this in mind, presented in Figure 4-4 and Figure 4-5 are the relative errors[1], normalized by the maximum u and w values respectively, between CFD-predicted and LDA-measured results for the longitudinal velocity (u) and vertical velocity (w) at Plane A. The turbulence

[1] $Relative\ Error = \frac{X_{CFD} - X_{LDA}}{X_{\max LDA}} \times 100\%$, where X is u or w or I

intensity ($I = \frac{u'}{U}$) relative error, normalized by maximum turbulence intensity, at Plane A is presented in Figure 4-6. Inspection of the normalized longitudinal velocity component (u/U) relative error (Figure 4-4) shows a region of under-prediction downstream of the wake-generator's rear wing (1.4<z/c<2.2), an area where the trailing wing was not tested. Focusing the analysis on the region where the trailing-wing operates (z/c<0.893 and -1.47<y/c<1.47) the results show an average error, in this region, of -0.19% for the horizontal velocity component. The vertical velocity component (w/U) relative error (Figure 4-5) shows the error ranging between -20% and +20%, but considering the operating region of the trailing wing an average error of +0.63% is obtained. The turbulence intensity results (Figure 4-6) show a central area below z=1.8 and spanning between -0.6<y/c<+0.6 where the turbulence intensity is mostly under-predicted, but outside this region is fairly well predicted. Considering the operating region of the trailing wing we see that a significant area of the aforementioned under-predicted region is inside the operating region of the wing, leading to an average error of -6.57%.

Returning to Figure 4-3 and comparing the experimental and computational plots shows that despite the magnitude not being always accurate the overall shapes are adequate and the important wake features, in respect to normalized horizontal and vertical velocity, were satisfactorily replicated at each spanwise section.

The results from the mid-span (Figure 4-3a), within the operating range of the downstream wing h/c<0.893, show an average error of -7.02% for u/U and -8.05% for w/U. At the trailing-wing flap mid-span (Figure 4-3b) the results show u/U underestimated by 2.42%, whilst w/U was overestimated by 3.19%. In the case of the trailing-wing tip (Figure 4-3c) both u/U and w/U were underestimated by 0.48% and 3.21%, respectively. Although all the vertical normalized velocity trends were well captured in CFD, the low vertical velocity present in the experimental setup led to errors due to the computational predictions being slightly different than those measured in the wind tunnel. These differences led to the vertical velocity computational results being up to -

200% of those measured in the wind tunnel such as in the case at mid-semi-span (Figure 4-3b).

Despite the over-prediction of the vertical velocity component and under-prediction of turbulence intensity in the operating range of the wing's leading edge, the computational approach is able to capture the velocity trends seen in the experimental wake. It is felt that this shows sufficient agreement with the experimental wake survey results to give confidence that it can be used, with care, to fill gaps in the experimental data set.

4.2.3 LDA Surveys

4.2.3.1 Transversal Planes

The normalized longitudinal velocity in the wake of the upstream body is presented in Figure 4-7, for Planes A and B. The figures show the development of the wake downstream of the wake-generating model. Although the figure only presents data from a single velocity component it is possible to identify two distinct flow features, in both planes. These features consist of the tip vortices created by the rear wing (labelled 1 in Figure 4-7a), and low velocity regions (labelled 2) typical of a wake.

The two tip vortices seen in Planes A and B are generated by a flow across the top of the endplate due to the pressure gradient between the suction and pressure surface of the wing, and also the outside of the endplate. As the vortices travel downstream from the endplate and cross Plane B their shape is well defined and their core position can be seen. As the vortices travel further downstream they start dissipating and when reaching Plane A their definition is reduced and the core position is no longer identifiable.

Although limited information is available it is believed that the low-velocity region, present at the top of Plane A (2), may be caused by separated flow on the flap element. Whilst the wake region (labelled 3 in Figure 4-7b) is believed to be caused by the counter-rotating trailing vortices pulling flow away from this region and stagnating along Plane C. This will be investigated further later in

this chapter with the help of the computational result as no hard conclusion can be drawn from Figure 4.

The turbulence intensity in Planes A and B is shown in Figure 4-8. These show that the areas of high turbulence intensity appear in similar areas to those of reduced normalized velocity (high velocity deficit), specifically close behind the body. In Plane B, the closest to the wake-generating model, the turbulence intensity reached a maximum of 45% and was confined to the lower region directly behind the diffuser and the wake-generator's body (Figure 4-8b). Further downstream (Plane A) the turbulence intensity has decreased to a few small areas of 30% and with the high turbulence region seen in Plane B morphing into a bigger area of lower turbulence intensity, with a value of 25% (Figure 4-8a). In both Plane A and B the turbulence intensity of the tip vortices are similar with a value of 20%, although in plane A, the furthest from the wake generating body, the size of the tip vortex turbulent region is bigger, an indication of the vortex expansion as it moves downstream.

4.2.3.2 Longitudinal Planes

The normalized longitudinal velocity in Plane C is presented in Figure 4-9. It clearly shows the presence of a region between x/c=0.912 and x/c=2.920 of low normalized velocity (u/U=0.2) that appears to be pulled upwards from below the lowest measurement point. As the flow travels downstream the normalized velocity of this region gradually increases, but remains below the freestream velocity as it reaches the end of the measurement plane. This region was mentioned beforehand, in section 4.2.3.1, when analysing the transversal planes and referred to as region 3 (Figure 4-7b). The results shown in Figure 4-9 add further evidence to the suggestion that it is the upwash from the wake-generating model's diffuser and rear wing that cause this region.

Also evident in Figure 4-9 is the presence of two wake regions, one generated by the main body of the wake-generator, as expected, and another by the rear wing. In both cases the plot shows evidence of a separated flow, although this would not be expected on the rear wing. In Section 4.3 the rear wing's separated flow will be analysed with the use of the computational results.

Although the measurement area taken in Plane C is equivalent to 0.5 car lengths horizontally and 1.75 car heights vertically the wake is clearly still growing at the most downstream point taken, indicating that the wake of the body will still influence a car much further behind.

Figure 4-10 shows the normalized longitudinal velocities in Plane D, which was the nearest to the wake-generator's rear wing endplate. In the figure downwash is evident rather than upwash for heights below z/c=1.460, which is caused by the direction of rotation of the trailing tip vortices that leads to upwash towards the mid-plane of the wake generator and downwash in the outboard direction, as will be discussed later in this chapter when analysing the computation results (section 4-3). Also visible in Figure 4-10 is a path at a height of z/c≈1.460 that starts as two almost parallel lines that start diverging downstream (x/c=2.007), that due to its vertical position is thought to be the rear wing tip vortex path. This path shows that the vortex stays in the same vertical position as it travels downstream, while the widening of the path at x/c≈2.007 is an indication of instabilities in the vortex, as described by Zhang et al. (2002), as it begins to breakdown.

Shown in Figure 4-11, is the normalized longitudinal velocity behind the rear wheel in Plane E. The wake in this plane is significantly smaller than in Planes C and D, primarily due to the geometry of the body and the lack of components in this region. The shape of the wake is caused by the airflow being accelerated around the wheel and separating at the top, leaving a low-energy region with downwash behind it. As explained previously the wheel was located on the fixed ground upstream of the rolling road and was stationary. This affected the wake behind the wheel as the rotation would have moved the separation point forward on the wheel giving a larger wake downstream.

4.3 Computational Results

Although LDA results were important for understanding the primary characteristics of the flow field behind the upstream body, the use of CFD allowed a further insight due to the two-dimensional limitation of the experimental set up.

The in-plane flow vectors and normalized longitudinal velocity in Plane B are presented in Figure 4-12. The characteristics of the flow field were the same as those discussed in Section 4.2.3; although the wake shape is almost identical there is a slight difference in the central region. The new piece of information is the flow direction being indicated by vectors. Although the influence of the trailing vortices was discussed in the previous section there was no evidence presented. In Figure 4-12 it is visible that the tip vortices induce upwash at the mid-span of the wake-generating body. The vortex core originating from the rear wing tips are enhanced by the diffuser upwash, and to a lesser extent the downwash flow from the wheels, generating two counter-rotating vortices that dominate the wake. The centre of the flow field is dominated by upwash that then moves outboard and rotates about the main vortex core located in proximity to the rear wing tip (y/c=0.876, z/c=1.618) to induce downwash at the outboard side. As the flow travels downstream its rotation will have an effect on the trailing wing's performance by altering the flow incidence along the span of the wing, which will lead to localized downforce changes. Presented in Figure 4-13 are the CFD-predicted flow incidence at Plane A (trailing wing's leading edge). From the results it is evident that at in the central region of the wing's operation range ($-0.4<y/c<0.4$) the flow incidence is positive, indicating a vertical flow in the upward direction, with values between a minimum of 12° and a maximum of 26°. Moving away from the central region the flow incidence becomes negative reaching a minimum of -6° in the trailing wing's operating range. This indicates that the flow is in the downward direction and that the wing's angle of attack is increased, leading to an increase in downforce on the outer section of the wing.

From Figure 4-12 it is also evident from the vectors that in Plane B at low heights ($z/c<0.365$) the flow is stagnating due to the significant change of flow direction encountered at the symmetry plane, as seen in the figure.

Although the LDA results had shown the presence of a wake region, similar to that of a separated flow from a wing, just downstream of the wake-generating model's rear wing, the computational study showed a similar region and allowed

the validation of the existence of a separated flow from the rear wing, as seen in Figure 4-14. Subsequently a quick test using a tuft wand in the wind tunnel proved that the wing flap was stalled. The separated flow greatly reduced the downforce being generated by the wing and in turn reduced the amount of upwash being generated, consequently affecting the diffuser performance. This situation was detected after all the experiments had been carried out and no attempt was made to correct it as it was not feasible to repeat the experiments.

4.4 Discussion

Comparing the experimental results with those of Wilson (2008) shows similarities in the flow structures and turbulence levels, despite the geometries not being identical. Whilst in the present study the experimental data obtained at half-car-length separation (Plane B) for maximum normalised longitudinal velocity (Figure 4-7) and maximum turbulence intensity (Figure 4-8) were u/U=0.3 and I=50% respectively, in Wilson's case the results were slightly higher with u/U=0.4 and I=45% for longitudinal velocity (Figure 4-15) and turbulence intensity (Figure 4-16) respectively. Comparing the vector field (Figure 4-12) with that of Wilson (Figure 4-17) also presents similarities with the flow at half-car-length, in both cases, being dominated by two counter-rotating vortices, originating from the rear wing tips, that induce upwash at the mid-span of the wake-generating model. As Wilson's work had satisfactory correlation with the wake of a complete Formula 1 scaled model and the results obtained in the present work, with the wake-generating model, have satisfactory correlation with Wilson's work it gave confidence that the results obtained, in terms of velocity trends, in the present work were representative of a complete car wake.

Despite the present model not being identical to the bluff bodies studied by Morel (1978) and Ahmed et al. (1984) if we consider the model used in this study as an inverted version of the aforementioned authors' models some similarities can be found. The model used in this study has a diffuser which can be considered as the inverted slant, used in Morel and Ahmed's work, generating upwash instead of downwash. Similarly a region of separated flow is found behind the model used in the current study which is caused by the rear of

the model being a vertical plate. Although the diffuser from this study's model is comparable with the slant from previous works the presence of endplates on the diffuser limits the formation of edge vortices, along the diffuser longitudinal edge, which are replaced by counter-rotating tip vortices generated by the rear wing that induce upwash along the central plane of the model.

Due to equipment malfunctioning it was not possible to acquire all the flow-field information required for this project, hence a computational study was carried out using the data obtained with the LDA to validate the computational approach. Despite the computational simulations over- and under-estimating the horizontal and vertical velocities, and turbulence intensity in certain regions of the flow, it managed to predict the flow field trends seen in the experimental results with acceptable errors in the region where the trailing-wing operates. Having obtained satisfactory correlation with the experimental data, it gave confidence in the computational method and results allowing the use of these to extract further information that was not possible from the LDA data.

In this study three main flow characteristics were identified: low dynamic pressure in the wake, counter-rotating vortices that lead to local velocity components and high turbulence intensities in the wake. Although these can be listed separately their interaction is what makes the wake unique.

Although a low-dynamic-pressure region was expected behind the wake generator the interaction of the tip vortices, from the opposite wing tips, led to an increase in this low-dynamic-pressure region due to the counter-rotating vortices stagnating at the mid-plane, downstream of the model, as they rotate into each other. This in conjunction with the upwash from the underbody and wing led to a low dynamic pressure region present downstream of the wake-generator starting at x/c=0.912.

The results highlight the complex environment that a trailing vehicle will have to operate in. Although the lower dynamic pressure can be seen to give an improvement in performance due to the reduction of drag in the trailing vehicle, this pressure reduction associated with the varying flow incidence leads to potential loss in downforce that limits the cornering performance of the trailing

vehicle. On the other hand the varying flow incidence can also be seen as having the potential of enhancing the performance of a trailing wing as, depending on the incidence, it will increase the angle of attack of the trailing wing. This increase in angle of attack leads to an increase in downforce that may reduce the load losses a wing endures whilst operating in the wake.

Although the low dynamic pressure can be viewed as detrimental to the trailing vehicle's performance, the turbulence intensity increase can be viewed potentially as positive as it may delay boundary layer separation on the trailing monoposto's front wing. This delay in separation may allow the trailing vehicle to use a wing at a greater angle of attack recovering part of the performance lost through the other mechanisms.

4.5 Conclusion

A wake-generating model similar to that presented by Wilson (2008) was tested with the intent of understanding the effect of its wake on a trailing wing. Experimental and computational data were acquired in an attempt to identify the flow features and explain the influence they have on the front wing of a trailing car.

The main flow features identified in the wake of the wake-generator are similar to those described by other authors and will play a significant part in the performance of not only a wing but an entire vehicle trailing immersed in the wake.

The analysis carried out on the flow behind the wake-generating model has demonstrated the complexity of this wake, which is intended to be representative of that produced by a monoposto race car. We are now in a position to investigate the effect of this wake on a trailing wing, which will be discussed in the next chapter.

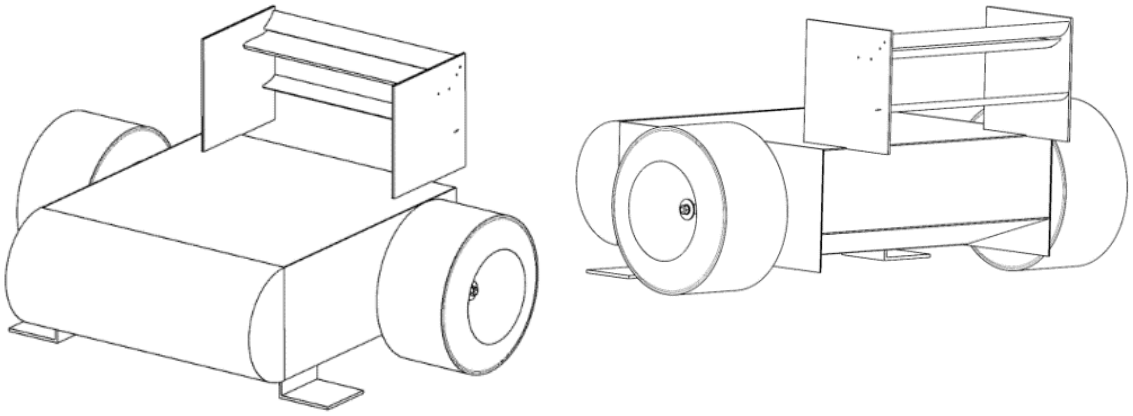

a) b)

Figure 4-1: Schematic of upstream body: a) front-quarter view; b) rear-quarter view

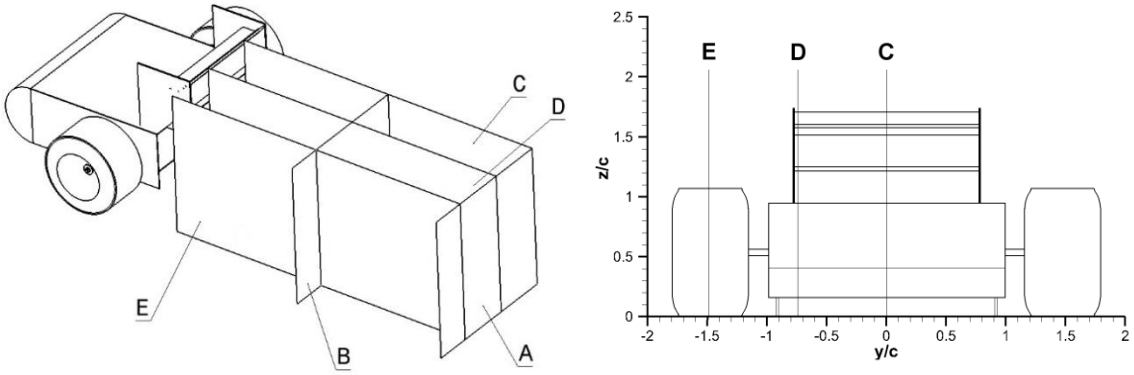

a) b)

Figure 4-2: Schematic of LDA measurement planes behind wake generator: a) isometric view of planes; b) position of longitudinal planes relative to wake generator

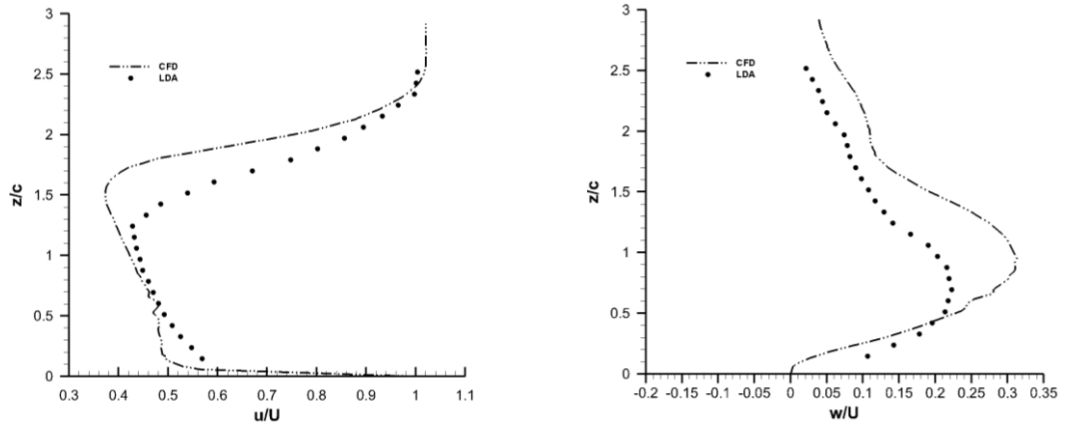

a)

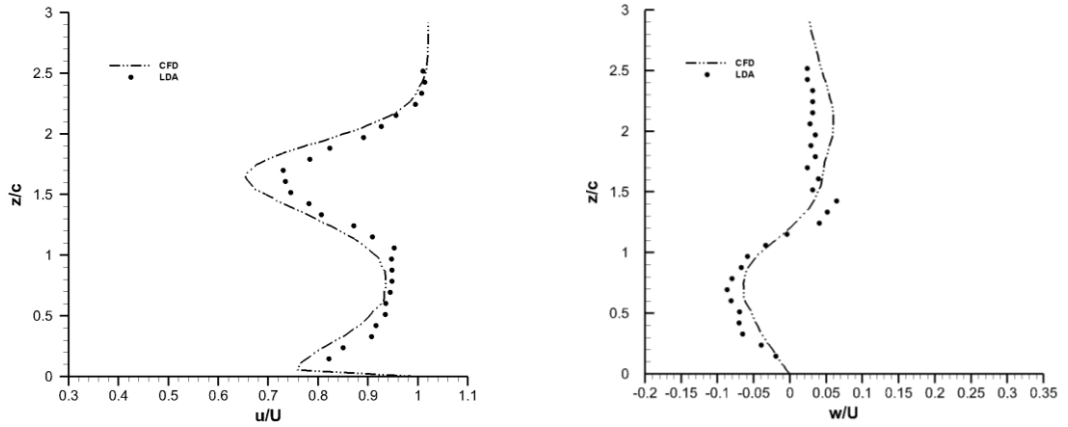

b)

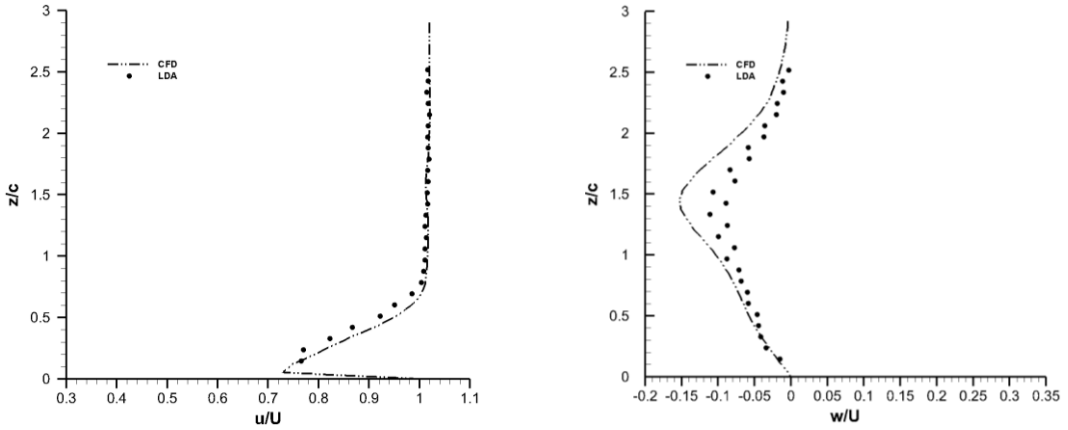

c)

Figure 4-3 - Normalised longitudinal (left) and vertical (right) velocity profiles at the trailing-wing leading edge (Plane A): a) centreline y=0 (Plane C), b) mid-semi-span y/c=0.744 (Plane D) and c) wing tip y/c=1.488 (Plane E). δ_{LDA}<1%

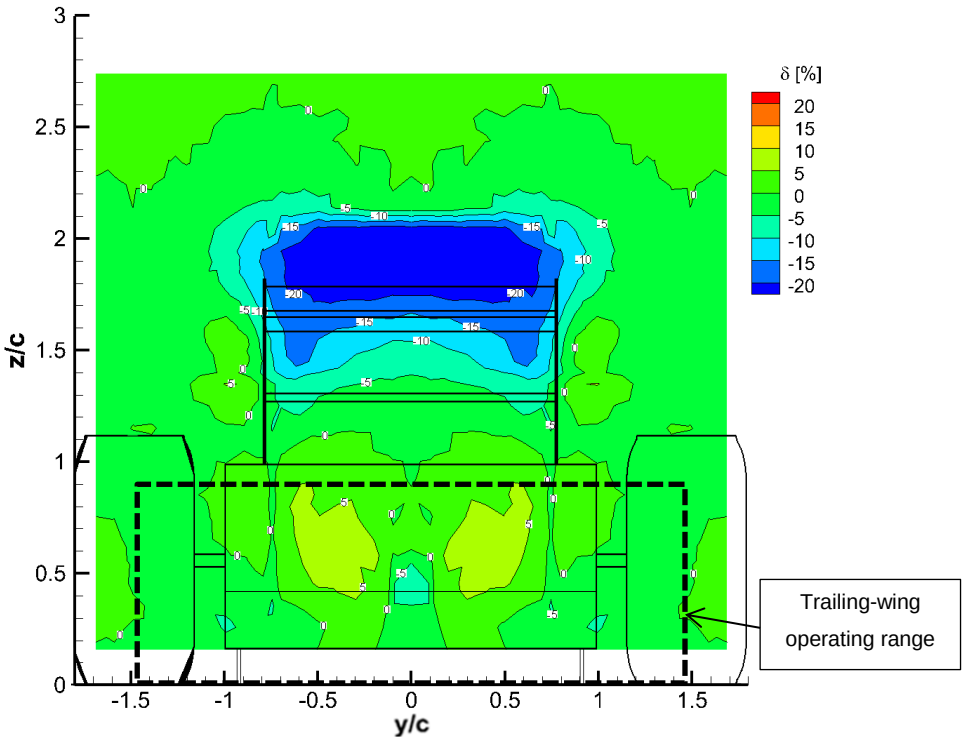

Figure 4-4: Relative error between CFD-predicted and LDA-measured longitudinal velocity (u) normalized by measured u_{max} at Plane A

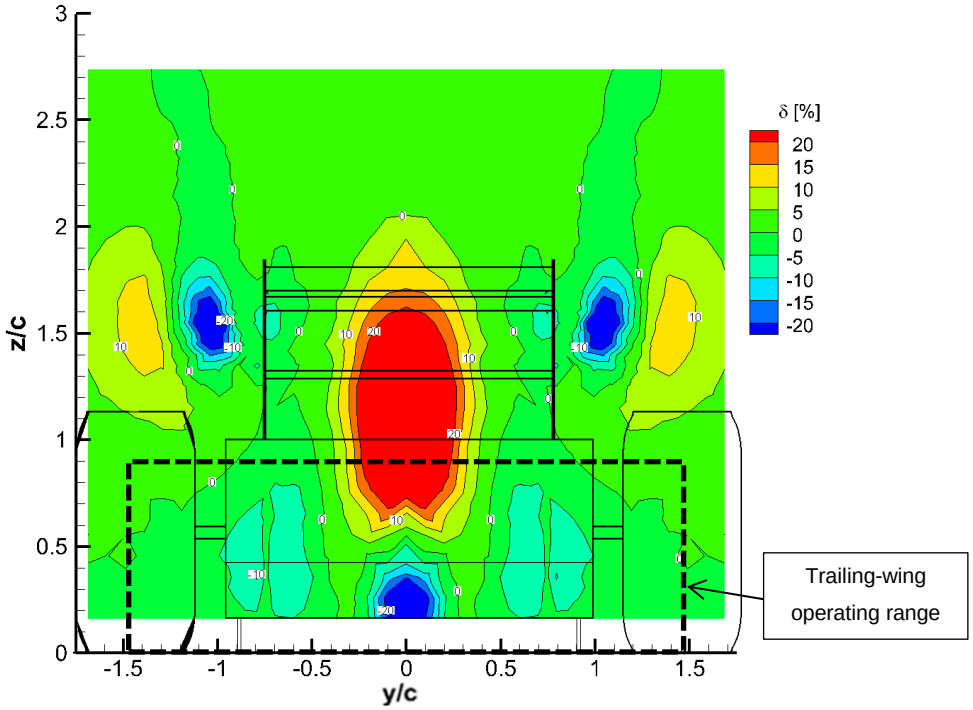

Figure 4-5: Relative error between CFD-predicted and LDA-measured vertical velocity (w) normalized by measured w_{max} at Plane A

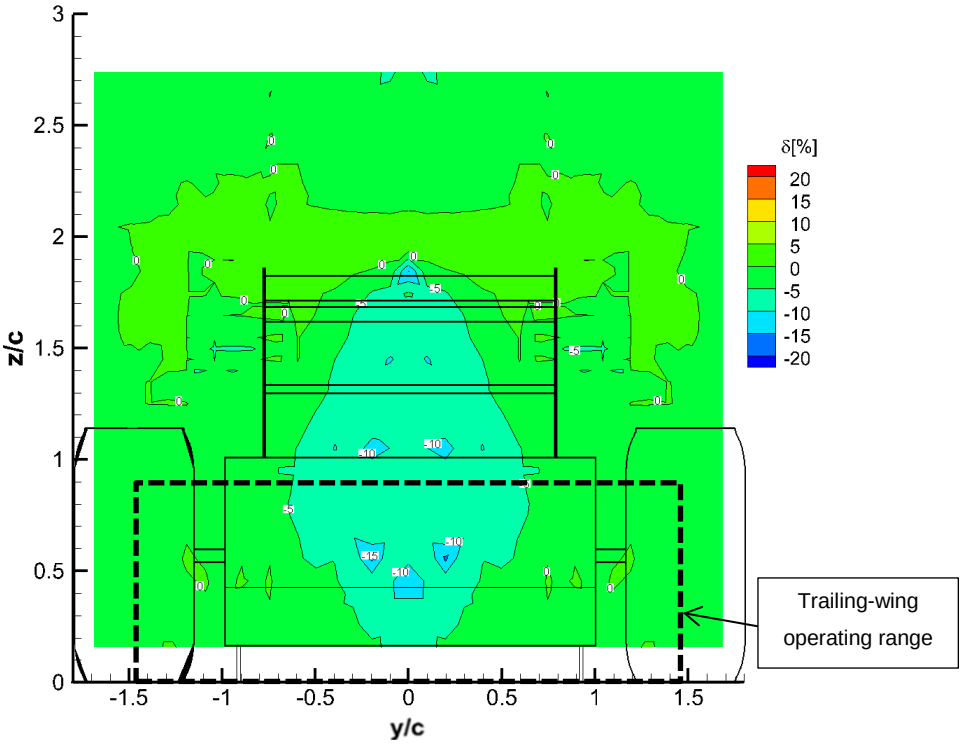

Figure 4-6: Relative error between CFD-predicted and LDA-measured turbulence intensity (I) normalized by measured I_{max} at Plane A

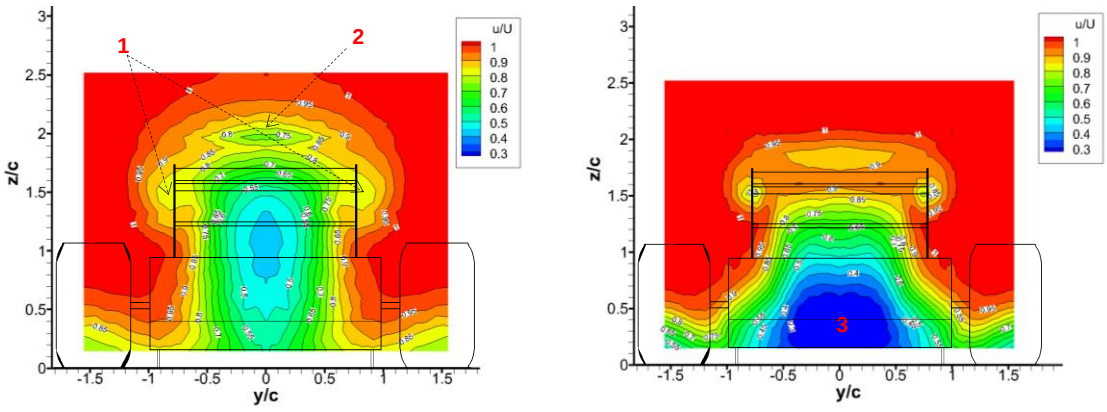

a) b)

Figure 4-7: LDA-measured normalised longitudinal velocity (u/U) in a) transversal Plane A and b) Plane B. δ_{LDA}<1%

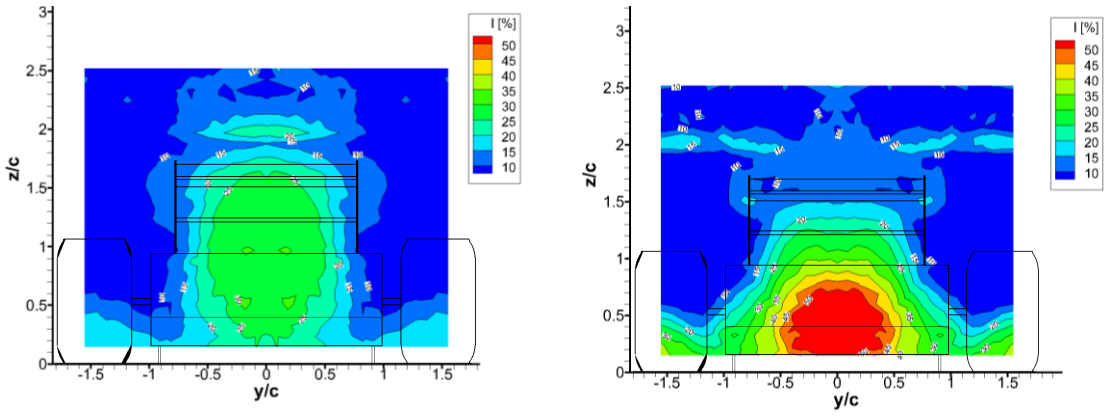

Figure 4-8: LDA-measured Turbulence intensity (I) in a) transversal Plane A and b) Plane B. δ_{LDA}<1%

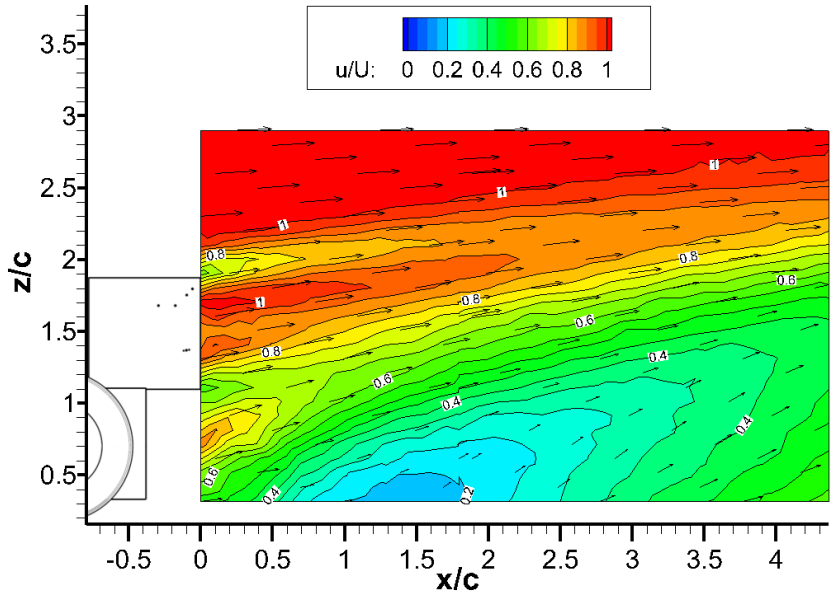

Figure 4-9: LDA-measured normalized longitudinal velocity (u/U) in Plane C. δ_{LDA}<1%

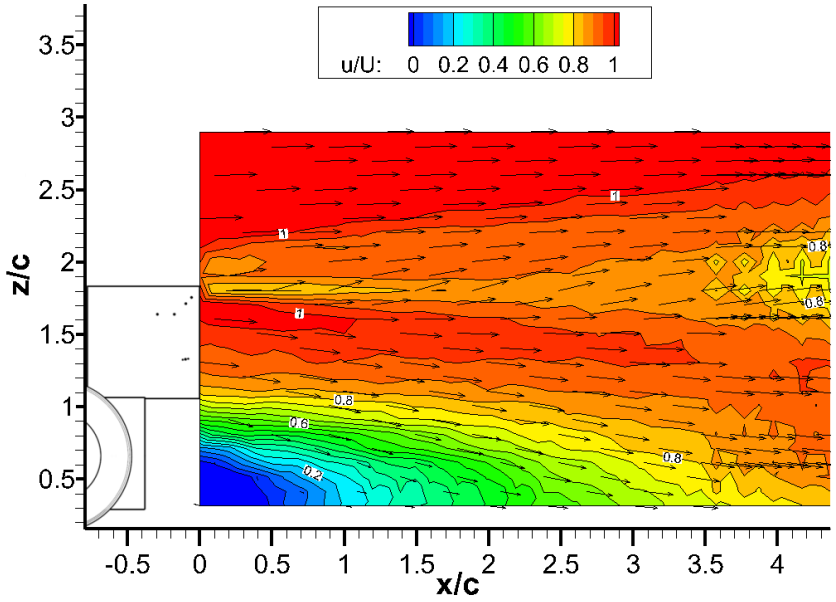

Figure 4-10: LDA-measured normalized longitudinal velocity (u/U) in Plane D.

δ_{LDA}<1%

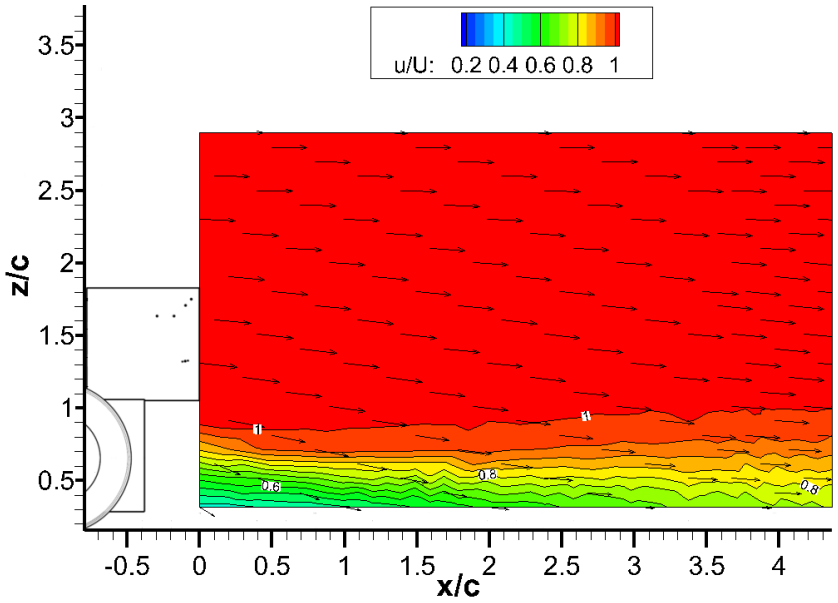

Figure 4-11: LDA-measured normalized longitudinal velocity (u/U) in Plane E.

δ_{LDA}<1%

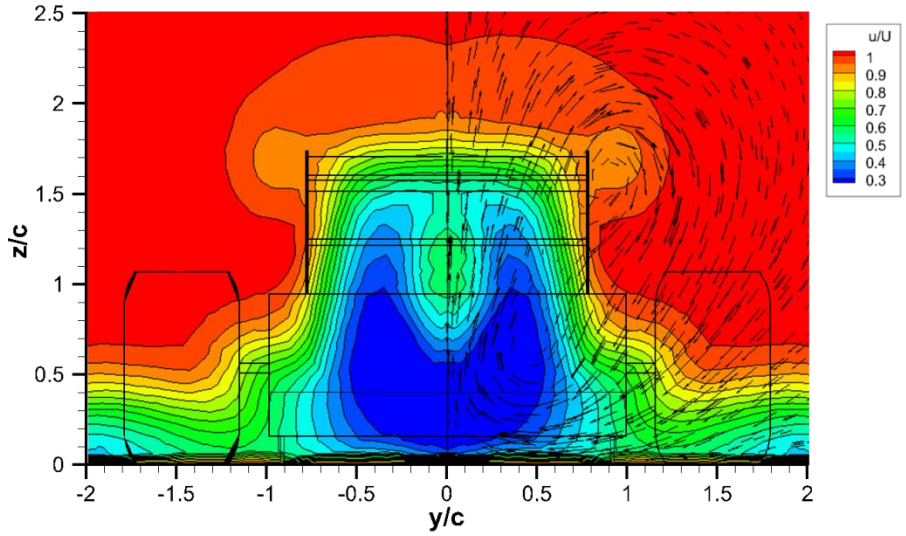

Figure 4-12: CFD- predicted normalised longitudinal velocity (u/U) at Plane B

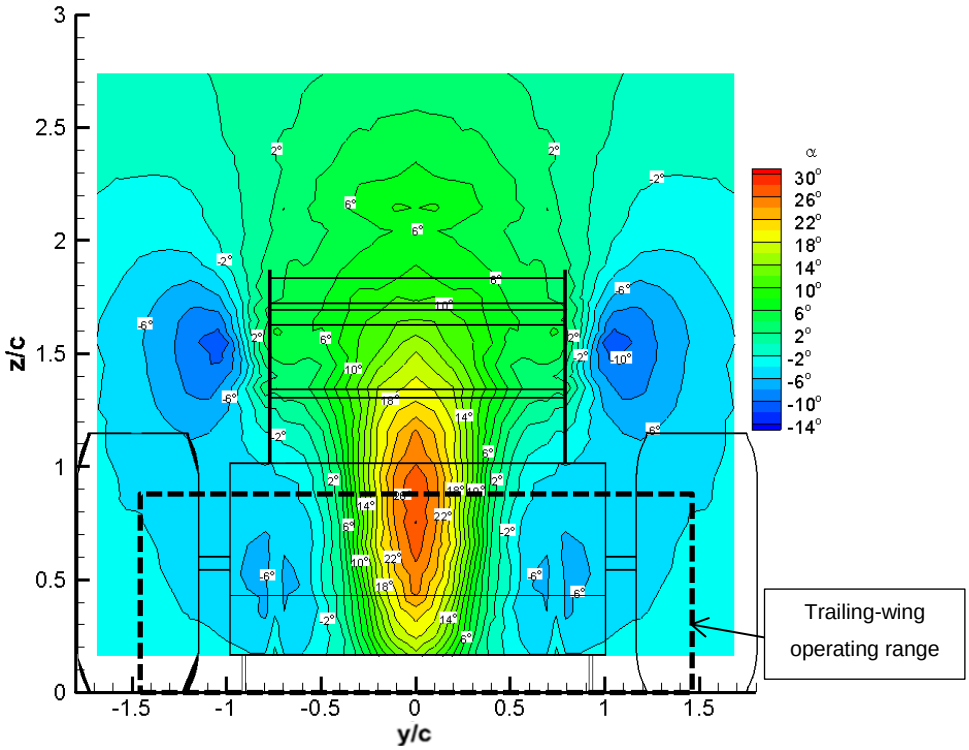

Figure 4-13: CFD-predicted flow incidence angle (α) at Plane A; positive values indicate vertical flow in upward direction.

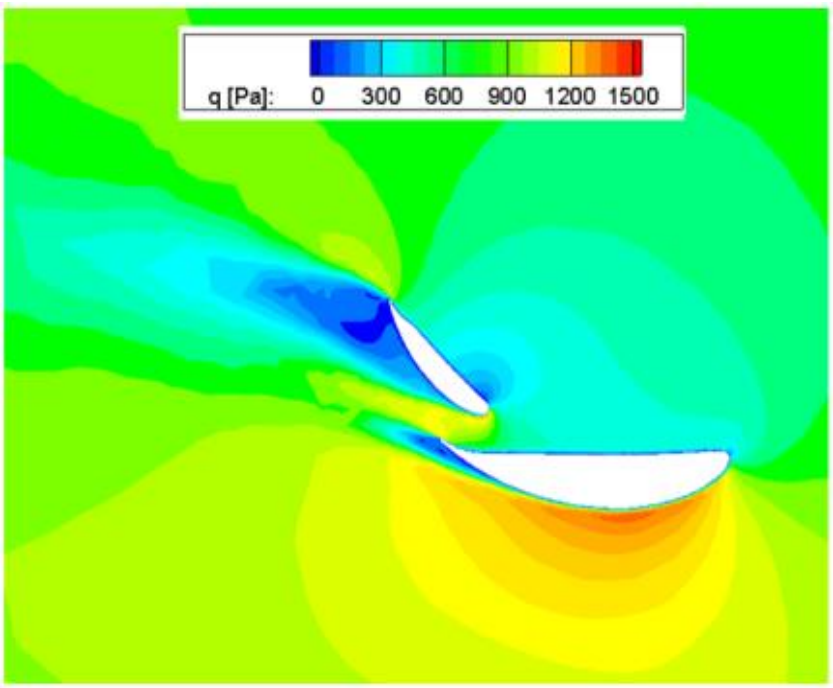

Figure 4-14: Dynamic pressure around rear wing centreline from CFD (flow from right to left)

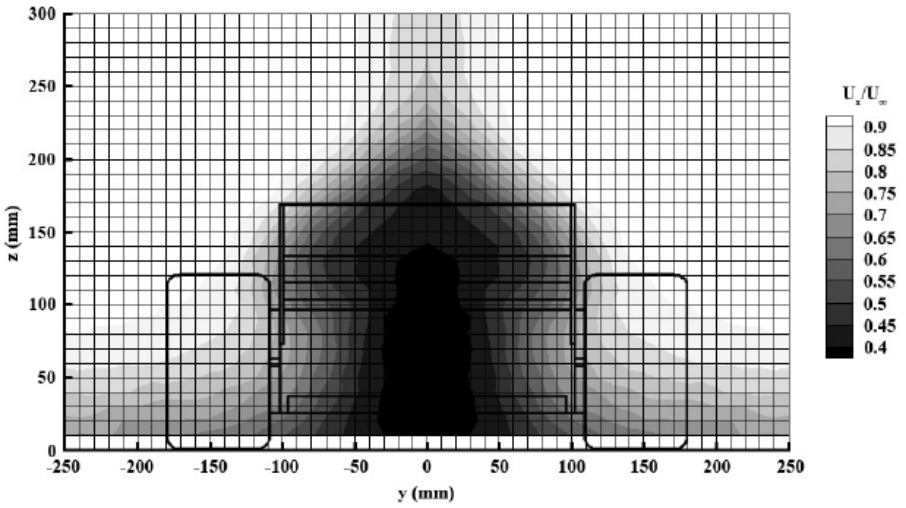

Figure 4-15 Contour of normalized axial velocity at half-car length downstream of wake-generating model. Plot extracted from Wilson et al. (2008)

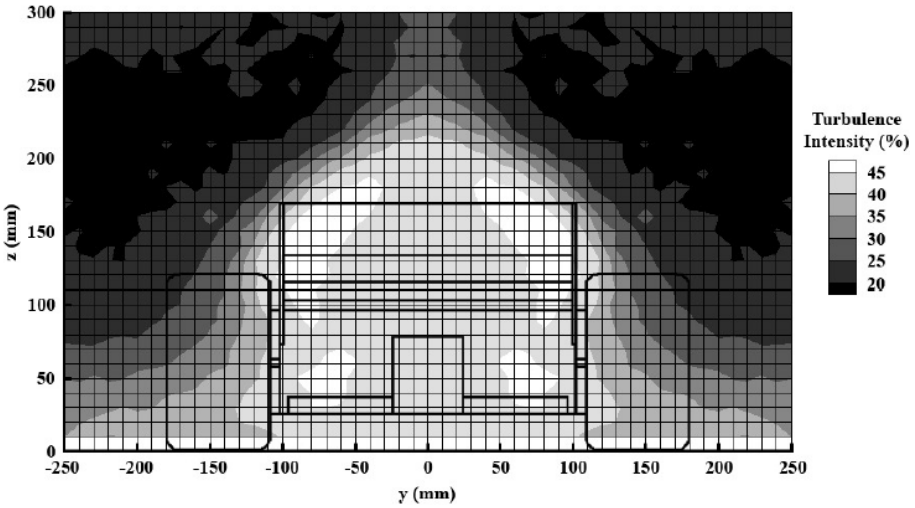

Figure 4-16 Contour of turbulence intensity at half-car length downstream of wake-generating model. Plot extracted from Wilson et al. (2008)

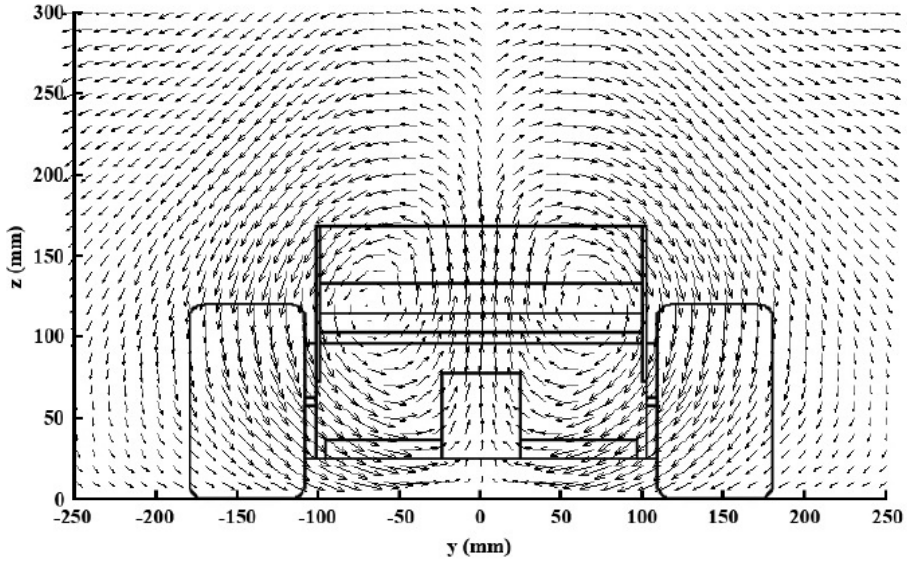

Figure 4-17 X and Y velocity vectors at half-car length downstream of wake-generating model. Plot extracted from Wilson et al. (2008)

5 Wing Operating in a Disturbed Flow

In this chapter the results for the wing operating in the disturbed flow, i.e., immersed in the wake of the wake generator, will be presented and discussed. Force measurements, surface flow visualization and computational simulations will be used to understand the performance changes the wing experiences when travelling in the wake of a leading monoposto car.

As in Chapter 3 the wing was tested at two difference flap configurations, low and high, but only results for the wing at zero degrees of yaw and roll will be presented as the objective of this work was to study the influence of individual external disturbances on the performance of an inverted wing in ground effect.

5.1 Force Measurements

5.1.1 High Flap Angle – 23.9º

The downforce coefficient (C_L), downforce coefficient slope ($dC_L/d(h/c)$), drag coefficient (C_D) and lift-to-drag ratio (L/D) results at different ride heights are presented in Figure 5-1, Figure 5-2, Figure 5-3 and Figure 5-4 respectively.

Figure 5-1 shows the downforce coefficient variation with ride height and the percentage change in downforce from the undisturbed case. As the wing is lowered from its maximum ride height of h/c=0.893 the downforce coefficient increases monotonically, from an initial value of C_L=0.833, until reaching its lowest ride height of h/c=0.060 with a value of C_L=1.245. Although the wing's downforce coefficient increases as the wing is lowered towards the ground these values are significantly lower than those noted when the wing operated in the undisturbed flow. Even at the highest ride height analysed in this study the wing starts its descent with a downforce coefficient 29.7% lower than in the undisturbed case. As the wing is lowered the percentage of downforce lost increases until reaching a ride height of h/c=0.159 at which point the downforce loss reaches 42.1%. Between the ride heights of h/c=0.159 and h/c=0.089 the percentage of downforce lost stabilizes. Further reduction in ride height leads to

a drop in the percentage of downforce lost, reaching the ride height of h/c=0.060 with a loss of 40%.

In Figure 5-2 the results for downforce coefficient slope at different ride heights are presented. Although the analysis of this plot was of importance for the wing in the undisturbed flow as it facilitated the identification of changes to the way the wing generated downforce, once the wing is immersed in the wake the analysis becomes more difficult, due to the differences in the oncoming flow encountered in the wake at different ride heights. Although the four force enhancement/reduction mechanisms that were identified in Sections 3.2.1.1 and 3.2.1.2 may still be present the current test configuration did not allow for the development of an accurate technique that would facilitate their identification.

The variation of drag coefficient with ride height is presented in Figure 5-3. As the wing is lowered from its highest ride height of h/c=0.893 the drag coefficient initially drops slightly from a starting value of C_D=0.120 to C_D=0.118 at a ride height of h/c=0.476. As the ride height is further reduced the drag coefficient increases until reaching a value C_D=0.140 at a ride height of h/c=0.129. Below this ride height the drag coefficient remains almost unchanged until the wing reaches the minimum ride height of h/c=0.060. Also noted is that as the ride height is reduced the decrease in drag generally increases. It starts with a 16.6% reduction at the initial ride height of h/c=0.893 and gradually increases until reaching its maximum value of 40.1% at the ride height of h/c=0.060, the lowest ride height in this study.

The downforce-to-drag ratio (L/D) results are presented in Figure 5-4 against ride height, for both disturbed and undisturbed flow. The results show that in the disturbed conditions as the wing's ride height is reduced from the maximum ride height of h/c=0.893 to the minimum ride height of h/c=0.060 L/D increases monotonically from a value of 6.928 to a maximum value of 8.864. In the case of the disturbed condition L/D increases by ΔL/D=1.936 compared to an increase of only ΔL/D=0.494 for the wing in the undisturbed conditions, giving the wing operating in the disturbed conditions a steeper L/D slope, a situation

caused by the trailing-wing operating in regions of the wake with different flow characteristics at each ride height. The results also show that the wing's L/D, with the exception of the ride height of h/c=0.060, is lower than that of the wing in the undisturbed case throughout the ride height range.

5.1.2 Low Flap Angle – 13.8º

The results for variation of downforce coefficient with ride height are presented in Figure 5-1. As the wing is lowered from its maximum ride height of h/c=0.893 the downforce coefficient increases monotonically, from an initial value of C_L=0.488, until reaching its lowest ride height of h/c=0.060 with a value of C_L=0.945. Although the wing's downforce coefficient almost doubles between the highest and lowest ride heights the values are significantly lower than those measured when the wing operates in an undisturbed flow. At the greatest ride height analysed in this study the wing starts its descent with a downforce coefficient 32.8% lower than in the undisturbed case. As the wing is lowered the percentage of downforce lost increases until reaching a ride height of h/c=0.109 at which point the downforce loss reaches 42.0%. As the wing's ride height is further reduced the downforce loss decreases reaching a value of 38.2% at a ride height of h/c=0.060.

Similarly to the "high-flap-angle" case the downforce coefficient slope presented in Figure 5-2 does not provide any information that could be considered of importance to the understanding of the different force enhancement/reduction mechanisms of the wing. Although it does not give any clear indication of where the mechanisms occur it does highlight the fact that the low-flap-angle case has a greater rate of downforce increase at ride heights below h/c=0.159.

The variation of drag coefficient with ride height is presented in Figure 5-3. As the wing is lowered from its highest ride height of h/c=0.893 the drag coefficient initially drops slightly from a starting value of C_D=0.047 to C_D=0.044 at a ride height of h/c=0.476. As the ride height is further reduced the drag coefficient increases monotonically until reaching its maximum value of C_D=0.140 at a ride height of h/c=0.060, the lowest ride height analysed in this study. Similarly to the high-flap configuration the drag reduction percentage generally increases

throughout the ride height range analysed, apart from a dip around h/c=0.099. It starts with a drag reduction of 16.9% at a ride height of h/c=0.893 and increases to 48.2% at a ride height of h/c=0.060.

The downforce-to-drag ratio (L/D) results are presented in Figure 5-4 for the low flap angle. As the wing's ride height is reduced from the maximum ride height of h/c=0.893 L/D increases monotonically from a value of 10.314 to 12.571 at a ride height of h/c=0.198. At h/c=0.188 L/D suffers a small drop to 12.551 and then continues increasing monotonically until reaching its maximum value of L/D=13.432 at a ride height of h/c=0.060. In the case of the disturbed condition L/D increases by ΔL/D=3.118, compared to a decrease of ΔL/D=1.557 for the wing in the undisturbed conditions, giving the wing operating in the disturbed conditions a steeper L/D slope. The results also show the lower flap setting wing when operating at lower ride heights (h/c<0.129) has a higher efficiency than that seen in the undisturbed case. Contrary to the results seen for both flap settings in the undisturbed flow, in the disturbed flow L/D on both flap settings increases monotonically throughout the ride height range with both settings showing a similar efficiency increase, between the highest and lowest ride height, with an increase of 24.8% and 27.9% for the low and high setting respectively.

5.2 Surface Flow Visualization

Surface flow visualization was carried out at the same ride heights as in the undisturbed case. Analysis of the surface flow results in the disturbed flow showed that the turbulent wake, upstream of the wing, led to similarities in the streaklines on the wing surface at different ride heights and flap settings. Due to the similarities noted only the high flap setting results will be presented.

In Figure 5-5 the streaklines on the suction surface of the wing for the high flap setting at ride heights of h/c=0.089 and h/c=0.060 are presented, next to the respective CFD-predicted streaklines. These ride heights were the same as the two lowest ride height cases presented in the undisturbed flow and were selected for the undisturbed conditions based on their position in the force-enhancement and force-reduction regions the wing operated in. In the case of

the disturbed flow both wings operated in the force- enhancement region and only minor differences were noted in the results.

Analysis of the images shows the absence of the spanwise separation bubble, which was present in the undisturbed flow case. Despite not being as pronounced as in the case of the undisturbed flow, the outboard tip vortices (labelled as 1) are still present and the tip-vortex widening, seen in the undisturbed conditions, (Section 3.2.2) is also visible when the wing is lowered from a ride height of h/c=0.089 to h/c=0.060.

Although there are significant differences in the surface flow results when compared with the undisturbed case, the separation present at the trailing edge (labelled as 2) of the main element and the curved flow from the flap's leading edge to its inboard tip (labelled as 3) indicates that not all features present in the undisturbed case have disappeared.

Analysis of the CFD-predicted streaklines presents similarities to the experimental results, with the exception of the separation seen on the wing's mainplane (labelled as 4) which is significantly bigger in the computational results. This is likely to be caused by the incorrect CFD-predicted velocity at the wing's mid-span, where both u/U and w/U were lower than those seen in the wind tunnel, leading to a greater local incidence and consequent steeper pressure recovery.

5.3 Computational Results

5.3.1 Pressure Distribution

The computational chordwise pressure distribution variation with ride height on the main plane at mid-span, main plane and flap at mid-flap span and for the main plane and flap wing at the outboard tips are shown in Figure 5-6, Figure 5-7 and Figure 5-8 respectively. Although a very fine mesh was used on the wing surfaces the results show some oscillations, particularly on the main plane suction surface, these are attributed to facetted geometry on this element and were also present on the results in Chapter 3.

The results for the main plane at mid-span (Figure 5-6) show that as the wing's ride height is reduced the pressure distribution at the leading edge of the wing's suction surface changes shape and the peak suction moves aft, a trend also noted for the wing in the undisturbed flow. At the greatest ride height of h/c=0.179 the pressure decreases quickly for x/c<0.03, reaching its peak negative pressure of C_p≈-0.4 representing a decrease of 85% when compared to the undisturbed case. Following the pressure peak there is a small rise in pressure before a more gradual increase until x/c=0.35. After this point the pressure increases at a greater rate until reaching the trailing edge of the wing. For h/c=0.060 and h/c=0.089 the pressure decrease is more gradual with both cases reaching their negative pressure peak at x/c≈0.20, with a pressure coefficient of C_p≈-1 and C_p≈-0.8 respectively representing a drop of approximately 75% for both cases compared with the undisturbed cases. Behind the pressure peak the pressure gradually increases towards the trailing edge, for h/c=0.089, whilst for h/c=0.069 there is an initial increase at a greater rate until x/c≈0.3 followed by a more gradual increase at a lower rate.

The results for the pressure distribution around the main plane and flap (Figure 5-7) at the mid-flap plane show a trend similar to the previous case, i.e., as the ride height is reduced the initial suction decrease is more gradual and the suction peak moves aft on the main plane. At the greatest ride height of h/c=0.179 the pressure decreases reaching a peak suction of C_p≈-1.5 at x/c≈0.03, a value 47% lower than in the undisturbed case. After the suction peak a small pressure increase is noted, followed by a plateau between x/c≈0.07 and x/c≈0.30 with C_p≈-1.4. Behind x/c≈0.30 the pressure increases gradually until x/c≈0.47, a point already on the flap, where a slight drop in pressure is noted before it starts a gradual increase until the trailing edge of the flap. For h/c=0.060 and h/c=0.089 the initial pressure decrease is more progressive, similar to that noted on the semi-span of the main plane. The pressure gradually decreases in both cases until reaching the pressure peak at x/c≈0.22, with a value of C_p≈-2.1 for h/c=0.060 and C_p≈-1.6 for h/c=0.089, representing a decrease of about 60% from the undisturbed case. Behind the suction peak the case with the lowest C_p (h/c=0.060) sees pressure rise at a

higher rate than for h/c=0.089, until x/c≈0.40. Behind this position both pressure contours match almost perfectly and pressure gradually increases until the trailing edge of the wing.

The chordwise pressure distribution results at the wing tip (Figure 5-8) show that, similarly to the main plane and flap mid-spans, the results for h/c=0.179 show an initial pressure drop peaking at x/c≈0.03, followed by an increase in pressure. In this case after the initial pressure increase it starts decreasing and reaches a negative peak of C_p=-2 at x/c≈0.50 a results that is only 17% lower than in the undisturbed case and almost double the pressure obtained by the h/c=0.060 and h/c=0.089 cases. Following the suction peak the pressure gradually increases until reaching the trailing edge of the wing. For both h/c=0.060 and h/c=0.089 the pressure contours show a gradual decrease in pressure until reaching x/c≈0.35, with peak values of C_p=-1.2 and C_p=-1.1 respectively, which are about 65% lower than those obtained in the undisturbed case. Behind the pressure peak the pressure for h/c=0.060 increases at an initially greater rate than was the case h/c=0.089. Downstream of x/c≈0.65 both cases present similar results and gradually increase their pressure until reaching the trailing edge of the wing.

From the results in Figure 5-6, Figure 5-7 and Figure 5-8 it is possible to obtain a comparison of the load that each wing section has at each ride height. This is presented in Figure 5-9 as a bar graph. As with the results presented in Section 3.2.3.2 for the undisturbed the results have been normalized using the loading seen at flap mid-span at a ride height of h/c=0.060 from the undisturbed case, as this was the highest load seen in the data set. The results show that at a ride height of h/c=0.179 the wing mid-span, flap mid-span and wing tip have a loading of 14.2%, 62.2% and 65.1% of the wing's maximum sectional loading respectively. Comparing these results with those from the undisturbed cases it is evident that the wing and flap mid-spans suffer a reduction in loading of 10.4% and 19.7% in the disturbed conditions, whilst the tip has 16% higher loading than in the undisturbed case. As the wing is lowered from a h/c=0.179 to h/c=0.089 the loading at the wing mid-span increases by 0.9%, to 15.1% of

the maximum loading, whilst at the flap mid-span and wing tip the loading decreases by 5.1% (to 57.1% of maximum) and 16.3% (to 48.8% of maximum) respectively. With a further reduction of ride height, from h/c=0.089 to h/c=0.060, the section loading increases by 0.5% at the wing mid-span, reaching a loading of 15.6% of the maximum value, while the flap mid-span loading increases 2.1%, reaching of 59.2% of the maximum sectional loading. Contrary to the other spanwise sections the wing tip suffered a reduction in loading of 3.7% with the final ride height reduction, giving it a final loading of 45.1% of the maximum sectional loading seen by the wing.

Analysis of the wing's pressure distribution at the three spanwise sections leads to the data obtained being limited and potentially clouding other phenomena occurring at other spanwise locations that are not seen with the three sections. In Figure 5-10 the suction surface pressure distribution is compared for the high flap setting in undisturbed and disturbed flow conditions, at a ride height of h/c=0.089. Analysis of the contour plot shows that the mid-flap span measurement plane (highlighted with a dashed line) only captures a small tip of a bigger region of low pressure (labelled as 1). The contour plot also shows how the suction generated by the inboard tip vortices on the flaps is reduced when the wing is immersed in the wake, information that was not possible to obtain from the aforementioned sectional loading. The outboard tip vortices, seen on the endplates (labelled as 2), also show a reduction in the vortex-induced suction when the wing is in the disturbed case.

Returning to the chordwise pressure distribution plots (Figure 5-6, Figure 5-7 and Figure 5-8) it is possible to identify two distinct pressure distribution behaviours on the pressure surface of the wing, which can aid understanding of how the boundary layer is behaving on the suction surface of the wing. The first consists of a rapid pressure decrease, on the pressure surface, which indicates the presence of a separated boundary layer at the trailing edge of the suction surface, and a second where the pressure maintains a fairly constant slope, which is an indication of an attached boundary layer on the suction surface. Despite the CFD-predicted surface flow (Figure 5-5) only showing a single

region of separation, at the trailing edge of the wing's main element (labelled 4 in Figure 5-5), analysis of the CFD-predicted wall shear stress (Figure 5-11) and the pressure distribution plots shows that the wing is likely to be also separated at the trailing edge of the flap at mid-span and at the tip.

From Figure 5-11 it is also evident that the wing operating in the undisturbed flow operates differently to the wing operating in the disturbed flow. In the case of the wing operating in the undisturbed flow the wall shear stress (τ) reaches zero on the wing's main element and then returns to a value above zero further downstream. This is an indication that the boundary layer has separated and reattached to the wing. In the case of the wing operating in the disturbed flow the wall shear stress only reaches zero along the trailing edge of the main element, flaps and in the outboard region where the tip vortices are located. The difference between both cases can be explained by the presence of a turbulent boundary layer in the disturbed case due to the high turbulence intensity in the oncoming flow which delays separation due to the increased momentum transfer in the boundary layer. In the case of the undisturbed flow the low turbulence intensity in the oncoming flow (I=0.7%) leads to the formation of a laminar boundary layer that separates (shown by the wall shear stress reaching zero (τ=0)) due to the adverse pressure gradient and reattaches downstream (τ>0) due to the boundary layer transitioning to turbulent.

5.3.2 Wake

In Figure 5-12 and Figure 5-13 the velocity vectors and dynamic pressure contours at x/c=1 behind the wing are presented for h/c=0.060 and h/c=0.089 respectively. The contours show the presence of two counter-rotating vortices, on each side of the wing, one originating from the inboard tip of the flap and a second much weaker vortex that originated from the outboard tip. At both ride heights the vortices remain in the same location relative to the wing. Also noticeable are the similarities between the wake of both the h/c=0.060 and h/c=0.089 cases. Analysis of the data shows that at x/c=1 downstream of the wing the dynamic pressure in the wake of the h/c=0.089 case is 6.3% higher than that of h/c=0.060. The lower dynamic pressure for h/c=0.060 is a

consequence of the wing at this ride height generating more downforce and consequently having more induced drag, increasing the losses and lowering the dynamic pressure in its wake.

In Figure 5-14 and Figure 5-15 the velocity vectors and turbulence intensity contours at x/c=1 behind the wing at h/c=0.060 and h/c=0.089 are presented. As noted in the wake dynamic pressure contours the similarities between both cases is apparent, with only a small increase of 0.04% in the turbulence intensity, particularly noticeable at mid-flap and in a region outboard of the endplate and extending slightly inboard of the endplate for h/c=0.060.

In Figure 5-16 the normalized flow velocity is presented for the mid-flap plane at x/c=1. Once again, the results show a similarity between the h/c=0.060 and h/c=0.089 cases. In both cases the minimum velocity reached $u/V_\infty=0.2$ representing an 80% drop from the freestream values and a drop of 5% for h/c=0.060 and 30% for h/c=0.089 when compared to the undisturbed cases. For h/c=0.179 the deficit is lower than that experienced at the other two ride heights, with a reduction of 50% from the freestream and 30% from the undisturbed condition. The velocity gradually increases further away from the road only reaching the freestream velocity at a height above z/c=2.0, outside of Figure 5-16's range, a height that still has some influence from the upstream wake-generator's wake.

5.4 Discussion

The results from the force measurements indicate that a wing travelling in a monoposto car's wake will suffer a significant decrease in the downforce generated and also a reduction in drag, phenomena that have been identified in previous studies (Fiumara (2007), Wilson et al. (2008) and Newbon et al. (2014)). Analysis of the reduction in downforce coefficient (Figure 5-1) showed that the reductions seen in both the high and low flap angles were within 4% of each other throughout the ride height range. On the other hand, the drag coefficient plot highlighted that at the highest ride height both cases experienced the same drag reduction but as the ride height was reduced the

low-flap case experienced greater drag reductions than the high-flap case, reaching a difference between cases of up to 8.9% at h/c=0.060, the lowest ride height tested in this study. The L/D results showed that at low ride heights despite being the region where the greatest downforce loss occurs it is also the region with the highest L/D in the wake.

The pressure distribution results highlight the difficulties the trailing wing has in operating in the wake of the wake-generating model, with different sections of the wing increasing or decreasing their loading at different ride heights. From the analysis of the chordwise pressure coefficient plots the following observations can be made.

- The pressure coefficient distribution trends noticed in the undisturbed cases are still present, i.e., the aft movement of the pressure peak with ride height reduction. Although the movement of the pressure peak is also present in the disturbed case the movement is greater than in the undisturbed case, hence the pressure peak occurs further aft than on the undisturbed case.
- The flow features found in the wake (dynamic pressure, turbulence intensity and flow angle) have an influence on the magnitude of the pressure peaks and the pressure distribution around the wing. These features cause a decrease in the forces experienced by the wing as a direct consequence of the increased pressures noted on the suction surface of the wing.
- At greater ride heights the flow conditions appear to be more favourable to the trailing wing's performance although the forces are still smaller than those experienced in the undisturbed cases. This is particularly true in the tip region of the h/c=0.179 case, where the sectional loading is 16% greater than in the undisturbed case and is also greater than at lower ride heights where ground effect has a greater influence.
- Analysis of the sectional loading, despite giving an indication of the how the wing is operating, does not capture all the data, leading to quantitative differences seen between the force data, for the whole wing, and pressure data presented for the sections.

- Comparing the CFD-predicted surface streaklines with the surface flow visualization from the wind tunnel presents similarities in the flow pattern, with the exception of the regions of separation at the trailing edge of the wing's main element. These regions are greater in the CFD results and can be attributed to inherent difficulty CFD has in predicting accurately the pressure field in separated and vortical flow fields, as is the case in the wake of wake-generator.

When considering the above bullet points it is evident that the wake of the wake-generator plays an important role in the wing's performance. In order to explain the performance drop that the trailing wing experiences we need to return to Chapter 4 to obtain some conclusions.

- At the main plane mid-span the dynamic pressure is approximately 25% of the freestream dynamic pressure, for all ride heights. Whilst at the wing tip the dynamic pressure at h/c=0.060 is approximately 44% of the freestream dynamic pressure, whilst 90% of it at the ride height of h/c=0.179. This is of primary importance as the dynamic pressure is the most important lift/downforce parameter.
- The results also show that the wake at the mid-span of the main plane is moving in the vertical direction away from the road, giving the wing a smaller angle of attack and consequently less downforce. On the other hand towards the tip of the wing the wake flow is moving vertically towards the road, giving the wing a bigger angle of attack and consequently more downforce.
- The influence that dynamic pressure and flow incidence have on the wing's performance also explains the reduction in drag that the wing experiences in the wake. In this case both variables have an influence on form drag and induced drag, the latter being related to the square of the downforce being generated.
- The similarities in the wing's wake at different ride heights, as shown in the dynamic pressure contour, turbulence intensity contour and wake profile at mid-flap, illustrates the difficulties of getting a wing to operate in a wake. Due to the small difference between the ride heights in

h/c=0.060 and h/c=0.089 both wings end up operating in wake regions that give them similar performances, even though h/c=0.060 is operating closer to the ground and a performance increase would be expected from this.

- Despite the force measurements not indicating that the wing is in the force-reduction region the CFD-predicted pressure distribution and the wall shear stress indicates the likelihood of the flap being partially separated along the trailing edge. This is further corroborated by the normalized velocity profiles which show an 80% velocity deficit downstream of the flap mid-span at x/c=1, similar to that seen on the wing in the undisturbed conditions with the boundary layer separated from the flap.
- The effect of oncoming flow turbulence on the performance of the wing was shown in the CFD-predicted wall shear stress plots. These showed that a wing operating in a high-turbulence flow is less likely to separate (Wilson et al. (2008)), whilst a wing operating in a low-turbulence flow is likely to have a laminar boundary layer separation with turbulent reattachment.

5.5 Conclusions

In this chapter the results for a wing operating in a disturbed flow were presented. These results confirmed the influence of the wake from the wake-generator on the reduction of performance of a trailing wing. The analysis was done by examining the influence each of the main flow features in the wake (low dynamic pressure, high turbulence and variable flow incidence) and their individual influence on the trailing wing's performance.

Although the wing was tested at various ride heights the influence that the leading wake-generator has, even at higher ride heights, means that there is not a region where the wing could be placed to minimize the performance loss. Of the three main wake features identified in Chapter 4 the reduction in dynamic pressure is possibly the one that is most difficult to ameliorate, whilst flow angularity and turbulence intensity may be used favourably to improve the

performance of the trailing wing. This would, however, require a change in the way race cars are currently designed and introduce new regulations that would push the development of race cars in a direction that would reduce the wake size, in order to increase the dynamic pressure in the wake, and increase downwash, or reduce upwash, to aid the trailing car's front wing by increasing its angle of attack.

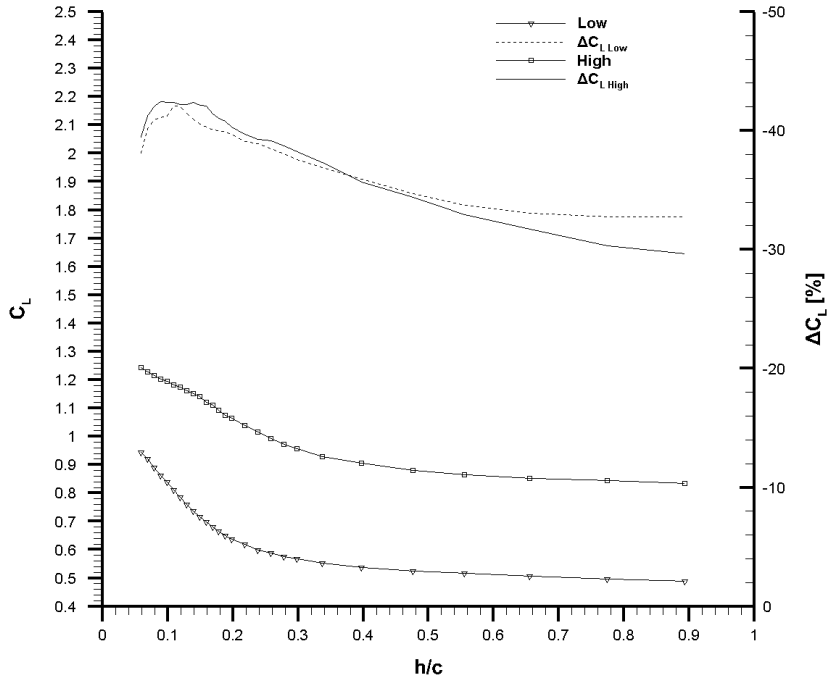

Figure 5-1: Variation with ride height of downforce in the disturbed flow and percentage change of downforce compared to the undisturbed case, for the low (13.8º) and high (23.9º) flap settings. Δ= ±1.40E-02

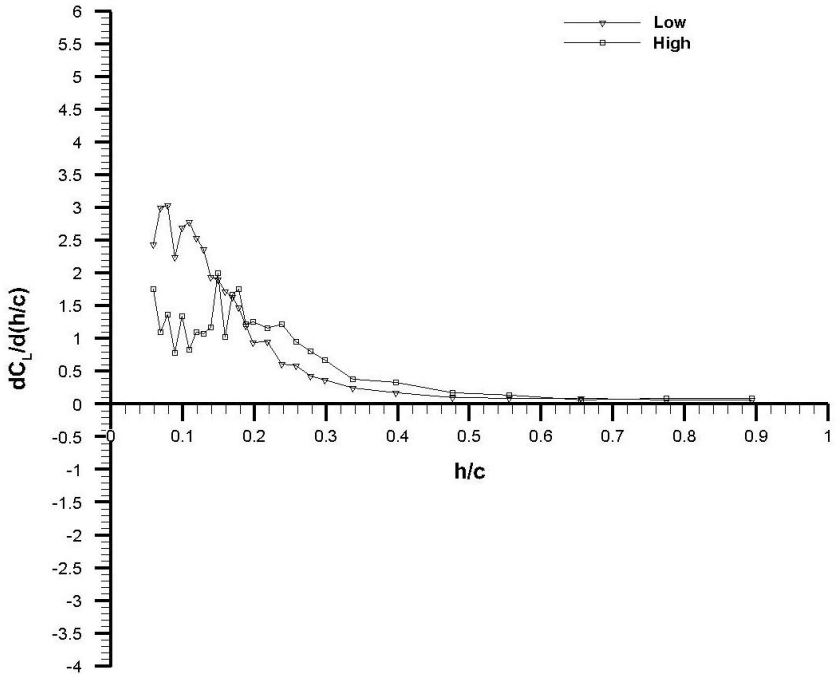

Figure 5-2: Variation with ride height of downforce slope in the disturbed flow for the low (13.8º) and high (23.9º) flap settings. Δ= ±7.18E-02

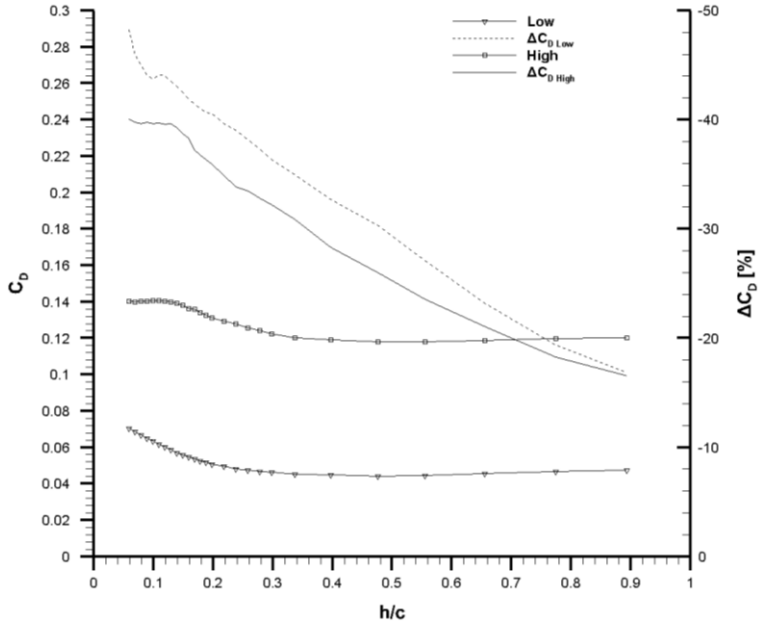

Figure 5-3: Variation with ride height of drag in the disturbed flow and percentage change of drag compared to the undisturbed case, for the low (13.8º) and high flap (23.9º) settings. Δ= ±2.33E-03

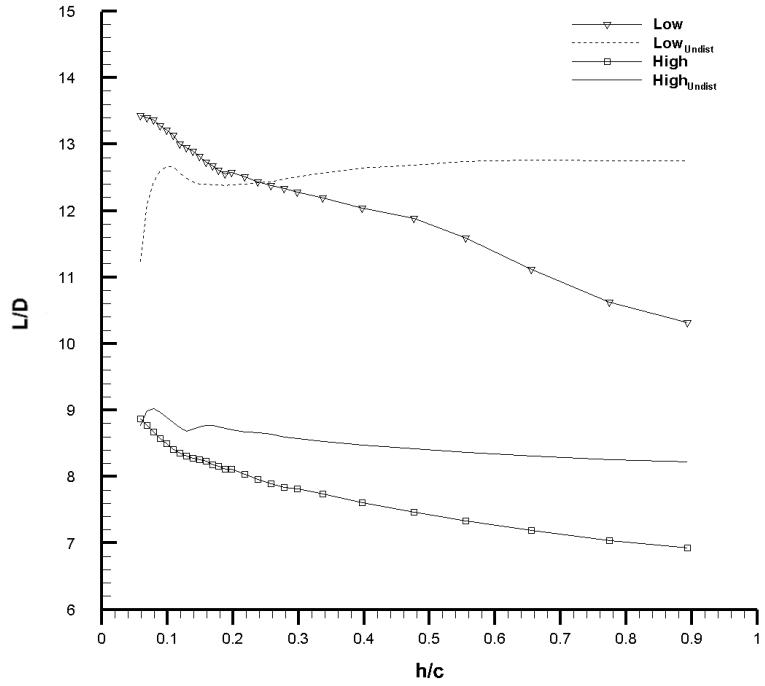

Figure 5-4: Variation with ride height of lift-to-drag ratio in the disturbed flow (symbols) compared to the undisturbed case (no symbols), for the low (13.8º) and high flap (23.9º) settings. Δ= ±2.26E-01

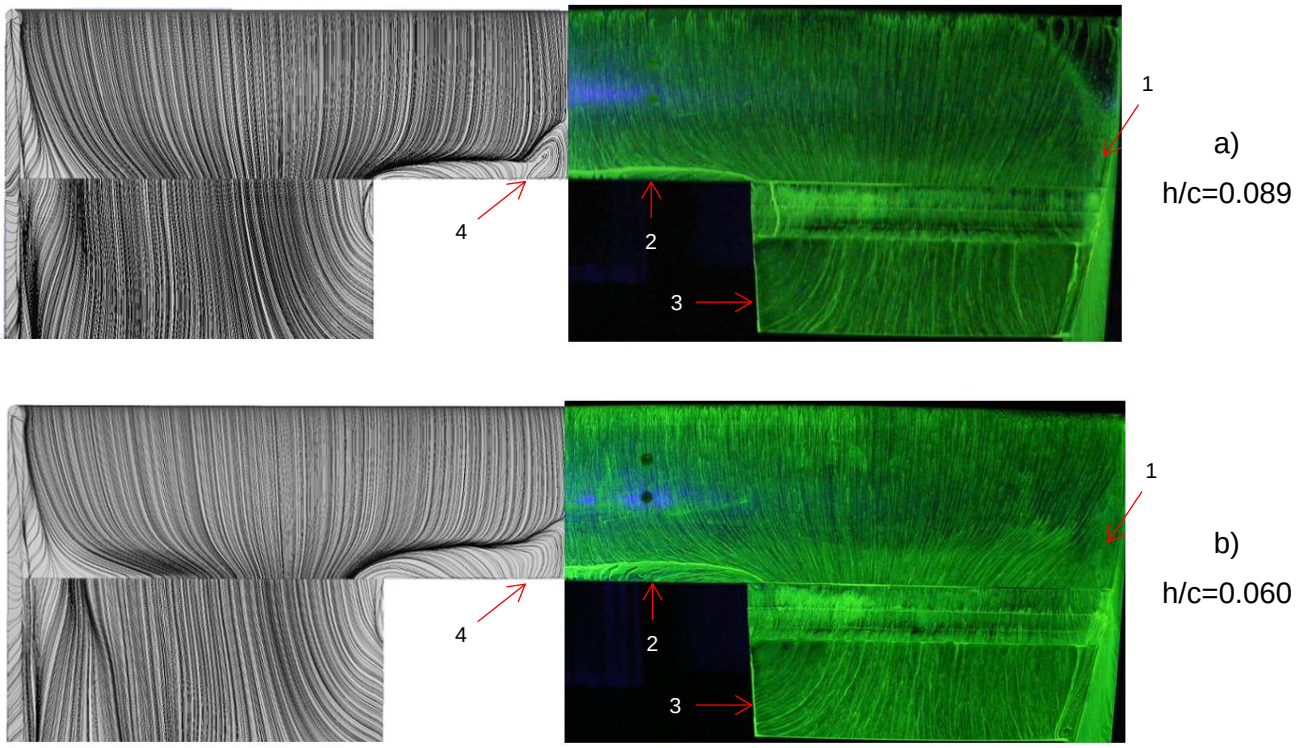

Figure 5-5: Comparison of experimental and CFD-predicted surface flow on suction surface of wing at high flap setting; leading edge uppermost, CFD on left, experimental on right. (0º yaw, 0º roll)

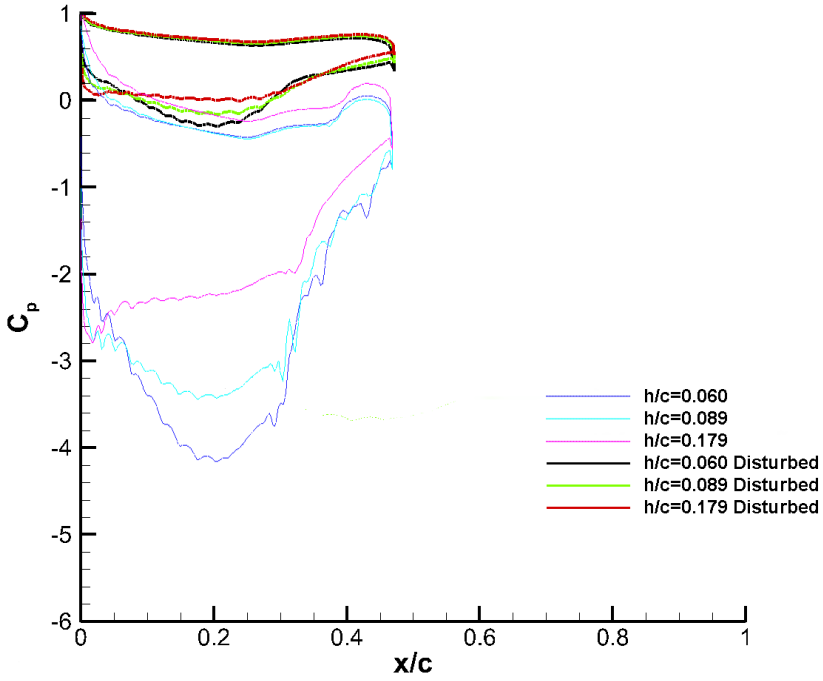

Figure 5-6: CFD prediction of the variation with ride height of the chordwise pressure distribution around the wing's main plane at mid-span for the undisturbed and disturbed flow cases

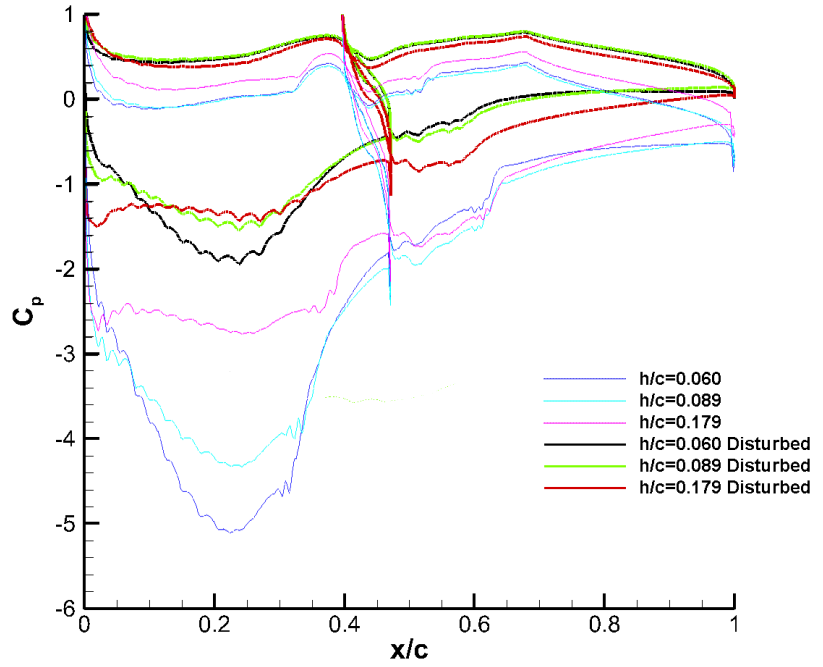

Figure 5-7: CFD prediction of the variation with ride height of the chordwise pressure distribution around the wing's main plane and flap, at the flap mid-span for the undisturbed and disturbed flow cases

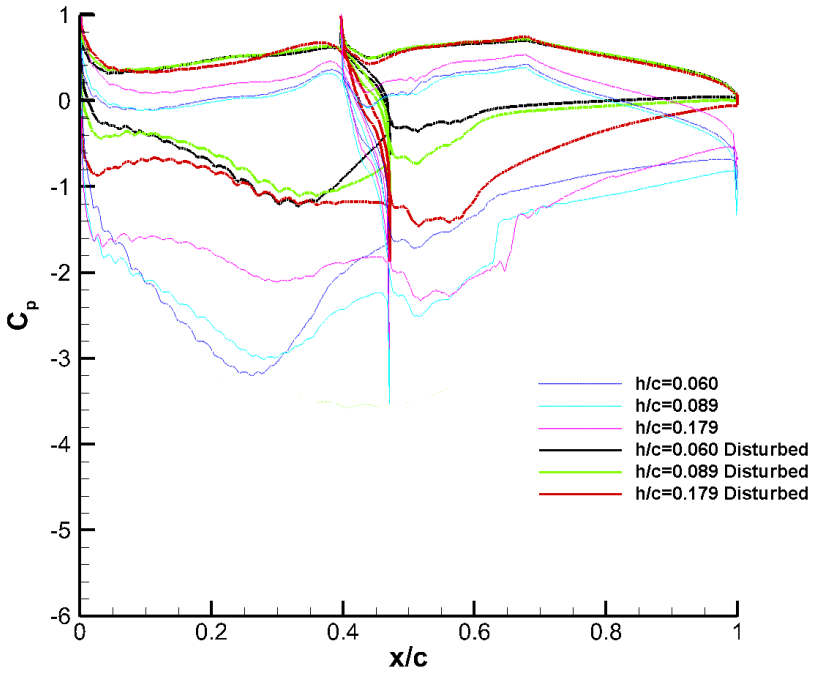

Figure 5-8: CFD prediction of the variation with ride height of the chordwise pressure distribution around the wing's main plane and flap at the wing tip for the undisturbed and disturbed flow cases

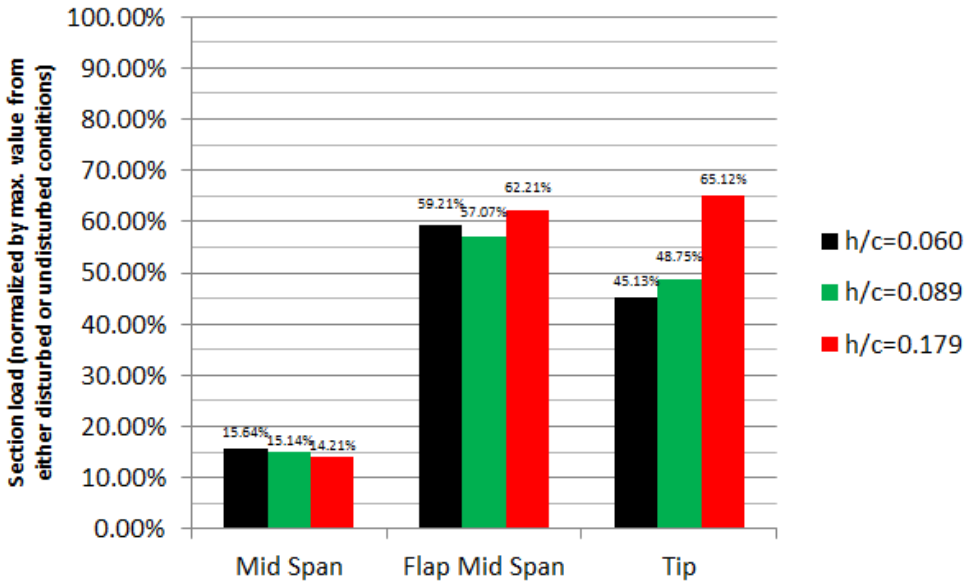

Figure 5-9: Bar graph of CFD-predicted wing section loading in the disturbed flow, normalized with the maximum loading seen in the data range. (0º yaw, 0º roll, CFD results)

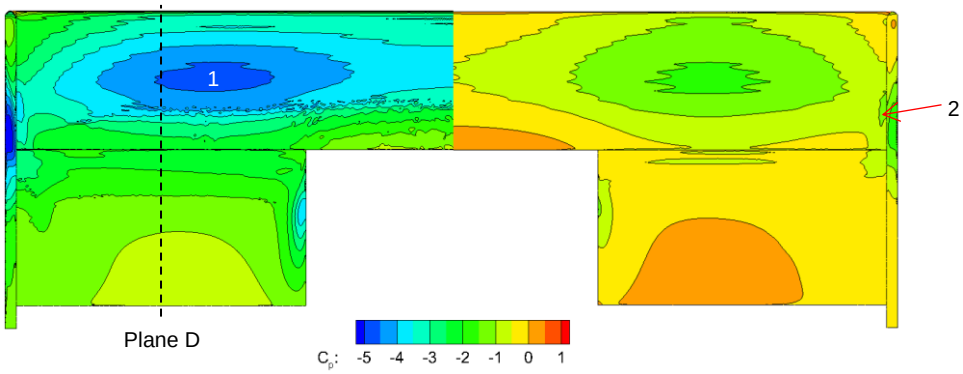

Figure 5-10: Pressure coefficient comparison between the high-flap-setting wing at h/c=0.089 in undisturbed (left) and disturbed (right) conditions; leading edge uppermost. (0º yaw, 0º roll, CFD results)

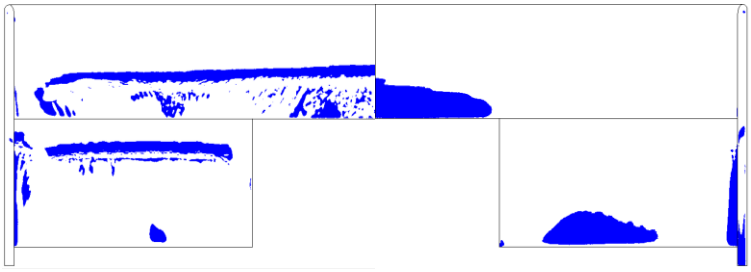

Figure 5-11: CFD-predicted regions of zero wall shear stress on the high-flap-setting wing at h/c=0.089; leading edge uppermost, undisturbed on left, disturbed on right. (0º yaw, 0º roll, CFD results)

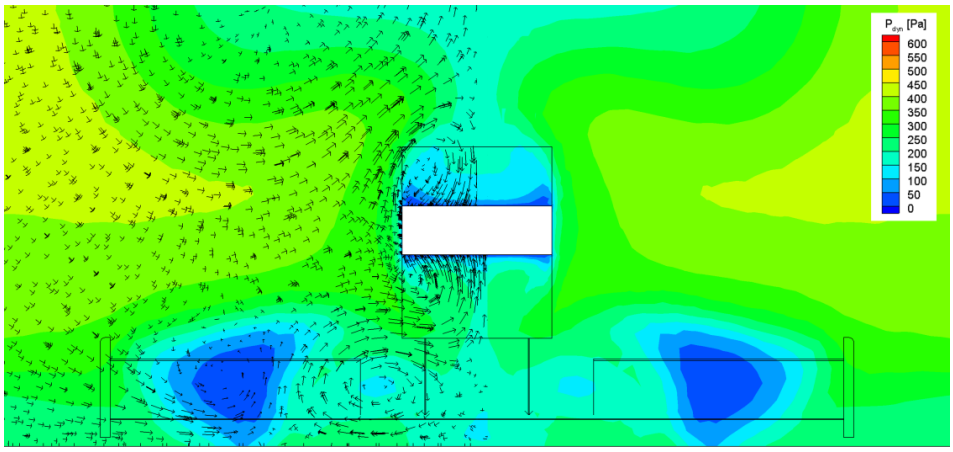

Figure 5-12: Velocity vectors and dynamic pressure contours at x/c=1 (Plane A) behind the wing at h/c=0.060

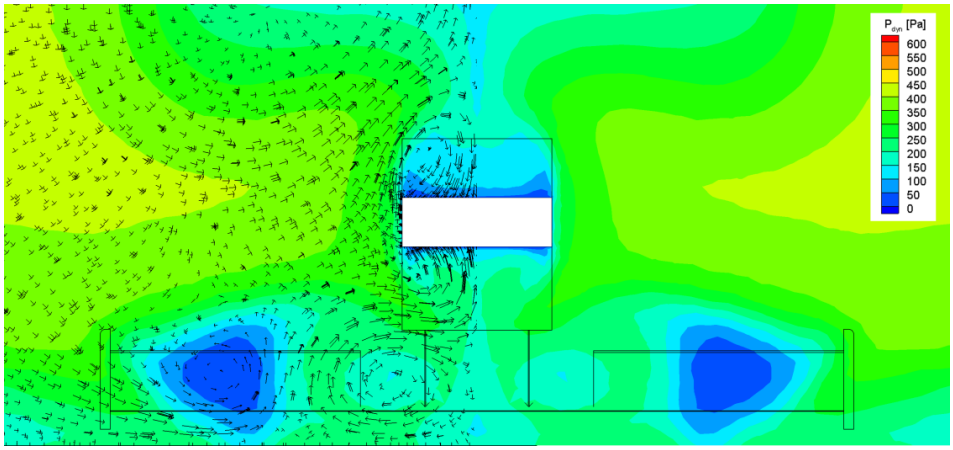

Figure 5-13: Velocity vectors and dynamic pressure contours at x/c=1 (Plane A) behind the wing at h/c=0.089

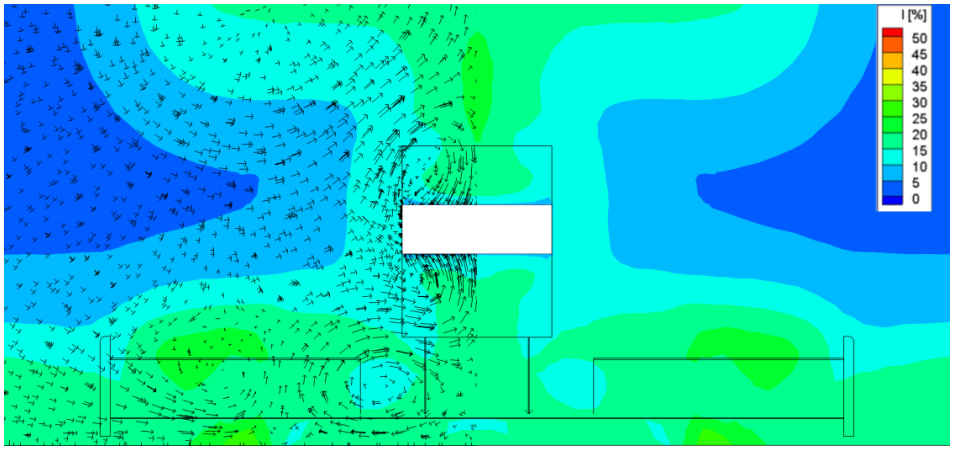

Figure 5-14: Velocity vectors and turbulence intensity contours at x/c=1(Plane A) behind the wing at h/c=0.060

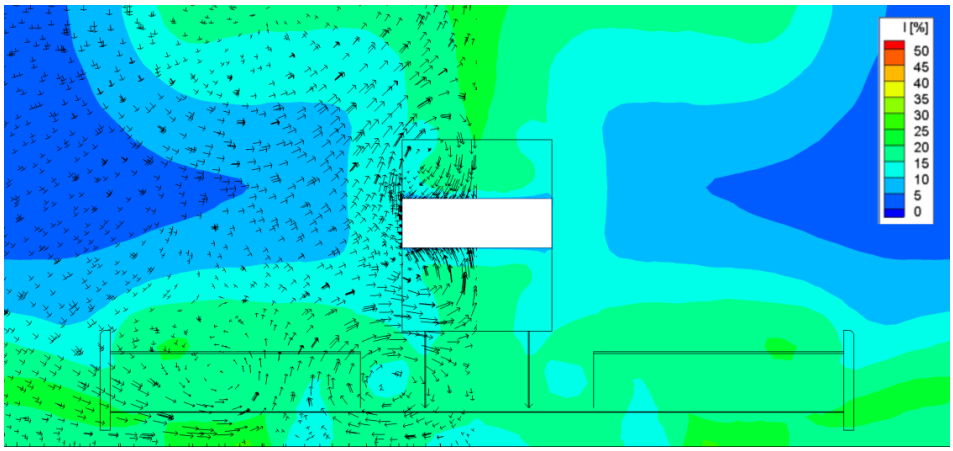

Figure 5-15: Velocity vectors and turbulence intensity contours at x/c=1 (Plane A) behind the wing at h/c=0.089

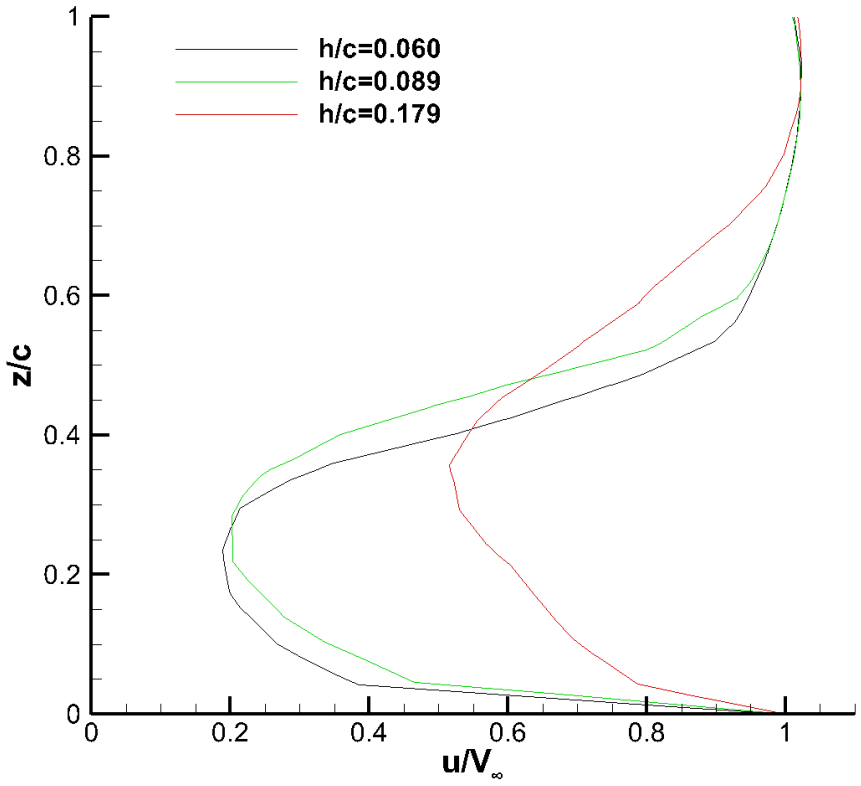

Figure 5-16: Mid-flap normalized flow velocity at different ride heights, at x/c=1 behind the wing

6 Conclusions and Future Work Suggestions

6.1 Conclusions

The aim of this research was to improve the understanding of the performance of a monoposto car's front wing when operating in realistic on-track conditions, including roll, yaw and immersion in the wake of a leading monoposto car. To achieve this and meet the objectives defined in Section 1.3, experimental and numerical techniques were used to examine the upstream, downstream and surface flows on a 50% scale wing operating both in an undisturbed and disturbed flow, as well as the main flow features of the wake from a representation of a leading monoposto car. This included an experimental investigation into the influence of roll and yaw on the performance of a monoposto car's wing in an undisturbed flow. From this research the following conclusions have been drawn.

1. The main characteristics of a monoposto car's wake were identified as:
    a. low dynamic pressure, up to 84% lower than in the freestream;
    b. high turbulence intensity, up to 25%;
    c. local flow incidence variation, with upward flow at mid-span and downward flow at the tips.
2. Independently of the flap angle a multi-element wing immersed in the wake of a leading monoposto's wake experiences a reduction of both downforce (up to 42.7%) and drag (up to 48.2%) throughout its operating range. This reduction in performance is mainly caused by the low dynamic pressure seen in the oncoming flow and has a greater effect when the wing is operating in proximity to the ground, a region where the wing also experiences force enhancement due to the increased circulation caused by the flow being constrained between the wing and the ground, as seen in Chapter 3 and described in the literature survey. Despite this similarity with the wing operating in the undisturbed condition the reduction in downforce caused by the decrease in dynamic pressure outweighs the downforce gains associated with ground effect leading to a net loss of downforce.

3. Although force enhancement is still present on a multi-element wing when immersed in the wake of a leading monoposto car the mechanism behind this phenomenon could not be identified due to the complex flow in the wake as this would require tests where each wake mechanism had to be tested individually and the influence on the trailing wing analysed.
4. The turbulence intensity in the wake has an influence on the boundary layer on the multi-element wing, with the laminar region no longer being present for $Re_c \approx 1.4x10^5$. As shown through the CFD-predicted wall shear stress the turbulent wake will delay boundary layer separation, but the precise influence of freestream turbulence intensity on the trailing wing would have to be studied in isolation from the other two main wake characteristics.
5. As a consequence of the lower dynamic pressure in the wake the trailing wing experiences higher static pressure on its surface and consequently the pressure difference between the pressure and suction surfaces is lower, leading to weaker tip vortices. Despite both the inner and outer-tip vortices suffering a drop in strength the flap inner-tip vortices experienced a smaller reduction in strength than the outer tip vortices, as they operate higher off the ground in a region where the vortices are more stable.
6. As a consequence of the leading body's counter-rotating wing tip vortices the local flow incidence will change along the span of the trailing wing. These changes in local flow incidence will lead to a decrease of angle of attack on the trailing wing if the flow has a vertical component in the upward direction, as seen at the trailing wing's central plane where a decrease of up to 26° in angle of attack is found. Conversely, if the vertical flow component is in the downward direction it will lead to an increase in the trailing wing's angle of attack, as seen at the mid-flap span and wing tip where the increase in angle of attack reached 6° and 4° respectively. Although this effect may influence positively or negatively the performance of the wing depending on the vertical velocity magnitude along the wing span, the effect on its own may not lead to a significant

change to the wing's performance as the dynamic pressure has a predominant effect outweighing the influence of the change in angle of attack due to the flow incidence.

7. The k-kl-w turbulence model proved to be a reliable model as it was able to predict the loads for the wing in the undisturbed condition, to within 2.7% for C_L and 5.9% for C_D, and was able to predict accurately the surface flow features on the wing. As with most computational turbulence models the k-kl-w model struggled to predict accurately the results for the wake development and the wing operating in the wake. Nevertheless the model was able to predict the important flow features seen in the wind tunnel and the results obtained with this computational model were deemed to be satisfactory, giving confidence that it could be used to fill in gaps in the experimental data. Despite this the computational resources required to run a simulation using this model are unpractical for models with more details than the model used in this study, such as full-car models.
8. A wing operating at small yaw angles (<5°) will experience, due to the presence of a region of separation on the windward side flap, a reduction of 3.5% in downforce with an increase of 2.6% in drag. Despite this the results showed that the downforce enhancement/reduction mechanisms in ground effect are unchanged and occur at the same ride heights as the case at 0° yaw.
9. A multi-element wing in roll operating in ground effect may exhibit more overall downforce than a wing operating at zero degrees of roll. This increase in downforce when the wing is operating in roll is caused by each section of the wing operating at different heights along the downforce slope, leading to higher sectional loading along the span than those found at the nominal ride height. Considering an arbitrary ride height the section at the nominal ride will experience the same loading as the unrolled wing. Depending on the position on the downforce slope the lower semi-span will find itself in the force-enhancement region with a greater downforce increase slope compared to the other semi-span

which is higher above the ground. This leads to a net downforce greater than that seen at the nominal ride height.

In summary, when trailing another monoposto car the wake of the leading car will significantly reduce the aerodynamic performance of the front wing of the trailing car. Due to the wake characteristics highlighted in this study it is highly unlikely that even with some careful design work that it will be possible to travel in the wake of a leading monoposto car without reducing the aerodynamic performance of the trailing monoposto car's front wing.

Whilst on track a monoposto car's attitude will constantly change with the car heaving, rolling and yawing, making it difficult to design the car for one specific condition. In the current study it was found that when a wing is subjected to small angles of roll (<3°) the downforce generated by a wing in ground effect can be increased. It was also found that a wing when at small angles of yaw (<5°) exhibits identical performance enhancement/reduction mechanisms as a wing at 0° of yaw, despite a small decrease in downforce and increase in drag. Due to these very specific conditions it is very unlikely that is will be possible to design a monoposto car to exploit the findings without having the capability of setting the car so that it always operates at the optimum conditions.

As a final remark, it is important to remember that in this investigation the wing was studied as an independent entity without the presence of a downstream body or rotating wheels in its proximity. Although both these elements depend on the flow from the wing and will also influence it, the flow characteristics that cause the performance limitation of the wing will occur independently of the presence or absence of these components. This way the conclusions taken from this study can be considered as applicable to a complete vehicle under the same conditions.

6.2 Future Work Suggestions

The literature review highlighted the limited availability of studies into the influence of the wake of a leading monoposto car on the front wing of the trailing one. This situation is caused by the vast computational resources required and

the dimensional limitations in the majority of wind tunnels that do not allow for experimental studies to be carried out with two large-scale models in the test section at the same time. The present work can be seen as an introduction into the field and contributes to the subject by identifying the most significant characteristics of a leading monoposto car's wake and the influence it has on the aerodynamic performance of the front wing of a trailing monoposto car.

Wing Geometry

Although it is expected that the wake of the leading monoposto is predominant, it would be of interest to understand whether different wing geometries are less susceptible to the wake minimizing the performance loss.

Boundary Layer Flow

The performance of a wing in ground effect is very sensitive to changes to the wing's boundary layer because of the Reynolds number ranges involved. In this study the presence of a separation bubble was noted on the suction surface of the wing. Although outside the scope of this work it is understood that the bubble can lead to significant changes to the results. This way a detailed understanding of the influence of this structure and the influence that the wing shape has on the bubble is required, as this may lead to the development of wings that exploit the presence of the bubble to increase performance.

Simplification of the Computational Approach

Due to the limited time available to refine the computational approach it was decided that the approach would focus on mesh refinement instead of fast computation times. This led to a very big mesh which might have been too refined for the purposes of this study. A simplified mesh may lead to similar results and be less expensive computationally. Further correlation with surface pressure readings and for different wing configurations would be of interest in order to set this model as a standard model for wake studies.

References

Agathangelo, B. & Gascoyne, M. (1998). Aerodynamic design considerations of a formula 1 racing car. SAE Paper 980339.

Ahmed, S.R. (1981). An Experimental Study of the Wake Structures of Typical Automobile Shapes. Journal of Wind Engineering, Vol. 9, pp. 49-62.

Albers, A., Brys, J., Illg, S., Roop, J. and Ashworth, J. (2003). Experimental investigation of identical cars in close proximity. AIAA Paper 2003-3817, 21st Applied Aerodynamics Conference, Orlando, FL.

Basara, B., Przulj, V., and Tibaut, P. (2001). On the calculation of external aerodynamics: industrial benchmarks. SAE Paper 2001-01-0701.

Bearman, P.W. (1997). Near wake flows behind two- and three-dimensional bluff bodies. Journal of Wind Engineering and Industrial Aerodynamics, 69-71, pp. 33-54.

Beves, C. (2009). An investigation into the use of low aspect ratio spherical wells to reduce flow separation on an inverted wing in ground effect. PhD thesis, The University of New South Wales.

Braslow, A. & Knox, E. (1958). Simplified method for determination of critical height of distributed roughness particles for boundary layer transition at mach numbers from 0 to 5. Technical report, NACA, Langley Aeronautical Laboratory.

Buchave, P, George Jr, W.K. and Lumley, J.L. (1979). The measurement of turbulence with the laser-doppler anemometer. Ann. Rev. Fluid Mech., 11:443-50.3.

Deviant, Ph., Laverne, T. and Hureau, J. (2002). Experimental study of wind turbine airfoil aerodynamics in high turbulence. Journal of Wind Engineering and Industrial Aerodynamics Vol. 90, pp. 689–707.

Diwan, S. and Ramesh, O.N. (2007). Laminar separation bubbles: dynamics and control. Sadhana – Indian Academy of Sciences Proceedings in Engineering Sciences, 32, Part 1 and 2, pp. 103-109.

Dominy, J.A. & Dominy, R.G. (1984). Aerodynamic influences on the performance of a grand prix racing car. Proceedings of the Institution of Mechanical Engineers, Part D: Journal of Automobile Engineering, Vol. 198, pp. 87-93.

Dominy, R. (1990). The influence of slipstreaming on the performance of a grand prix racing car. Proceedings of the Institution of Mechanical Engineer, Part D: Journal of Automobile Engineering, Vol. 204, pp.35-40.

Dominy, R, Ryan, A. & Sims-Williams, D.B. (2000). The aerodynamic stability of a Le Mans prototype race car under off-design pitch conditions. SAE Paper 2000-01-0872.

Dominy, R, Ryan, A. & Sims-Williams, D.B. (2000). The influence of slip-streaming on sports prototype race car performance. Proceedings of the Institution of Mechanical Engineers, Part D: Journal of Automobile Engineering, 214, pp. 887-894, 2000.

Dominy, R.G. (1992). Aerodynamics of grand prix cars. Proceedings of the Institution of Mechanical Engineers, Part D: Journal of Automobile Engineering, Vol. 206, pp.267-274.

Dominy, R.G. and LeGood, G. (2008). The use of a bluff body wake generator for wind tunnel studies of NASCAR drafting aerodynamics. SAE paper 2008-01-2990.

Dring, R.P. (1982). Sizing criteria for laser anemometry particles. ASME Journal of Fluids Engineering, 104:15-17, March.

Duncan, L.T. (1994). The Effect of Deck Spoilers and Two Car Interference on the Body Pressures of Race Cars, SAE Paper 942520.

Fiumara, F. (2007). Analysis of an Overtaking Manoeuvre. EnginSoft CAE Meeting - Fluent Session, Stezzano, BG, Italy.

Galoul, V. & Barber, T. (2007). A study of an inverted wing with endplates in ground effect. In 16th Australian Fluid Mechanics Conference, pp.919-924.

Genc, M.S., Karasu, I. and Acikel, H.H. (2012). An experimental study on the aerodynamics of NACA2415 aerofoil at low Re numbers. Experimental Thermal and Fluid Sciences, 39, pp 252-264.

Gogel, D. & Sakurai, H. (2008). The effects of end plates on downforce in yaw. SAE paper 2006-01-3647.

Goto, K. and Sakurai, H. (2006). Numerical study for the optimal flap chord length of a two element airfoil. SAE paper 2006-01-3643.

Hoffman, J.A. (1990). Effects of onset free-stream turbulence on the performance characteristics of an airfoil. AIAA paper 90-3025-CP.

Howell, J. (1981). Catastrophic lift forces on racing cars. Journal of Wind Engineering and Industrial Aerodynamics, 9, pp 145-154.

Hu, H and Yang, Z. (2008). An experimental study of the laminar flow separation on a low Reynolds number airfoil. Journal of Fluids Engineering, Vol. 13, 051101-1.

Jasinski, W. & Selig, M. (1998). Experimental study of open-wheel race-car front wings. SAE Paper 983042.

Jeffrey, D., Zhang, X. & Hurst, D. (2001). Some aspects of the aerodynamics of gurney flaps on a double-element wing. Journal of Fluids Engineering, March Vol.123, pp. 99-104.

Katz, J. (1985). Calculation of the aerodynamic forces on automotive lifting surface. Transactions of the ASME: Journal of Fluids Engineering, December Vol. 107, pp. 438-443.

Katz, J. (2006). Aerodynamics of race cars. Annual Review of Fluid Mechanics, 38, pp. 27-63.

Knowles, K., Donoghue D. & Finnis, M. (1994). A study of wings in ground effect. In RAeS Conference on Vehicle Aerodynamics, Loughborough University, pp. 22.1-22.13.

Knowles, K. and Finnis, M.V. (1998). Development of a new open-jet wind tunnel and rolling road facility. 2nd MIRA International Conference on Vehicle Aerodynamics, Coventry, UK, 20-21 October.

Knowles, R (2005). Monoposto racecar wheel aerodynamics: investigation of near-wake structure and support-sting interference. PhD thesis, Cranfield University

Krajnović, S. and Davidson, L. (2001). Large-eddy simulation of the flow around a ground vehicle body. SAE paper 2001-01-0702

Kuya, Y., Takeda, K., Zhang, X., Beeton, S. and Pandaleon, T. (2009). Flow separation control on a race car wing with vortex generators in ground effect. Journal of Fluids Engineering, Vol. 131, 121102-1.

Lanfrit, M. (2005). Best Practice Guidelines for Handling Automotive External Aerodynamics with Fluent. Fluent Deutschland GmbH.

Lawson, N., Knowles, K., Hart, R.J.E., Wray, J.N. & Eyles, J.M. (2002). An experimental investigation using PIV of the underflow of a GA(W)-1 aerofoil section in ground effect. In 4th MIRA International Vehicle Aerodynamics Conference, MIRA.

Mabey, D.G. (1991) A review of scale effects in unsteady aerodynamics. Prog Aerospace Sci, 28, pp 273-321.

Mahon, S. (2005). The aerodynamics of Multi-Element Wings in Ground Effect. PhD thesis, University of Southampton.

Mahon, S. & Zhang, X. (2006). Computational analysis of an inverted double-element airfoil in ground effect. Journal of Fuilds Engineering, Vol. 128, pp. 1172-1180.

Marshall, D.W., Newman, S.J. and Williams, C.B. (2010). Boundary layer effects on a wing in ground-effect. Aircraft Engineering and Aerospace Technology: An International Journal, Vol. 82/2, pp. 99–106.

Moffat, R.J. (1982). Contributions to the theory of single-sample uncertainty analysis. Journal of Fluids Engineering, Vol. 104, pp. 250-260.

Molina, J. & Zhang, X. (2010). Aerodynamics of oscillating wing in ground effect. In 48th AIAA Aerospace Sciences Meeting including the New Horizons Forum & Aerospace Exposition, FL, USA.

Morel, T. (1978). Aerodynamic drag of bluff body shapes characteristic of hatch-back cars. SAE Paper 780267, SAE World Congress & Exhibition, Detroit, MI, USA, February/March.

Moryossef, Y. & Levy, Y. (2004). Effect of oscillations on airfoils in close proximity to the ground. AIAA Journal Vol. 42, No.9, pp. 1755-1764.

Mueller, T.J. and Batill, S.M. (1982). Experimental studies of separation on a two-dimensional airfoil at low Reynolds numbers. AIAA Journal, Vol 20, (4), pp. 457-463.

J. Newbon, R. Dominy, D. Sims-Williams (2014). Investigation into the Effect of the Wake from a Generic Formula 1 Car on a Downstream Vehicle. In Proceedings of International Vehicle Aerodynamics Conference 2014, IMechE, Loughborough, UK.

Nobach, H. (2000). A global concept of autocorrelation and power spectral density estimation for LDA data sets. In Proceedings of the 10th International Syposium of Applications of Laser Techniques to Fluid Mechanics, IST, Lisbon, Portugal.

Pegrum, J.M. (2007). Experimental study of the vortex system generated by a formula 1 front wing. PhD thesis, Imperial College, London.

Ranzenbach, R. & Barlow, J. (1996). Cambered airfoil in ground effect - an experimental and computational study. In International Congress and

Exposition, Vehicle Aerodynamics: Wind Tunnel, CFD, Aeroacoustics and Ground Transportation Systems. SAE Paper 960909.

Ranzenbach, R., Barlow, J. & Diaz, R. (1997). Multi-element airfoil in ground effect - an experimental and computational study. AIAA paper 97-223.

Ranzenbach, R. & Balow, J.B. (1994). Two-dimensional airfoil in ground effect, an experimental and computational study. SAE paper 942509.

Ranzenbach, R. & Barlow, J.B. (1995). Cambered airfoil in ground effect - wind tunnel and road conditions. In AIAA paper 95-1909-CP. AIAA paper 95-1909-CP.

Romberg, G.F., Chianse, J.F. & Lajore, R.J. (1971). Aerodynamics of race cars in drafting and passing situations. In Automotive Engineering Congress, Detroit, MI, USA. SAE Paper 710213.

Soso, M. and Selig, M.S. (2002). An Angle of Attack Correction Scheme for the Design of Low Aspect Ratio Wings with Endplates. SAE paper 02MSEC-15.

Soso, M. & Wilson, P. (2005). Investigating changes to the downforce curve of a double element airfoil in ground effect. SAE paper 2004-01-3558.

Soso, M. (2005), An investigation into the aerodynamics of a wing in ground effect in generic racing car wake flows, PhD thesis, University of Southampton.

Soso, M. & Wilson, P. (2006). Aerodynamics of a wing in ground effect in generic race car wake flows. Proceedings of the Institution of Mechanical Engineers, Part D: Journal of Automobile Engineering, Vol. 220, pp. 1-13.

Soso, M. & Wilson, P. (2008). The influence of an upstream diffuser on a downstream wing in ground effect. Proceedings of the Institution of Mechanical Engineers, Part D: Journal of Automobile Engineering, Vol. 222, pp. 551-563.

Tani, I. (1964). Low-speed flow involving bubble separations. Progress in Aeronautical Sciences, 5, pp 70-103

Toet, W. (2013). Aerodynamics and aerodynamic research in formula 1. The Aeronautical Journal, Vol. 117, 1187.

van den Berg, M.A. and Zhang, X. (2009). The aerodynamic interaction between an inverted wing and a rotating wheel. Journal of Fluids Engineering, Vol 131, 101104-1.

Watkins, S., Ravi, S. and Loxton, B. (2010). The effect of turbulence on the aerodynamics of low Reynolds number wings. Engineering Letters, 18:3, EL_18_3_09.

Wilson, W., Dominy, R. & Straker, A. (2008). The aerodynamic characteristics of a race car wing operating in a wake. SAE Paper 2008-01-0658.

Wright, P.G., The influence of aerodynamics on the design of formula one racing cars. Int. J. of Vehicle Dynamics, Vol. 3, no. 4, pp. 383-397, 1982.

Young, L. (2003). Laser measurement of the airflow around a racing car aerofoil with flap. MSc thesis, Cranfield University.

Zahm, A. & Bear, R. (1921). Ground-plane influence on airplane wings. Journal of the Franklin Institute, May, pp. 687-693.

Zerihan, J. (2001). An investigation into the aerodynamics of wings in ground effect. PhD Thesis, University of Southampton.

Zerihan, J. & Zhang, X. (2000a). Aerodynamics of single element wing in ground effect. Journal of Aircraft, Vol.37, no. 6, pp. 1058-1064.

Zerihan, J. & Zhang, X. (2000b). An experimental study of a single element wing in ground effect. Unpublished material.

Zerihan, J. & Zhang, X. (2001). A single element wing in ground effect; comparisons of experiments and computation. 39th AIAA Aerospace Sciences Meeting and Exhibit, Reno, NV, USA. AIAA Paper 2001-0423.

Zhang, X. & Zerihan, J. (2002). Aerodynamics of a double element wing in ground effect. 40th AIAA Aerospace Sciences Meeting and Exhibit, Reno, NV, USA. AIAA Paper 2002-0834.

Zhang, X, Zerihan, J., Ruhrmann, A. & Deviese, M. (2002). Tip vortices generated by a wing in ground effect. In 11th International Symposium on Applications of Laser Techniques to Fluid Mechanics, IST, Lisbon, Portugal.

Zhang, X., Senior, A. and Ruhrmann, A. (2003a) Vortices behind a bluff body with an upswept aft section in ground effect. International Journal of Heat and Fluid Flow Vol. 25, pp. 1–9.

Zhang, X. and Zerihan, J., Aerodynamics of a Double Element Wing in Ground Effect. AIAA Journal, Vol. 45, pp. 1007-1016, 2003b.

Bibliography

Abbott, I.H. and von Doenhoff, A.E. (1960). Theory of Wing Sections. Dover Publications, UK.

Barlow, J.B., Rae, W.H. and Pope, A. (1999). Low-Speed Wind Tunnel Testing. Wiley, Third Edition.

Benzing, E. (2012). Ali/Wings: Their Design and Application to Racing Cars. Giorgio Nada Editore, Italy.

Coleman, H.W. and Steele, W.G. (1999). Experimentation and Uncertainty Analysis for Engineers. John Wiley & Sons, 2nd edition, UK.

Dantec Dynamics (2004). Statistical stop criteria in BSA flow sotware. Product information 189, Denmark.

Hucho, W.H. (1998) Aerodynamics of Road Vehicles. Society of Automotive Engineers International, fourth edition.

Liebeck, R. and Blackwelder, R. (1987). Low Reynolds number – separation bubble, University of Southern California, Final Technical Report for contract N00014-84-K-0500 (Available from Defense Technical Information Center as AD-A199 378).

Katz, J. (1995). New Directions in Racecar Aerodynamics – Designing for Speed. Bentley, 1st edition.

Kirkup, L. (1995). Experimental Methods: An Introduction to the Analysis and Presentation of Data. John Wiley & Sons, 1st edition, UK.

Moffat, R.J. (1988). Describing the uncertainties in experimental results. Experimental Thermal and Fluid Science, Vol. 1, pp. 3-17.

Smith, A.M.O. and Gamberoni, N. (1956). Transition, pressure gradient and stability theory, Proc. 9th Int. Congr. Appl. Mech, John Wiley and Sons, Chichester, UK.

van Ingen, J.L. (1956). A suggested semi-empirical method for the calculation of boundary layer transition region, Report Nos. V.T.H-71, Report V.T.H.-74 (in English), Delft, The Netherlands.

von Doenhoff, A.E. and Horton, E.A. (1958). A low-speed experimental investigation of the effect of a sandpaper type of roughness on boundary-layer transition. NACA Rep 1349.

White, F.M. (1974). Viscous Fluid Flow. McGraw-Hill, New York, USA.

White, F.M. (2011). Fluid Mechanics, 7th Edition. McGraw-Hill, New York, USA.

Wright, P. (2001). Formula 1 Technology. Society of Automotive Engineers, Warrendale, PA, USA

Ansys Fluent User Guide

ICEM CFD User Guide

Appendix A – Wind Tunnel Specifications

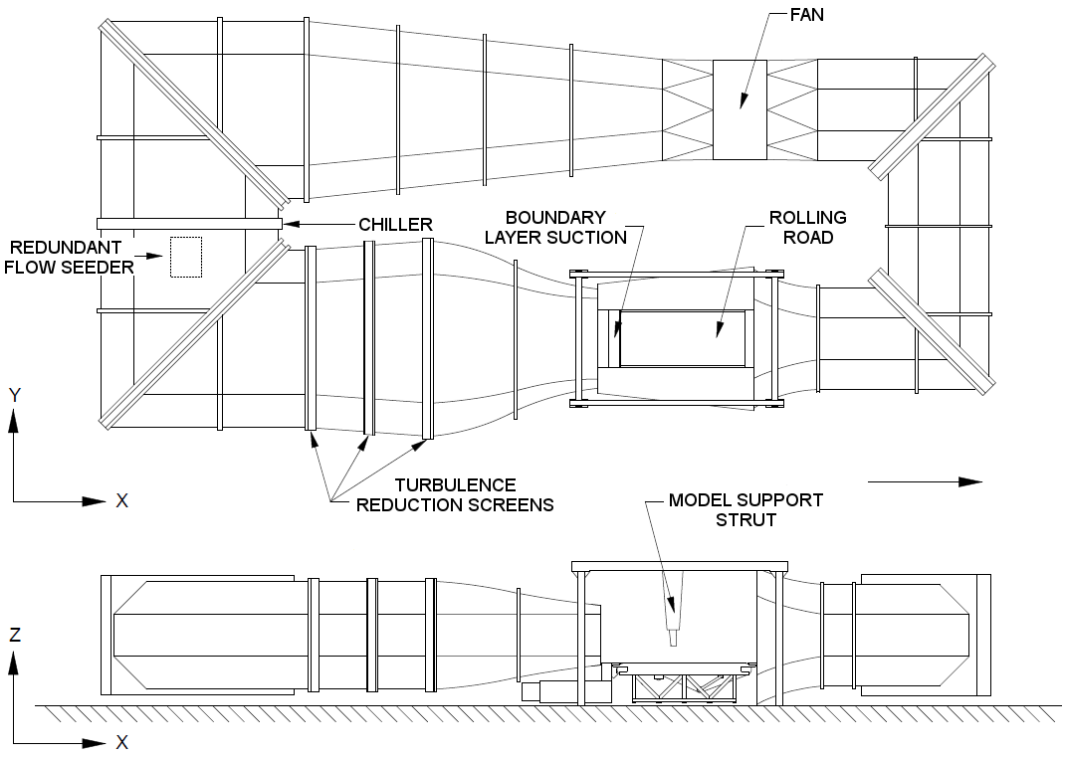

Figure A-1 Schematic of the DS Hougton Wind Tunnel

Type		Closed circuit, 3/4 open-jet with rolling road
Contraction Ratio		3.31:1
Nozzle Dimensions		2.74m x 1.66m
Max. Flow Velocity		$42ms^{-1}$
Flow Velocity Error		<0.2%
Boundary Layer Thickness		1.58mm at leading edge of wing
Turbulence Intensity		0.3% 0.7% with redundant flow seeder
Turbulence Reduction Screens		3x 53% open area, wire mesh
Maximum Rolling Road Velocity		$50ms^{-1}$
Temperature Control	Air	±0.5°C via 400kW cooling circuit
	Road	±0.5°C via 150kW cooling circuit
Force Balance		6-component Aerotech, internal to model
Wind Tunnel Control System		Pi Mistral
Data Logging System		Pi Mistral

Appendix B – Wind Tunnel Model Geometry

B.1 Simplified Wing Asssembly

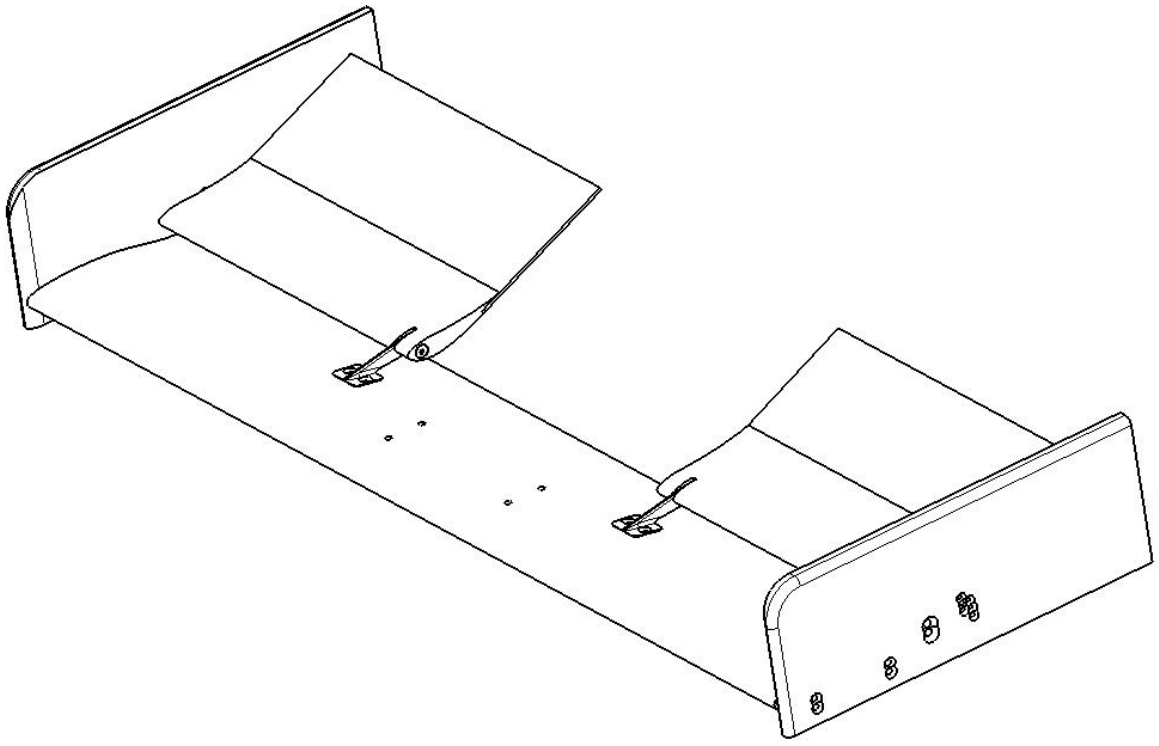

Figure B-1 Isometric view of the double-element wing used in the study.

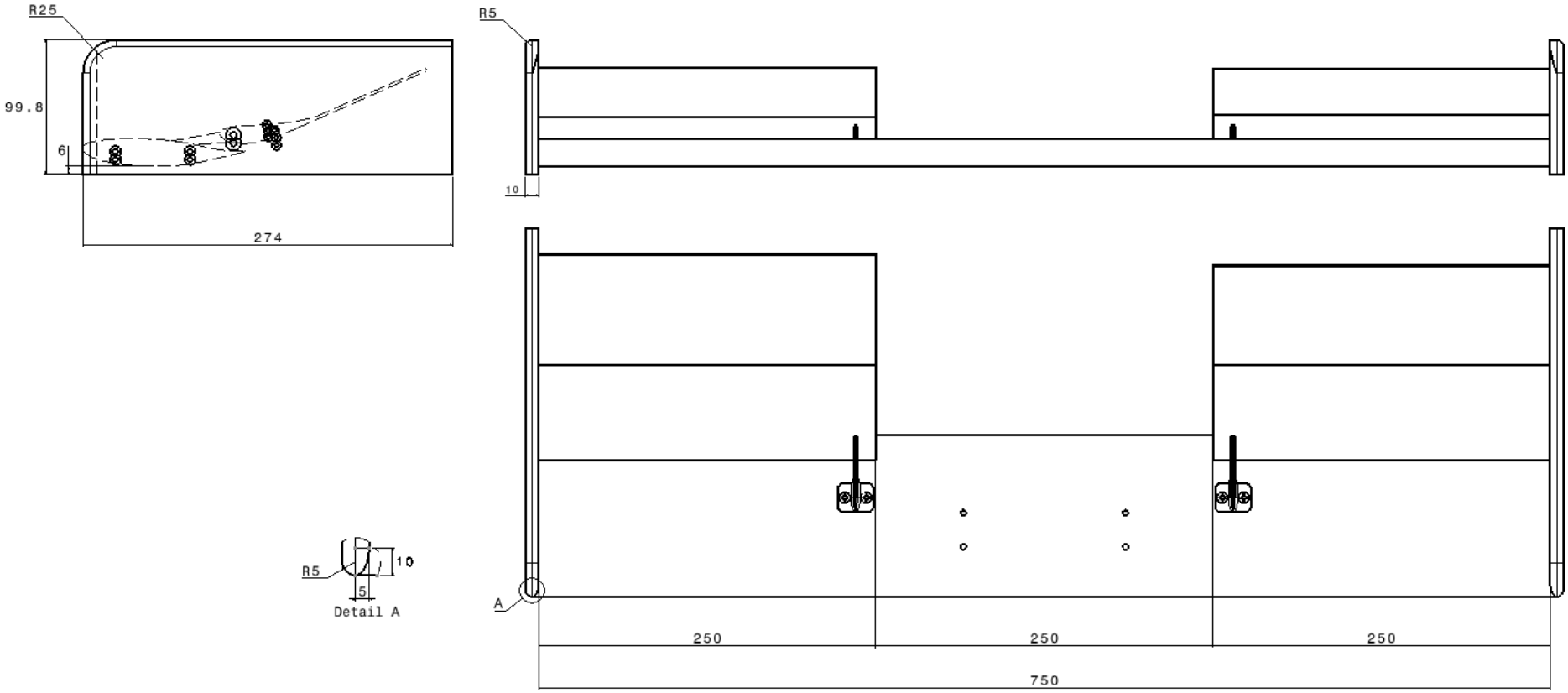

Figure B-2 Dimensions of the double-element wing used in this project

B.2 Streamlined Body

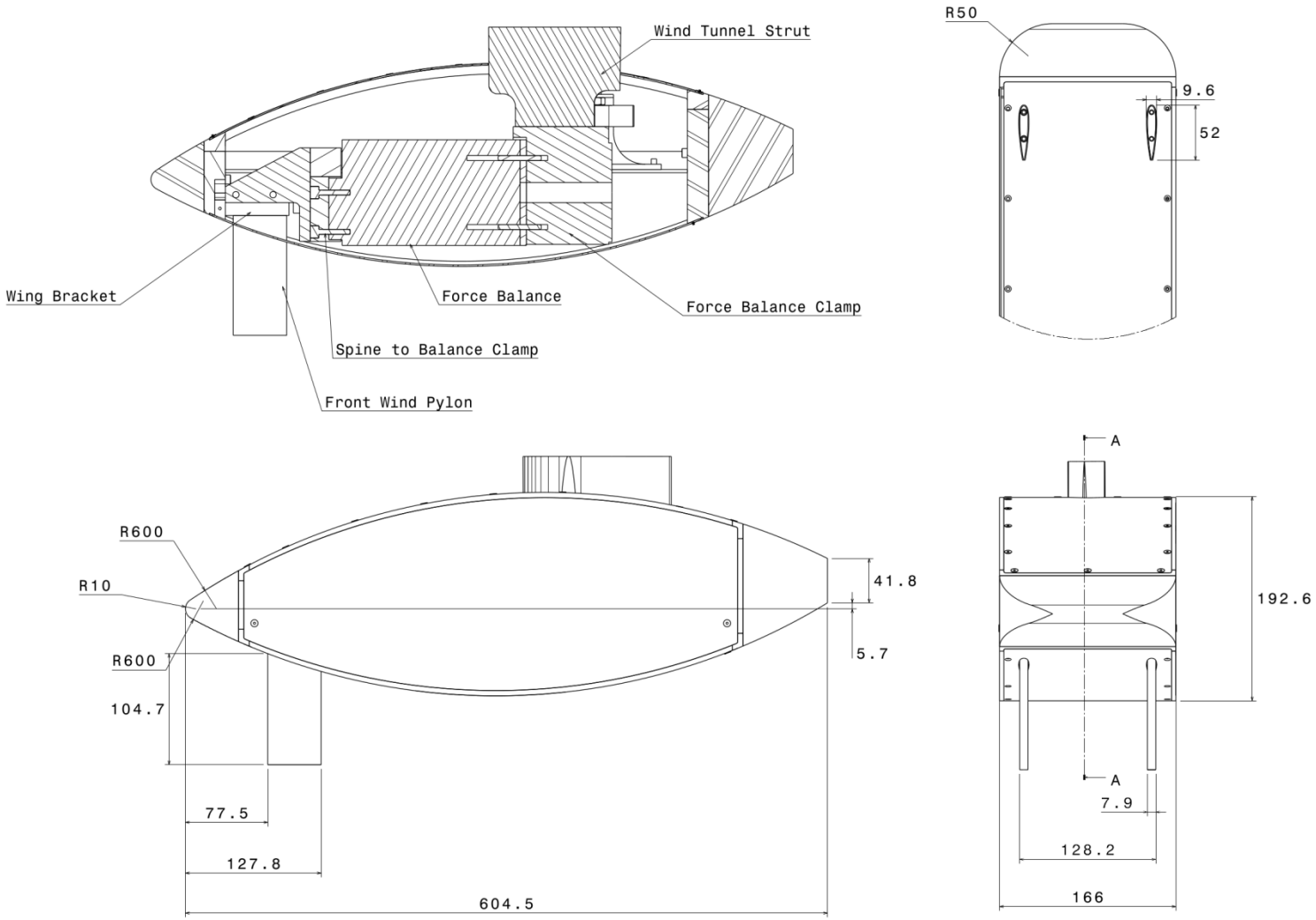

Figure B-3 Dimensions and layout of the streamlined body.

B.3 Wake Generator

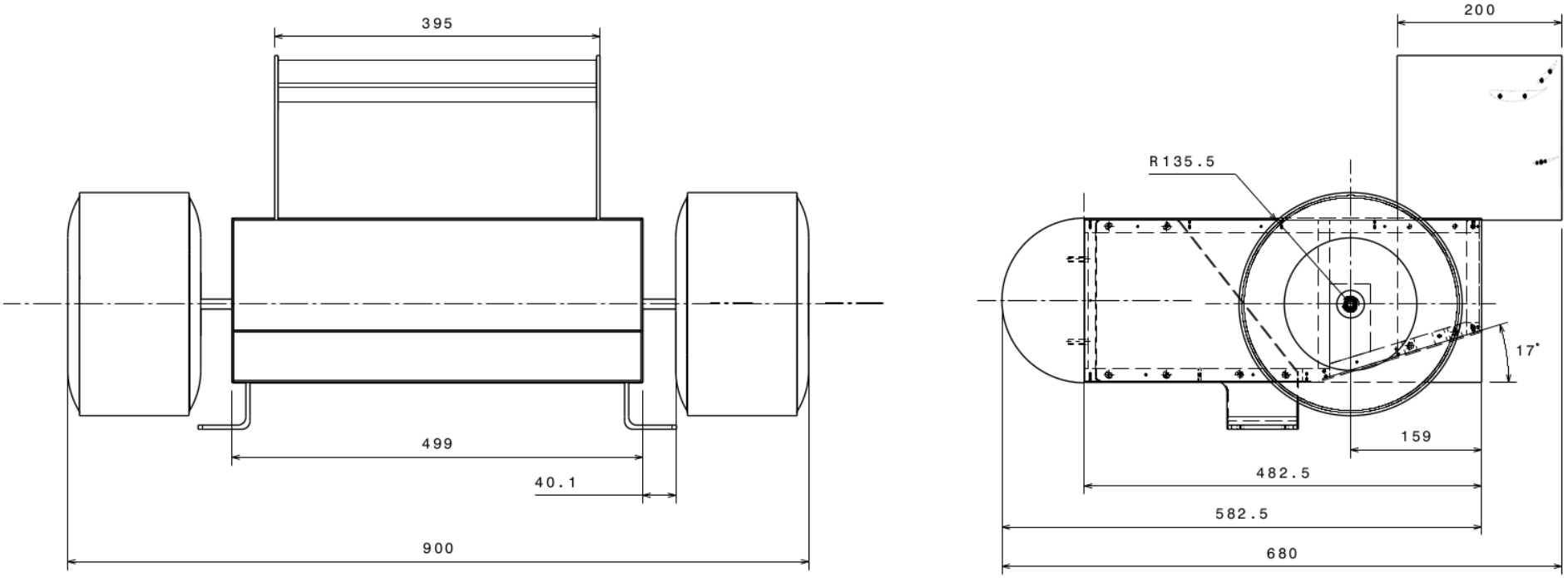

Figure B-4 Dimensions of wake-generator.

B.4 Wing Installation Behind Wake Generator

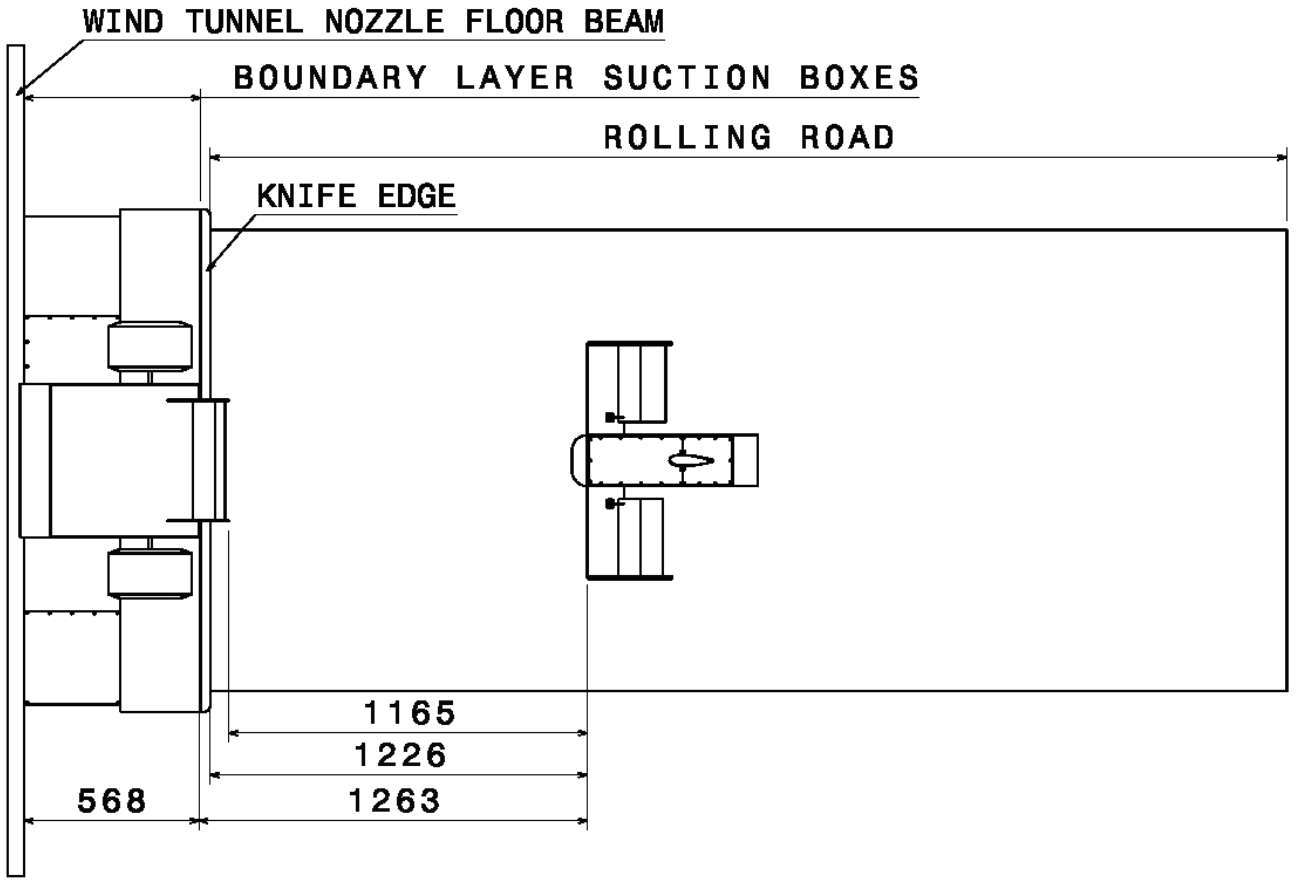

Figure B-5 Installation dimensions for wing behind wake-generator.

Appendix C – Uncertainty Analysis

C.1 Force Measurements Uncertainty

An Aerotech 6-component force balance was used throughout the experimental runs to measure the forces acting on the wing. The data logging system acquired the 6 component measurements simultaneously for 20 seconds at a sampling rate of 10Hz. Before the start of the experimental runs different sampling frequencies were studied and 200 samples was chosen as it gave satisfactory repeatability for the conditions tested. The values were acquired for 20 seconds and then averaged using a moving-average scheme. The architecture of the data-logging software was such that only the averaged values were output, hence not allowing for an uncertainty analysis to be conducted on the data.

Besides the measurement uncertainty from the force balance, there were also uncertainties related to the accuracy to which the wing was set up and the flow conditions. The uncertainties were divided into the different variables influencing the force measurements and the sensitivity of each variable was assessed. The calculations were done in such a way that the values obtained are the maximum possible uncertainty for the experimental setup. Table C-1 presents the different variables assessed, the resulting uncertainty for each variable and an indication of how the error value was obtained.

The total uncertainty value for a 95% confidence level for each balance component was calculated using the root-mean-square method, as described by Moffat (1982).

Table C-1 Uncertainty breakdown into each variable influencing the wing's performance

Variable	Error	C_L	C_D	Source
Force Balance	$\pm 1.6 \times 10^{-2}\%$ - C_L $\pm 7.8 \times 10^{-2}\%$ - C_D	$\pm 1.81 \times 10^{-04}$	$\pm 3.38 \times 10^{-04}$	Aerotech Force Balance Calibration Report
Ride Height	±0.001mm	$\pm 9.71 \times 10^{-04}$	$\pm 8.23 \times 10^{-03}$	Drop Height Gauge Accuracy
Main element Incidence	$\pm 1.7 \times 10^{-4}$ °	$\pm 5.43 \times 10^{-06}$	$\pm 8.19 \times 10^{-05}$	Calculated
Flap Incidence	±0.1°	$\pm 1.89 \times 10^{-03}$	$\pm 7.50 \times 10^{-03}$	Inclinometer Accuracy
Dynamic Pressure	±0.2%	$\pm 9.34 \times 10^{-04}$	$\pm 8.40 \times 10^{-03}$	Sensor Datasheet
Roll	$\pm 4.0 \times 10^{-3}$ °	$\pm 1.83 \times 10^{-05}$	$\pm 1.94 \times 10^{-04}$	Calculated
Yaw	$\pm 2.1 \times 10^{-2}$ °	$\pm 2.94 \times 10^{-05}$	$\pm 3.34 \times 10^{-04}$	Calculated
TOTAL	-	$\pm 1.40 \times 10^{-2}$	$\pm 2.33 \times 10^{-03}$	-

C.2 Laser Doppler Anemometer Uncertainty

As the wind tunnel and equipment was the same as used by Knowles (2005) and Strachan (2006) the same process was used to calculate the laser doppler anemometer uncertainty, although the different seeding medium was taken into account and the uncertainty recalculated.

C.2.1 Seeding Response

The laser doppler anemometer technique relies on laser light being scattered by particles of a flow seeding source. This means that the velocity data obtained

during measurements taken in an experiment is the velocity of the seeding particles and not of the fluid. The selection of the seeding is a compromise between the amount of light scattered and the influence the seeding has on the flow, i.e. a large seeding particle will scatter a greater amount of light but will have a greater influence on the flow itself. Selection of the seeding should also take into account the capability of the method maintaining an approximately constant particle diameter, as a large spread in particle sizes will introduce noise into the acquired signal. Although not related to the measurement errors the accumulation and deposition of particles in the wind tunnel during testing also needs to be considered as excess accumulation of particles in the turbulence reduction screens may alter the flow conditions in the wind tunnel test section. Correct selection of the seeding material with an appropriate volatility that leaves little residue once evaporated can save a significant amount of time.

Originally the seeding was chosen based on previous work done in the D.S. Houghton wind tunnel and the available equipment. This seeding was water-based with 15 % ethylene glycol added as an evaporation inhibitor. The seeding particles were generated by an ultrasonic atomiser which, in combination with a momentum separator, produced a large volume of uniform-diameter (1.3μm), ambient-temperature seeding. Due to problems with this equipment a CF Taylor smoke machine was subsequently used. This machine uses a heater and compressed air to vaporize smoke oil, producing a large volume of uniform-diameter (0.9μm) seeding. The drawback of this system is that the smoke is at a higher temperature than the airflow. For this reason and to aid mixing of the seeding with the flow the smoke was “injected” into the flow downstream of the test section, meaning the smoke would do a full loop in the tunnel and cross the cooling core bringing the flow temperature to a uniform 25°C.

Due to differences in density between the seeding particle and the flow a seeding response error is introduced. This way the ability for the particle to follow the flow and the error associated with it were accessed using the method described by Dring (1982). Using this method the particle’s response to an

acceleration in the surrounding fluid is related to the Stokes number, S_t , of the particle. With the Stokes number being given by the following relationship:

$$S_t = \frac{\rho_p D_p^2}{18\mu T_c} \qquad \text{(Equation 1)}$$

where ρ_p and D_p represent the particle fluid density and diameter respectively, μ the absolute viscosity of the surrounding fluid and T_c the characteristic time for the acceleration. For this case a characteristic time of 8.4×10^{-3} s was used to represent the time taken for a particle to cross the shear-layer in the downwash region. Taking air viscosity as 1.75×10^{-5} kg $m^{-1}s^{-1}$, the density of the seeding fluid as 975 kg m^{-3} and substituting 0.9×10^{-6} m for D_p, the Stokes number was estimated as:

$$S_t = \frac{975\left(0.9*10^{-6}\right)^2}{18(1.75*10^{-5})*(8.4*10^{-3})} = 2.580 * 10^{-15} \qquad \text{(Equation 2)}$$

As proposed by Dring (1982) for small Stokes number ($S_t < 0.01$) the maximum velocity error is equal to the Stokes number. Therefore, the error due to the response of the seeding was negligible.

C.2.2 Velocity Bias

As pointed out above in the seeding response discussion, the LDA signal is generated by light being scattered by seeding particles in the flow. The randomness of the seeding distribution means that there is a link between the flow and the samples but they are not statistically independent. Considering a point in the flow to be uniformly-seeded a fluctuation in velocity above the mean value would move more particles through the measurement volume leading to more samples being obtained than a similar fluctuation below the mean velocity. This way the calculated mean velocity from the raw samples will be biased towards higher velocities.

Removing the velocity bias can be done by weighting the samples by a factor inversely proportional to the velocity of the sample during calculation of the mean value. The use of a particle transit time, t, as a weighting factor was recommended by Buchave et al. (1979).

The following calculation was used to remove the velocity bias from the mean measured signals, *S*:

$$S = \frac{\sum_x^N s_x t_x}{\sum_x^N t_x} \qquad \text{(Equation 3)}$$

with *s* representing the velocity component measured by the anemometer and the subscript *x* referring to the index of the current sample, from the population *N*.

C.2.3 Sampling Error

The interval at which samples of a procedure are acquired influences the uncertainty of the population's mean and variance. For correct estimation of these values statistically-independent samples are required. When two samples are less than one integral time scale, τ_i, apart they are considered to be statistically dependent or correlated. This way, to ensure statistically-independent samples the sampling interval between two samples should be at least double the integral time scale, τ_i, of the process. As it is difficult to collect statistically-independent samples when a particle crosses the measurement volume, the LDA system can operate in "dead-time" mode, where a minimum time between samples could be fixed. This procedure, however, requires prior knowledge of the flow's integral time scale.

As described in Chapter 2 in this work the number of samples obtained at each spatial position was fixed, independently of the time taken to acquire the samples. Once the samples for a given point were acquired the probe would move to the following point. Due to differences in the sampling rate at each point the uncertainty also was different.

Using the method proposed by Benedict and Gould (1996) it was possible to estimate the uncertainty. In their method, it was proposed that a 95% confidence limit for mean value $\overline{U}$ would equal:

$$1.96\sqrt{\frac{\overline{u^2}}{N}} \qquad \text{(Equation 4)}$$

This applies equally to any population distribution assuming that N>50 and that the samples u, are statistically independent. The first criterion was easily fulfilled, however the second was not and was addressed in the following way. The potential number of statistically-independent samples, N_{eff}, was calculated from the sampling time, T_m, and the integral time scale:

$$N_{eff} = \frac{T_m}{2\tau_i} \qquad \text{(Equation 5)}$$

If N>N_{eff}, then N_{eff} was replaced in Equation 4 otherwise it remained unchanged. Still, calculating N_{eff} required a posteriori estimation of the integral time scale.

This estimation for τ_i was done using the method presented by Nobach (2000). As mentioned above, τ_i is related to the correlation of two samples of the same population, and as such can be found from the autocorrelation function, ACF, of the population. Estimating the ACF could be done from the inverse power spectral density of the data, but only if all samples were equidistant. For randomly-sampled data the Fourier analysis is not possible unless the data are re-sampled to be equidistant, a process that may lead to further error due to aliasing.

In a method described by Nobach (2000) the ACF is estimated using slot correlation which does not involve re-sampling the signal and therefore avoids aliasing issues. The method also incorporates transit-time weighting to remove the velocity bias during estimation. Using software written by Knowles (2005) that estimated τ_i at each point in a measurement plane, allowing calculation of N_{eff} and subsequent calculation of the confidence limits for the mean values.

The analysis of the u-component velocity showed that for a 95% confidence interval over 50% of the measured points were found to have an error smaller than 1%.

C.2.4 Measurement Volume Location Uncertainty

As the particle velocity can be measured at any location within the measurement volume a systematic error is introduced due to the dimensions of the measurement volume. This way the uncertainty in the location where the

particle's velocity is measured is half the major dimensions of the measurement volume: 0.012mm, 7.5mm and 0.012 for the x, y and z axis respectively. This uncertainty was taken into account when selecting the measurement grid and planes in order to avoid overlap between measurement points.

C.3 Force Measurement Repeatability

In order to understand if the data from the wind tunnel were repeatable a procedure was implemented where the first run of a day was a repeat of the last run of the previous day. This way it was possible to check if the results matched from one day to another and verify that there were no problems with the wind tunnel and acquisition system.

The repeatability of the data sets was also analysed through a series of repeated runs at various times during the research with the wing in the datum configuration. Repeatability was separated into three categories: short, medium and long term.

Short-term repeatability was regarded as the variations in the forces, for identical wing configuration, during two consecutive test runs with the wind tunnel being stopped between runs. The force data were compared between both test runs, which allowed the short-term repeatability to be quantified. The maximum variation in forces due to short-term repeatability was quantified at $\pm 2.5 \times 10^{-2}$ for C_L and $\pm 3.9 \times 10^{-3}$ for C_D.

Medium-term repeatability was regarded as variations in the force measurements, for identical wing configuration, during non-consecutive test runs with the flap setting having been changed for a test run and returned to the datum position for a repeat run. The force data were compared between both test runs, which allowed the medium-term repeatability to be quantified. The maximum variation in forces due to medium-term repeatability was quantified as $\pm 3.8 \times 10^{-2}$ for C_L and $\pm 1.0 \times 10^{-2}$ for C_D.

Long-term repeatability was regarded as variations in the force measurements, for identical wing configuration, during non-consecutive test runs with the model having been removed from the wind tunnel and re-installed to the datum

position for a repeat run. The force data were compared between both test runs which allowed the long-term repeatability to be quantified. The maximum variation in forces due to long-term repeatability was quantified as $\pm 2.8 \times 10^{-2}$ for C_L and $\pm 6.4 \times 10^{-3}$ for C_D.

C.4 Hysteresis

Hysteresis consists of the dependency of a system output on the present and past outputs. In the case of an inverted wing in ground effect the movement from one ride height to another ride height may lead to different results depending on the direction of movement, e.g. if the wing is being lowered towards the ground or raised away from it.

Tests were carried out to see if the wing geometry used in this study suffered from hysteresis. The results presented in Table C-1 show that although some minor differences were present between the descending and ascending phase the results were satisfactory as they did not present significant jumps between points as noted in other studies.

With no significant differences found in the results it was decided to carry out all measurements in the present study in the descending direction.

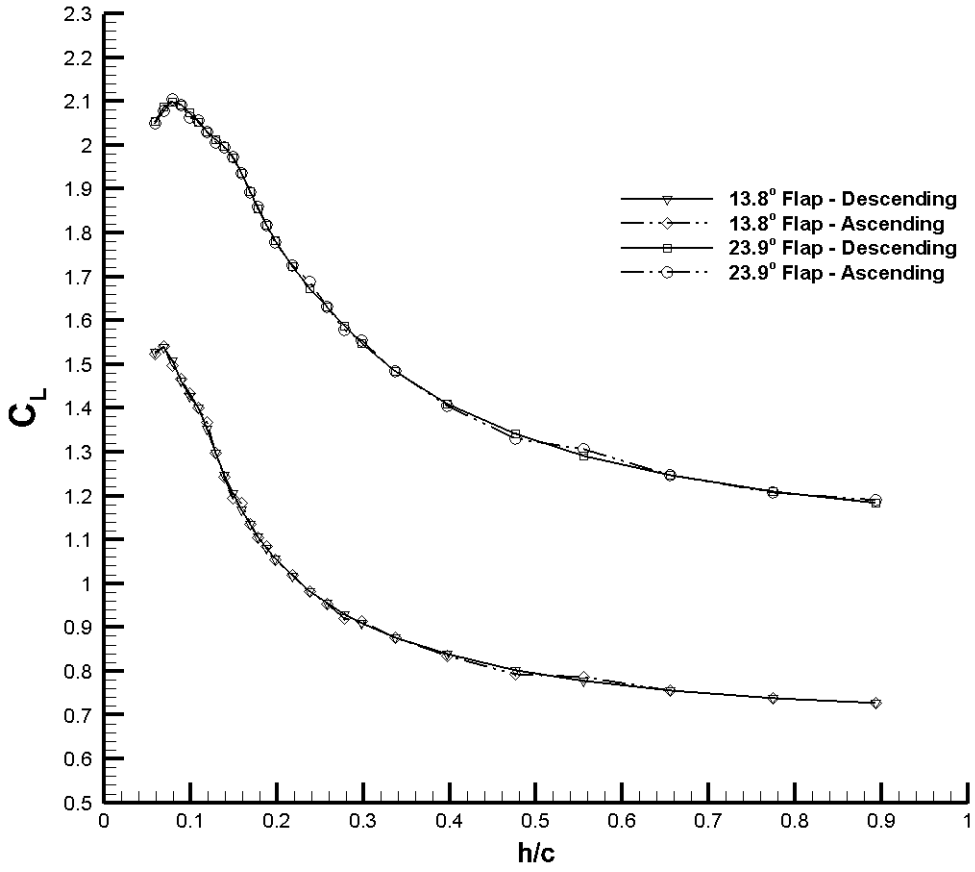

Figure C-1 Variation of downforce coefficient with ride height for both flap settings in both upward and downward movement (0º yaw, 0º roll)

C.5 Roll and Yaw Direction Analysis

Tests were carried to confirm that the wing forces were independent of the direction of change of roll and yaw. The results are presented in Figure C-2 and Figure C-3 for the roll and yaw cases, respectively.

The results show that in both the roll and yaw cases the results are independent of the direction of change of these parameters.

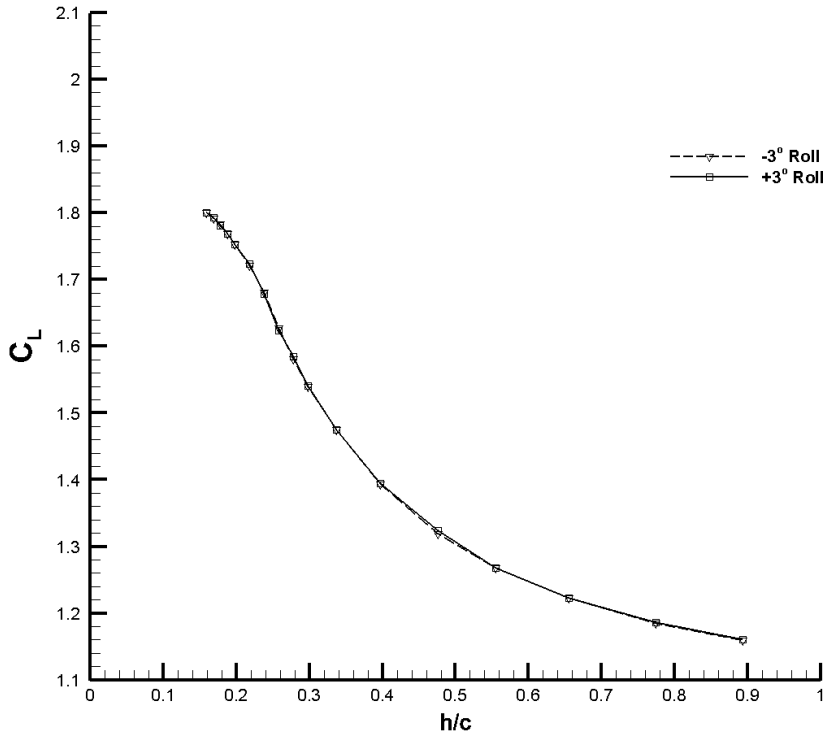

Figure C-2 Variation of downforce coefficient with ride height for symmetric roll angles (0º yaw)

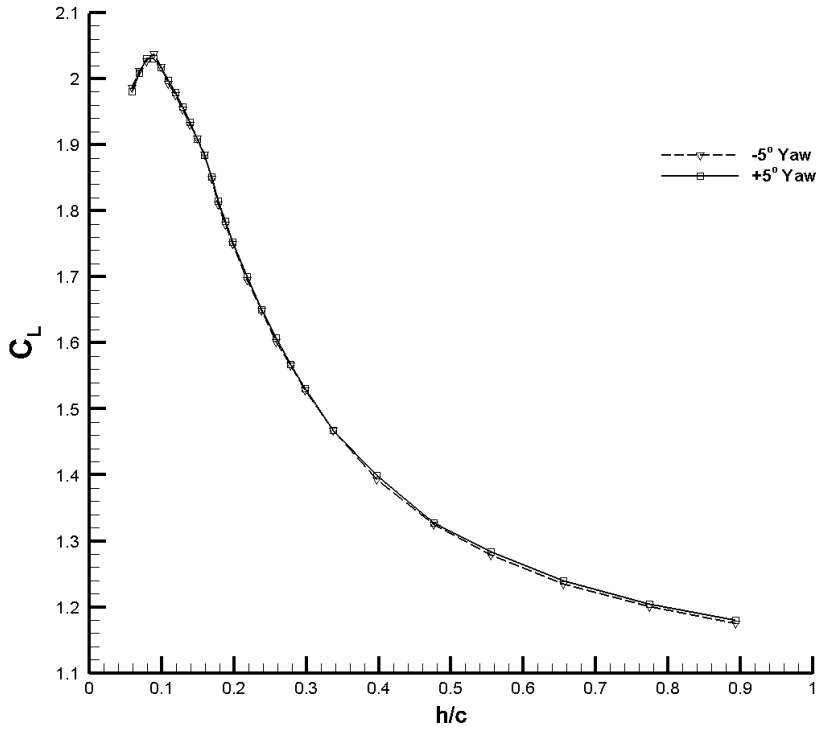

Figure C-3 Variation of downforce coefficient with ride height for symmetric yaw angles (0º roll)

Appendix D – Experimental & Numerical Test Conditions

The following tables show the different experimental set-ups tested during this research.

D.1.1 Force Measurements

Table D-1 and Table D-2 presents the list of configurations for which force measurements were carried out, in the undisturbed and disturbed flow conditions.

Table D-1 List of configurations tested for the undisturbed flow case

	Yaw Angle					**Roll Angle**				
Flap Angle	-5.0	-2.5	0	2.5	5.0	-3.0	-1.5	0	1.5	3.0
13.8	✓	✓	✓	✓	✓	✓	✓	✓		
23.9	✓	✓	✓	✓	✓	✓	✓	✓		✓

Table D-2 List of configurations tested for the disturbed flow case

	Yaw Angle					**Roll Angle**				
Flap Angle	-5.0	-2.5	0	2.5	5.0	-3.0	-1.5	0	1.5	3.0
13.8			✓					✓		
23.9			✓					✓		

D.1.2 Surface Flow Visualization

In Table D-3 and Table D-4 the list of configurations for which surface flow visualization was carried out, in both the undisturbed and disturbed flow conditions respectively, are presented.

Table D-3 List of flow visualization tests carried out for the undisturbed case

	Yaw 0° Roll 0°		Yaw -5.0° Roll 0°		Yaw 0° Roll -3.0°	
	Flap Angle		Flap Angle		Flap Angle	
h/c	13.8	23.9	13.8	23.9	13.8	23.9
0.821	✓	✓		✓		✓
0.365	✓	✓		✓		✓
0.179	✓	✓		✓		✓
0.089	✓	✓		✓		
0.060	✓	✓		✓		

Table D-4 List of flow visualization tests carried out for the disturbed case

	Yaw 0° Roll 0°	
	Flap Angle	
Ride Height	13.8	23.9
0.821		
0.365		✓
0.179		✓
0.089		✓
0.060		✓

D.1.3 LDA Testing

Table D-1 presents a schematic of the planes measured using the laser doppler anemometer. Details of the plane dimensions and number of points acquired for each plane can be found in Table D-5 for the transverse planes, whilst details for the longitudinal planes can be found in Table D-6. The dimensions presented are in absolute distance, in mm, measured from the projection of the endplate trailing edge on the wake-generator's centreline at the ground plane. Due to limitations in the LDA system traverse dimensions it was not possible to measure the initial 100mm of the wake in the longitudinal planes. Details of the LDA configuration can be found in Table D-7.

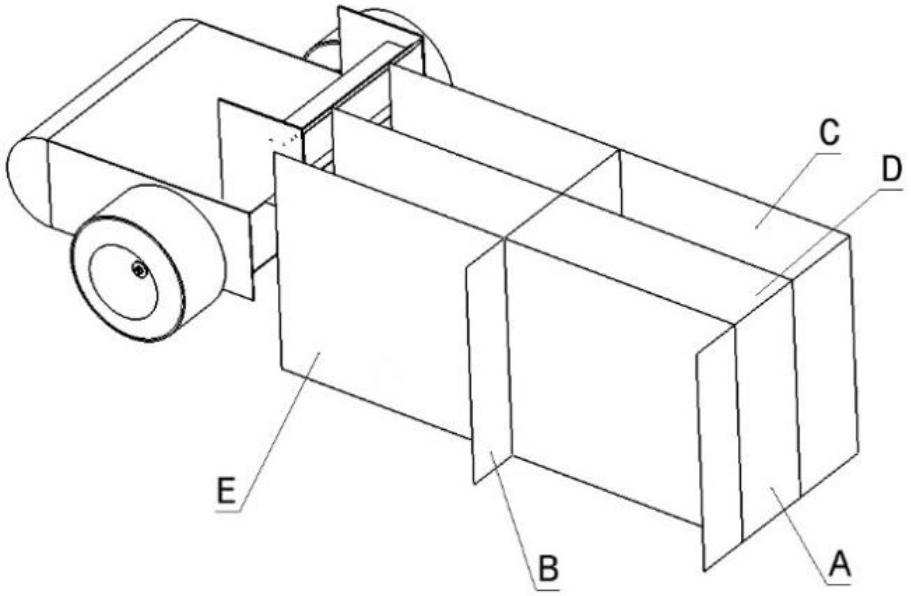

Figure D-1 Schematic of LDA measurement planes behind wake generator in isometric view

Table D-5 LDA measurements carried out on the tranverse planes

Plane	x	Min y	Max y	Min z	Max z	# Points
A	1100	0	425	40	690	442
B	550	0	425	40	690	442

Table D-6 LDA measurements carried out on the longitudinal planes

Plane	y	Min x	Max x	Min z	Maz z	# Points
C	0	100	1100	40	690	1040
D	187.5	100	1100	40	690	1040
E	375	100	1100	40	690	1040

Table D-7 LDA configuration details

Probe Orientation	
u-component (nm)	514.5
v-component (nm)	488
Probe Settings	
Focal Length (mm)	2500
Beam Diameter (mm)	2.2
Expander Ratio	2.97
Beam Spacing (mm)	40
Alignment pinhole (μm)	25

D.1.4 Numerical Study

In Table D-8 the configuration details for the computational study are presented.

Table D-8 Numerical study details

Software	Ansys Fluent 14.5
Basic Configuration	3D, Segregated, Steady
Mesh-type	Viscous-Hybrid
Number of cells:	Undisturbed flow cases: 1.7×10^7 Wake-generator: 3.4×10^7 Disturbed flow cases: 5.0×10^7
Turbulence Model	$k\text{-}k_L\text{-}\omega$
Material	Air
Near-wall treatment	Standard wall functions
Discretization	
Pressure	Second order
Momentum	Second order
Turbulence	Second order
Pressure-Velocity Coupling	SIMPLE
Boundary Conditions	
Inlet Type	Velocity Inlet

Velocity	25m/s
Direction Vector	(1,0,0)
Outlet Type	Pressure Outlet
Ground	Replicating wind tunnel geometry, with stationary ground under wake-generator and moving ground at same velocity as freestream.
Walls	Symmetry

Although in Chapter 4 only the results for the wake-normalized velocity are shown as part of the numerical versus experimental correlation, in Table D-9 the differences between numerical and experimental downforce results are presented.

Table D-9 Difference in downforce between the numerical and experimental results for the undisturbed and disturbed flow cases.

h/c	Undisturbed Flow	Disturbed Flow
0.893	-0.10%	+2.54%
0.397	-0.35%	+2.95%
0.179	-0.71%	+3.83%
0.089	-1.34%	+5.09%
0.060	-2.73%	+5.98%

Appendix E – Published Work

Work published by author of this study:

- Correia J, Roberts L S, Finnis M V and Knowles K. (2014). Scale Effects on a Single Element Inverted Wing in Ground Effect. The Aeronautical Journal; Vol. 118, pp. 797-809.
- Correia J, Roberts L S, Finnis M V and Knowles K. (2014). Aerodynamic Characteristics of a Monoposto Racing Car Front Wing Operating in High Turbulence Conditions. International Vehicle Aerodynamics Conference, Loughborough, UK.

Other work published using data gathered during this study:

- Roberts, L., Correia, J., Finnis, M.V. and Knowles, K. (2015). Aerodynamic characteristics of a wing-and-flap configuration in ground effect and yaw, Proceedings of the Institution of Mechanical Engineers, Part D: Journal of Automobile Engineering [DOI:10.1177/095440715596274]

Appendix F – Unpublished References

Analysis of an Overtaking Manoeuvre

Francesco Fiumara, MEng
CFD Department
Dallara Engineering Srl, Italy

ABSTRACT

This paper describes the work carried out in Dallara to study the problem of the overtaking manoeuvre. First of all a series of steady-state simulations have been executed to investigate how the flow field changes with the relative position between the two cars and to decide on which part of the trajectory of the overtaking car the unsteady-state simulation had to be conducted; then a transient simulation has been performed using the dynamic mesh model available in Fluent.

1. INTRODUCTION

The role of CFD in Dallara has deeply changed from 1998, year in which such technology has been introduced in the company. To the initial study of isolated elements of the car other areas of application have been gradually added, rendering CFD a fundamental tool in the design of every new model. At present, besides being used in the design of important components (front wing, rear wing, airbox, fuel systems) by implementing appropriate simplified geometries, the numerical simulation is applied to the early concept phase and, above all, to the detailed analysis of the full car (because of the strong coupling among the various elements). The knowledge of the strengths and weaknesses of CFD, matured through the continuous comparison with wind tunnel data for several kinds of vehicles, and the increased capacity of parallel computers now have allowed us to deal with some problems for which the experimental approach is not the most practical to follow. Among these there is the overtaking manoeuvre.

Rather than evaluating the sole behaviour of the two cars during the manoeuvre and the forces involved, this study has entailed an analysis to understand how to approach such a scenario, to estimate the importance of the various parameters and to define an adequate procedure of calculation. Therefore, instead of using one of the many cars that we have analyzed in these years, it has been chosen to define a sufficiently simple geometry so as to offer all the characteristics of an open wheels racing car but that, at the same time, permitted to limit the number of the cells (Figure 1).

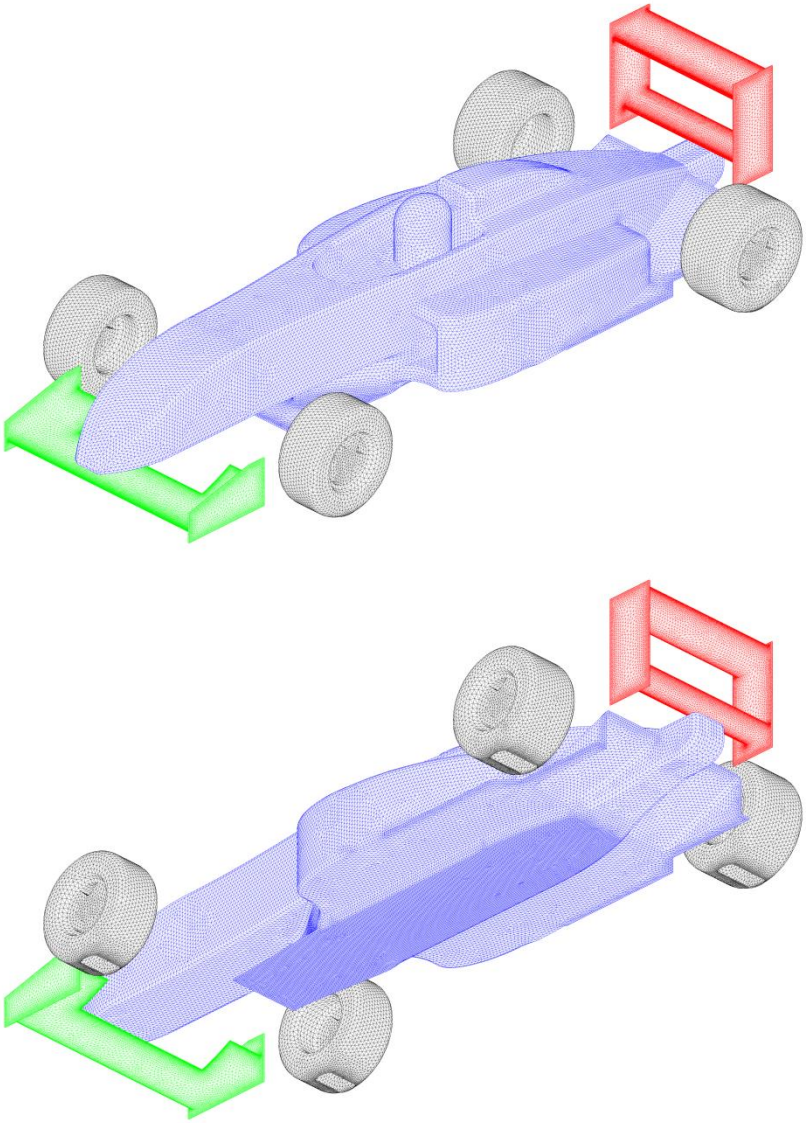

Figure 1: The analysed geometry

The point which has demanded a particular attention has been the determination of the more appropriate method of mesh deformation. Several tests were performed and at the end our choice has fallen on the 2.5D surface remeshing method coupled with the smoothing method because it was found to give the mesh with the best skewness and the smallest variations in cell volume.

2. SIMULATIONS

In order to have preliminary indications on the main aspects of the problem a series of steady-state simulations with different relative positions between the two vehicles have been executed. In Figure 2 it's possible to see the tested configurations.

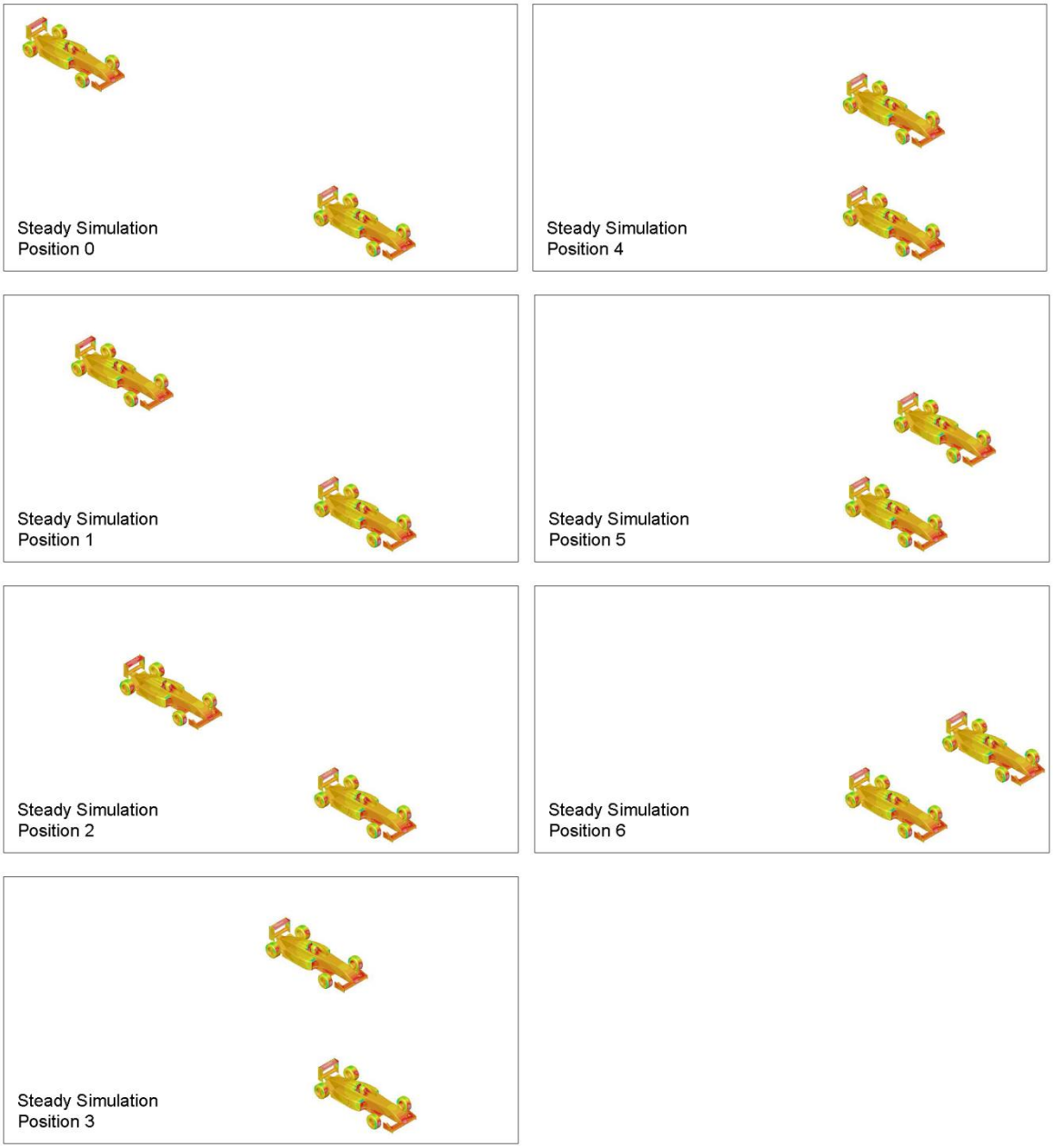

Figure 2: Contours of pressure coefficient for the steady-state simulations

Besides estimating the interaction between the two cars this first phase has allowed us to establish the beginning and end points of the transient simulation. We decided that the calculation started from the position 0 and finished at the position 4 of the steady-state tests, with a total simulation time of 4 s. In Figure 3 some wake visualizations are shown for the interval comprised between 1.5 and 2.5 s, which the analysis has highlighted to be the most critical and on which we have focused our attention.

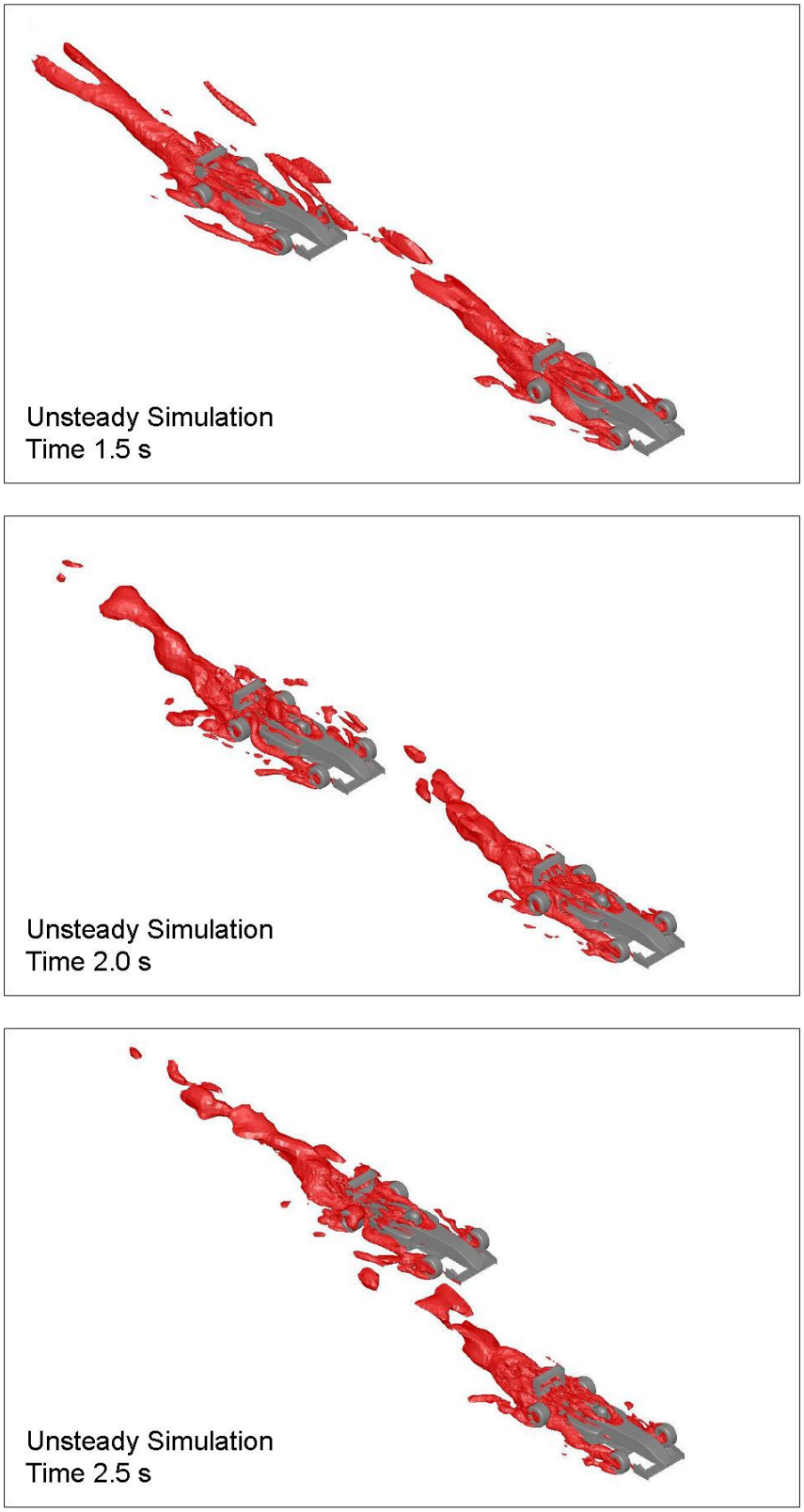

Figure 3: Isosurfaces of total pressure at various steps of the transient simulation

For both the steady-state cases and the single unsteady-state scenario similar hybrid meshes of about 20 million cells were used. Figure 4 shows the mesh of the transient simulation at the initial position with the volume subjected to deformation highlighted in red.

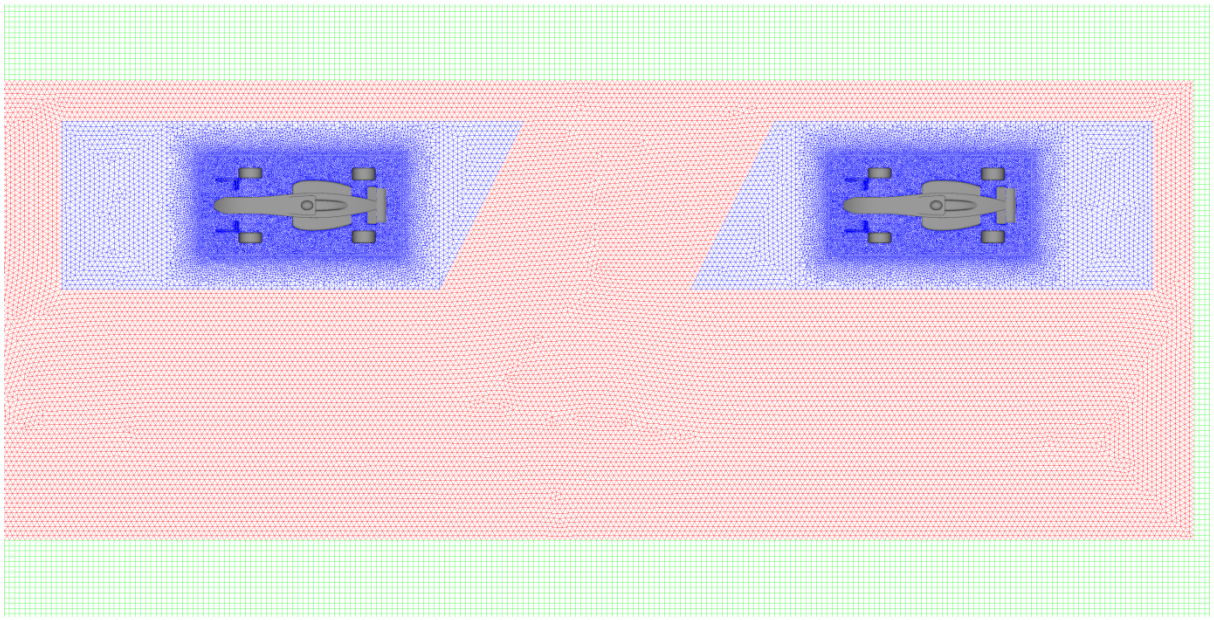

Figure 4: Mesh of the transient simulation at the initial condition

A velocity of 50 m/s at the inlet was used in all the simulations. In the transient case a rigid body motion was imposed to the overtaking car and to the cells around it (coloured in blue in Figure 4), so as to have a difference in velocity of 2.5 m/s between the cars. The RSM turbulence model was adopted for the steady-state simulations and the LES model with the WALE subgrid-scale model for the unsteady-state one.

2. RESULTS

The results of the steady-state cases are shown in Figures 5-8. It's clear that in positions 0-2 the interaction between the two vehicles is very strong and the rearward car has less drag, downforce, front balance and flow rate through the radiators than the forward one. In positions 3-6, instead, they behave almost like isolated cars and it's possible to note only a small increase in the drag of both the cars and in the flow rate through the left radiator of the forward car and the right radiator of the rearward one.

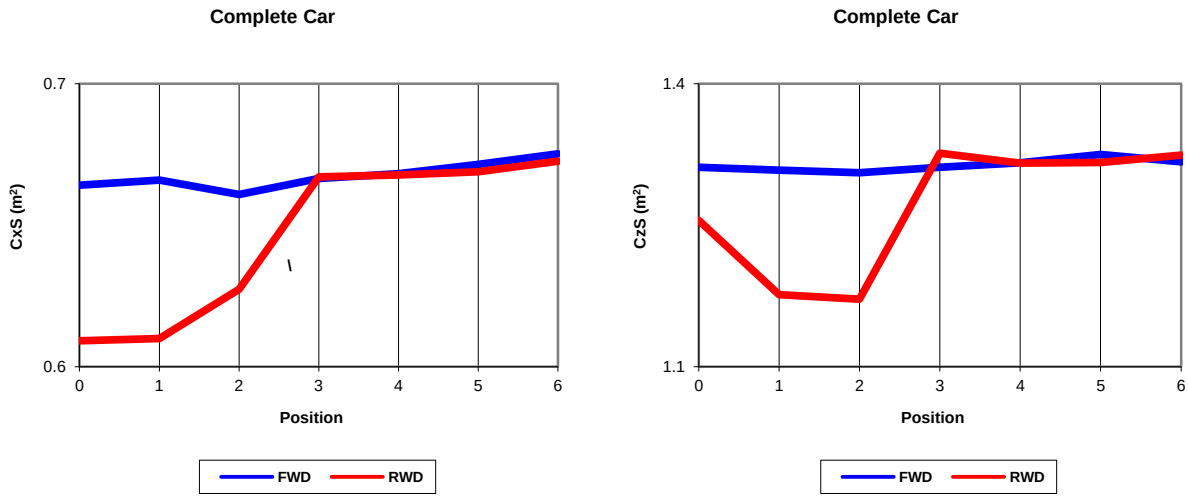

Figure 5: Variation of the total coefficients of the cars with the relative position between them

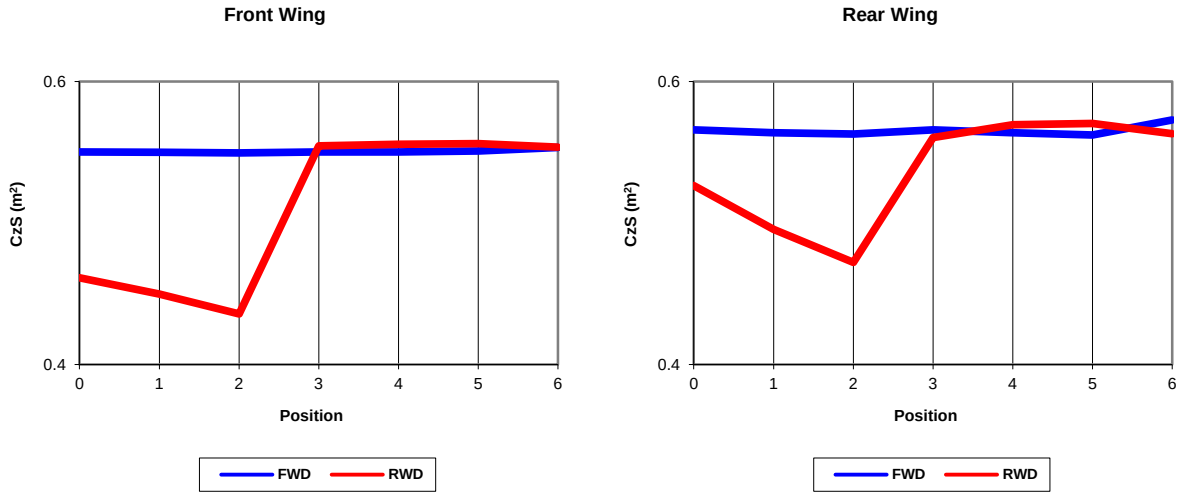

Figure 6: Variation of the downforce coefficients of the wings of the cars with the relative position between them

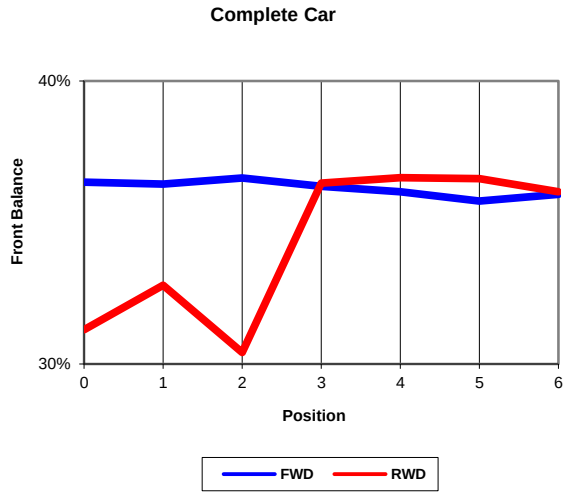

Figure 7: Variation of the front balance of the cars with the relative position between them

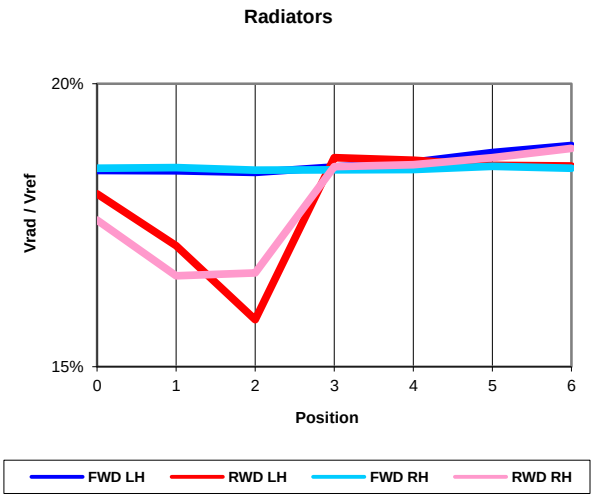

Figure 8: Variation of the flow rate through the radiators of the cars with the relative position between them

The results of the unsteady-state case are shown in Figures 9-12. For the drag and downforce coefficients and the front balance the conclusions relative to the steady-state simulations are still valid and, in particular, at 2.5 s from the beginning of the calculation the values of these parameters are almost the same for the two cars. Considering the forces, instead, the difference between the two cars depends obviously on how big the gap in velocity is between them.

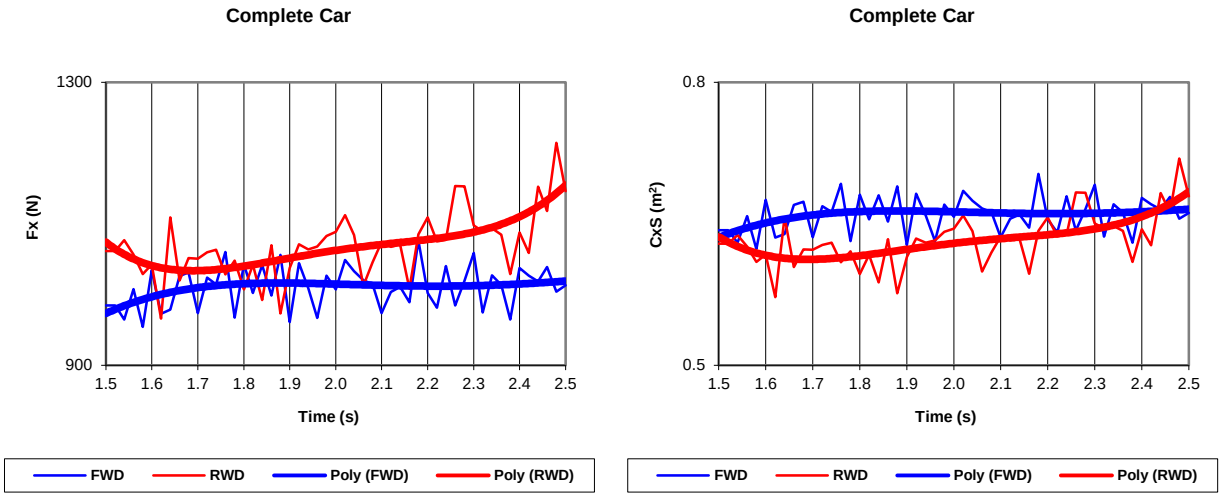

Figure 9: Variation of the total drag and the total drag coefficient of the cars with time

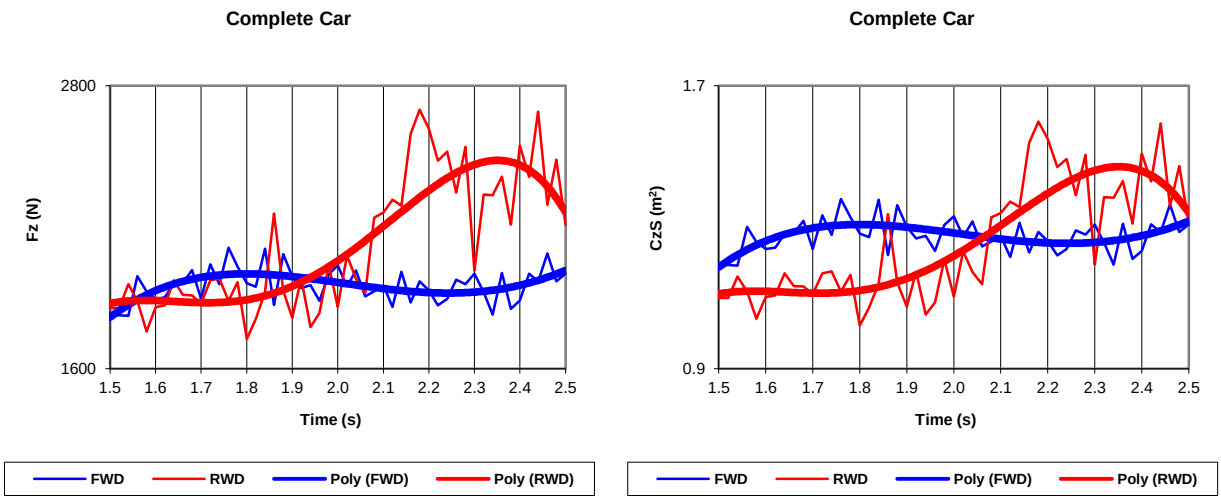

Figure 10: Variation of the total downforce and the total downforce coefficient of the cars with time

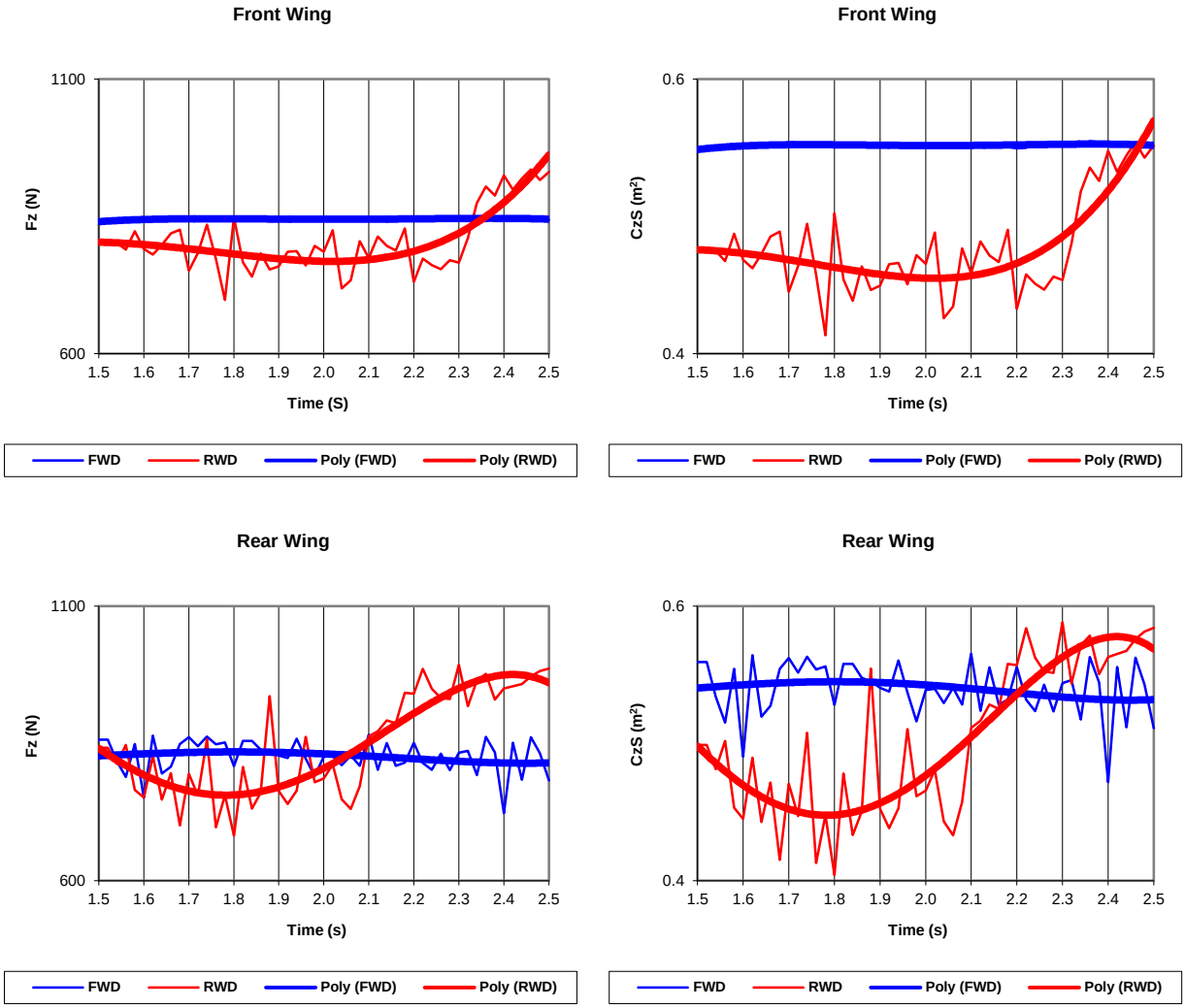

Figure 11: Variation of the downforce and the downforce coefficient of the wings of the cars with time

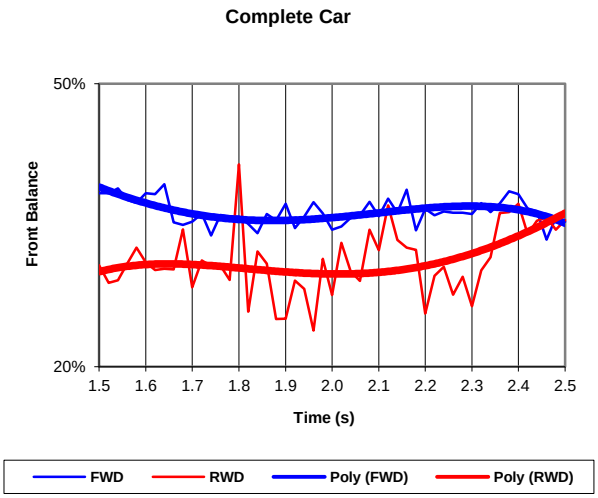

Figure 12: Variation of the front balance of the cars with time

3. CONCLUSIONS

This paper shows how CFD can be a useful tool to study the problem of the overtaking manoeuvre. To contain the number of cells the geometry was kept simple and the distance between the two cars was made quite large. Other analyses with real geometries and more appropriate trajectories are in program, that will allow to compare the numerical results with the track data.